IκBα is required for full transcriptional induction of some NFκB-regulated genes in response to TNF in MCF-7 cells

January, 2022

Graduate School of Science
Department of Biological Sciences

Minami Ando (D3)
Laboratory for Cell Systems

INDEX

1 Abstract

Once a cell receives extracellular stimulus, the signal is transduced through intracellular signaling pathways activating transcription factors. Inflammatory stimuli triggers the degradation of three inhibitory κB (IκB) proteins, allowing for nuclear translocation of Nuclear factor-κB (NFκB) for transcriptional induction of its target genes. Nuclear factor-κB (NFκB) is one of the transcription factors that is essential for regulating the transcription of immune response genes and pro-apoptotic signaling pathway related genes. Of these three, IκBα is a well-known negative feedback regulator that limits the duration of NFκB activity. In this study, whether IκBα's role in enabling or limiting NFκB activation is important for TNF (Tumor Necrosis Factor)-induced gene expression in human breast cancer cells (MCF-7) was attempted to be determined.

When IκBα was present, after NFκB rapidly translocated into the nucleus, the negative feedback regulation by IκBα produced a dampened peak of nuclear NFκB abundance. On the other hand, when IκBα was absent, nuclear NFκB abundance was persistent because of the negative feedback regulation by IκBα disappeared. The maximum nuclear NFκB abundance was higher when IκBα was present. However, when the fold change in expression level of NFκB target genes were compared between the presence and absence of IκBα, many more TNF-response genes showed reduced induction than enhanced induction when IκBα was absent. Mathematical modeling was used to investigate the underlying transcriptional regulatory mechanism. The reduced activation of some NFκB target genes in IκBα absent cells was found to be explained by the incoherent feedforward loop (IFFL) model. In addition, for a subset of genes, prolonged NFκB activity due to loss of negative feedback control did not prolong their

transient activation, indicating a multi-state transcription cycle control of gene induction. Genes encoding key inflammation-related transcription factors, such as *JUNB* and *KLF10*, were found to be best represented by a model that contained both the IFFL and the transcription cycle motif. These findings suggest the regulatory strategies that safeguard inflammatory gene expression from overproduction and repositions the function of IκBα not only as a negative feedback regulator of NFκB, but also as an enabler of NFκB-regulated stimulus-responsive inflammatory gene expression. This study indicates the complex involvement of IκBα in the inflammatory response to TNF in breast cancer cells.

The regulation strategies of safeguarding the inflammatory NFκB target gene expression from overproduction may be also important in the COVID-19 pandemic caused by infection with SARS-CoV-2. In COVID-19 patients, classical monocytes which showed a high expression level of cytokine genes including *TNF* in *CCL3* are considered to be the major source of cytokine storm. In addition, it has been reported that these patients often suffer from post-acute COVID-19 syndrome, and one of the causes are considered as inflammatory cytokine production in innate immune response. In this part, whether NFκB target cytokine genes are overproduced in *CCL3* highly expressed classical monocytes from COVID-19 patients in convalescent stages were attempt to be determined.

2 Abbreviation

ARDS…Acute respiratory distress syndrome

ATAC-seq…Assay for transposase-accessible chromatin with high-throughput sequencing

ATP…Adenosine tri-phosphate

AUC…Area under the curve

BSA…Bovine serum albumin

C1-FFL…Coherent type-1 feedforward loop

CD14+…Cluster of differentiation 14

COVID-19…Coronavirus disease of 2019

Ctrl…Control

DAPI…4',6-diamidino-2-phenylindole

DEG…Differentially expressed gene

DNA…Deoxyribonucleic acid

DRG…Delayed response gene

EDTA…Ethylenediamine tetraacetic acid

ERG…Early response gene

FBS…Fetal bovine serum

FFL…Feedforward loop

GRM…Gene regulatory mechanism

H3K27me3…Tri-methylation of lysine 27 on histone H3 protein

H3K27…Lysine 27 on histone H3 protein

HDAC1/2…Histone deacetylases 1and 2

I1-FFL…Incoherent type-1 feedforward loop

IFFL…Incoherent feedforward loop

IKKβ…Inhibitor of nuclear factor kappa-B kinase subunit beta

IQR…Interquartile range

IRG…Intermediate response gene

IκBα…Inhibitory subunit of NFκB alpha

IκB…Inhibitory kappa B

JNK…c-Jun N-terminal kinase

MAGIC…Markov affinity-based graph imputation of cells

MAPK…Mitogen-activated protein kinase

MCF-7…Human breast cancer cell line

MFI…Max-fold induction

NEMO…NFκB essential modulator

NFκB…Nuclear factor-kappa B

NuRD…Nucleosome remodeling and deacetylation

ODE…Ordinary differential equation

PBMC…Peripheral blood mononuclear cell

PBS…Phosphate-buffered saline

PCC…Pearson correlation coefficient

PCR…Polymerase chain reaction

PRC1…Polycomb repressive complex 1

PRC2…Polycomb repressive complex 2

RLE… Relative log expression

RNA-seq...Ribonucleic acid-sequencing

RPM…Reads per million

RelA…Nuclear factor NF-kappa-B p65 subunit

SARS-CoV-2…Severe acute respiratory syndrome coronavirus 2

SLM…Smart local moving

SWI/SNF…Switch/sucrose non-fermentable

TF…Transcription factor

TMM…Trimmed mean of M values

TNF…Tumor necrosis factor

TSS…Transcription start site

Tn5…Transposable 5

UMAP…Uniform manifold approximation and projection

VTE…Venous thromboembolism

mRNA…Messenger RNA

nRMSD…Root mean square deviation

siIκBα…IκBα knockdown

siRNA…Small interfering RNA

β-TRCP…Beta-transducin repeat-containing protein

κB…Kappa B

3 Introduction

3.1 The canonical NFκB signaling pathway

The canonical NFκB signaling pathway is triggered by many inflammatory stimuli, including tumor necrosis factor (TNF), an important cytokine involved in chronic and acute inflammation[1]. After cell surface receptors are activated by these stimuli, the scaffold protein NFκB essential modulator (NEMO) of IKKβ protein phosphorylates the two specific N-terminal serines of canonical inhibitory κB (IκB) proteins[2,3], which then act as a docking platform for the ubiquitin ligase β-TRCP. After ubiquitination, proteasome-mediated proteolysis of the IκB protein is induced and this enables NFκB to enter the nucleus[4] to bind to the DNA and to activate the genes (Figure 1). The pathway is responsible for regulating inflammation, control of proliferation and apoptosis of lymphoid cells during the immune response[1].

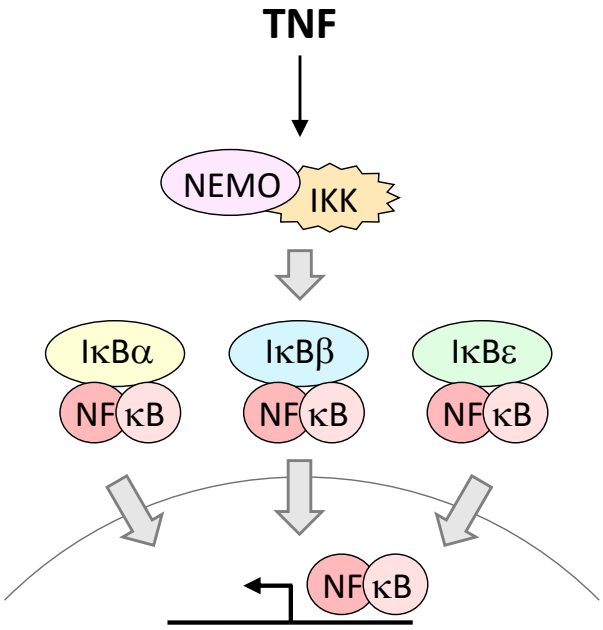

Figure 1. The canonical NFκB signaling pathway

The canonical NFκB signaling pathway is triggered by many inflammatory stimuli, including tumor necrosis factor (TNF), an important cytokine involved in chronic and acute inflammation. The activity of NFκB is precisely regulated by various inhibitors, Inhibitor of κB (α, β and ε).

3.2 Structures of NFκB

The NFκB consists of various different dimers including five homologous proteins, and there are two subfamilies, class I and II. Class I consists of p105 and p100, which contain long C-terminal domains that contain multiple copies of ankyrin repeats that act to inhibit these proteins. p105 is further processed into p50 and p100 is processed into p52 by either limited proteolysis or possibly arrested translation. Class II includes c-Rel, RelB and RelA (p65), and Rel proteins contain C-terminal transactivation domains[5]. All dimers have the ability to bind to the κB-site consensus sequence, but the biochemical functions differ depending on the combination of these proteins[1]. For example, heterodimers RelA/p50, RelA/c-Rel and p52/RelB activate transcription, whereas homodimers p50/p50 and p52/p52 repress transcription[6–14] (Figure 2). The primary NFκB isoform induced by TNF is the p50:RelA dimer[1].

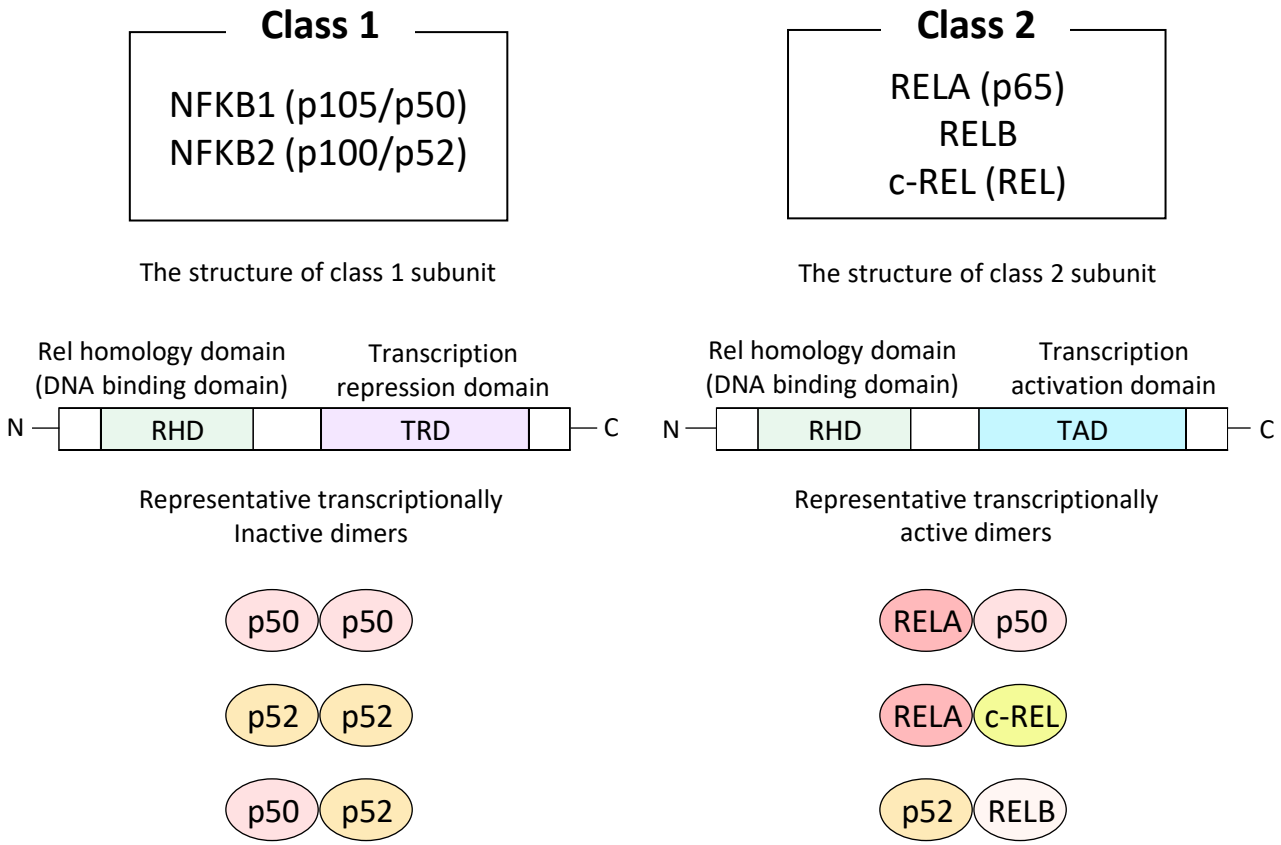

Figure 2. Classes of NFκB subunits and representative dimers

Diagram of NFκB subunits and representative dimers. NFκB consists of various different dimers including five homologous proteins, and there are two subfamilies, class I and II.

3.3 The canonical IκB proteins

The canonical NFκB pathway mediates a wide variety of extracellular and intracellular signals to control a diverse set of cellular responses[1] (Figure 3)[1]. The activity of NFκB is precisely regulated by various inhibitors, Inhibitor of κB (α, β and ε) (Figure 1) and A20[1,15]. In the canonical pathway, IκBβ is known to inhibit the nuclear translocation of NFκB, whereas IκBα and IκBε bound to NFκB actively shuttles between the nucleus and cytoplasm after stimulation[2,3] (Figure 3)[1]. Furthermore, there are distinct roles in regulating the NFκB activity between IκBα and IκBε[1,16,17]. IκBα responds most rapidly to stimuli[4,18–20], but also mediates a powerful negative feedback loop that may remove NFκB from DNA[21], and result in oscillatory NFκB activity[4]. On the other hand, IκBβ and IκBε degrade more slowly upon TNF stimulation, and IκBε mediates a second negative feedback mechanism that functions in anti-phase to IκBα[20] and dampens the NFκB oscillations produced by IκBα[4]. Thus, the precise balance of these IκB proteins determines the dynamics of nuclear NFκB activity in response to stimulation[1,16,17,22].

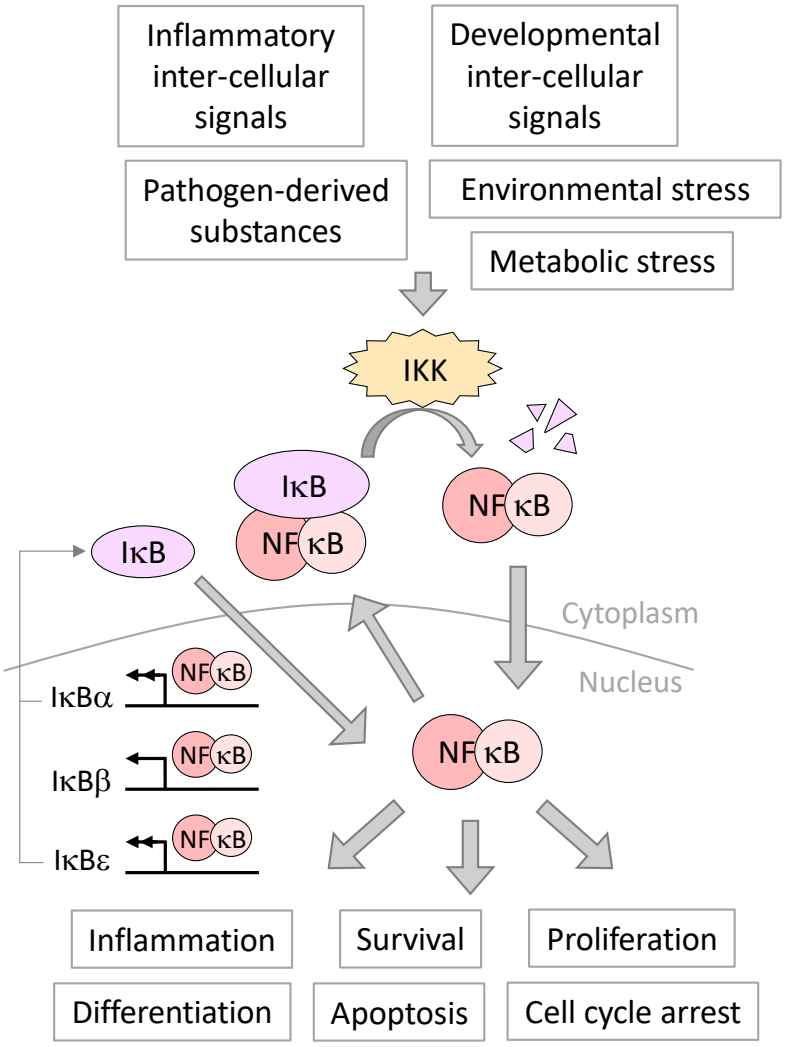

Figure 3. The canonical NFκB signaling pathway mediating various extracellular and intracellular signals[1]
Negative feedback control mediated my IκBα and IκBε allows for dynamic regulation of NFκB.

3.4 Role of IκBα in gene expression

Previous studies of IκBα's effect on gene expression have focused on its role as a negative feedback regulator that limits the duration of NFκB activity when stimulated transiently, or that result in oscillations when stimulated with TNF for an extended period of time. In a transient stimulation protocol IκBα-deficient cells show enhanced expression of some genes[4], as NFκB duration may be discriminated by a slow mRNA decay step or a slow chromatin step[23]. In the persistent stimulation protocol IκBα-deficient cells show NFκB-mediated eviction of many more nucleosomes and establishment of *de novo* enhancers[24]. However, whether the slowed and diminished NFκB activation observed in IκBα-deficient cells[4,20,25] affects gene expression has not been examined.

3.5 Post-acute COVID-19 syndrome and NFκB transcriptional regulation

Coronavirus disease 2019 (COVID-19) has caused morbidity and mortality in a global scale, but persistent and prolonged residual effects after acute COVID-19[26] have been reported. These effects of SARS-CoV-2 infection include thromboembolism, dyspnea, fatigue, hair loss, palpitations and decline in quality of life[26–29]. Previous studies have indicated that inflammatory cytokine production in the process of robust innate immune response may contribute to these sequelae[30–32]. In ongoing COVID-19, hyper-activation of the NFκB pathway is involved, and this leads to the induction of a variety of pro-inflammatory cytokines[33]. A previous study revealed that *CCL3* highly expressed CD14+ monocytes from PBMCs were highly enriched in a subpopulation of severe

patients[34]. These cells expressed significantly high cytokine genes and inflammatory genes, and are considered to be the major sources in PBMCs triggering the cytokine inflammatory storm[34]. However, whether transcriptional regulation of cytokine genes remain active in *CCL3* highly expressed CD14+ monocytes from COVID-19 patients in convalescent stages remains to be elucidated.

3.6 Aim of this study

Previous studies of IκBα's effect on gene expression have focused on its role as a negative feedback regulator that limits the duration of NFκB activity when stimulated transiently, or generates oscillatory dynamics when stimulated with TNF persistently. In a transient stimulation protocol IκBα-deficient cells show enhanced expression of some genes[4], as NFκB duration may be discriminated by a slow mRNA decay step or a slow chromatin step[23]. In the persistent stimulation protocol IκBα-deficient cells show NFκB-mediated eviction of many more nucleosomes and establishment of de novo enhancers[24]. However, whether the slowed and diminished NFκB activation observed in IκBα-deficient cells[4,20,25] affects gene expression has not been examined (Figure 4).

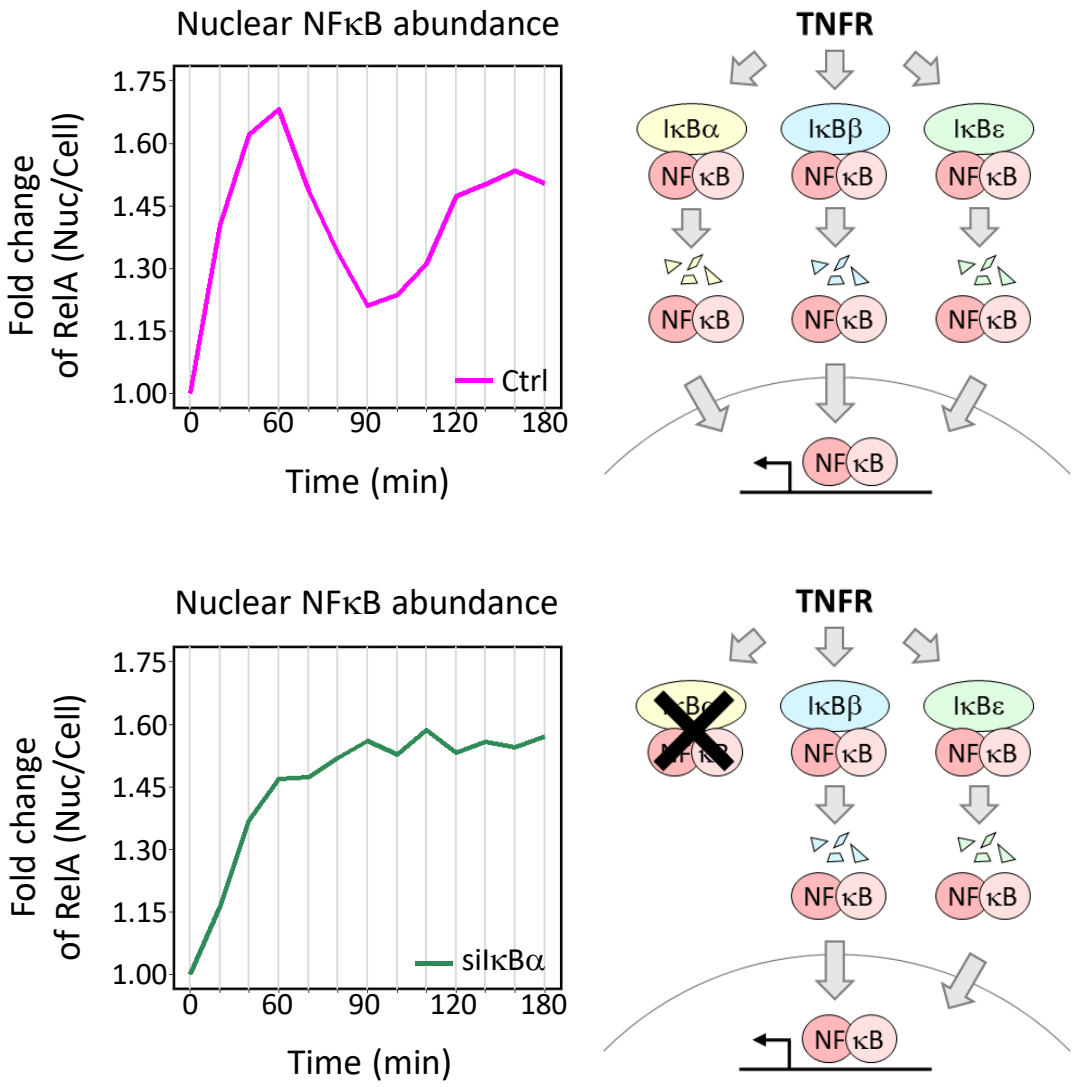

Figure 4. Dynamics of nuclear NFκB abundance

Time course nuclear NFκB abundance from fixed-cell immunofluorescence of MCF-7 cells treated with 1 ng mL^-1 TNF in Ctrl (Control) and siIκBα (IκBα knockdown). IκBα-deficient cells showed slowed and diminished NFκB activation. Line graphs represent the means of two biological replicates.

To reveal this, bulk RNA-seq transcriptomic profiling data and single-cell ATAC-seq data were measured and analyzed. A cohort of genes that are diminished in siIκBα knockdown condition were revealed, indicating a post-induction repression mechanism that suppresses NFκB target gene expression from overproduction (Figure 5).

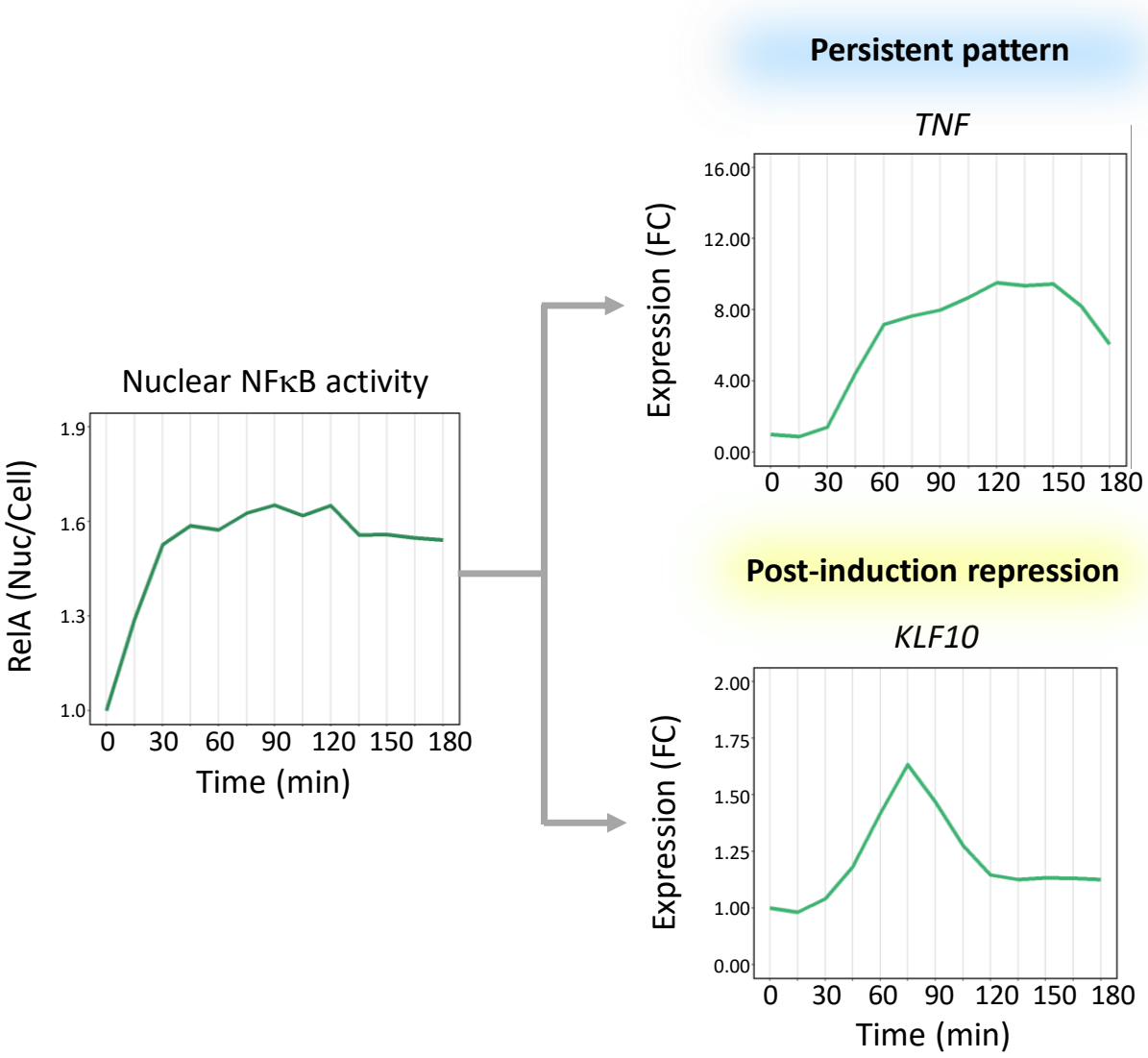

Figure 5. Post-induction repression observed for some NFκB target genes
After induction, there were some early response genes which showed post-induction repression, while some showed a persistent expression pattern similar to the nuclear NFκB abundance. This implied that there is a post-induction repression mechanism of

To investigate the gene regulatory mechanisms (GRM) that are sensitive to the presence of IκBα, mathematical models of alternative GRM models were applied to the data. The findings indicated that overproduction of inflammatory genes may cause harmful diseases, such as post-acute COVID-19 syndrome. However, whether NFκB target cytokine genes show significant accessibility at κB sites and were overproduced in a subtype of cells which are considered as the major source of cytokine storm in COVID-19 has not been examined for COVID-19 patients in convalescent stages. To reveal this, single-cell ATAC-seq data and single-cell RNA-seq data of PBMCs from COVID-19 patients in convalescent stages which may lead to post-acute COVID-19 syndrome were analyzed.

4 Methods

4.1 Experiment

All experiments were performed by Dr. Shigeyuki Magi, who was an assistant Professor in the Laboratory of Cell Systems, Institute for Protein Research, Osaka University.

4.1.1 MCF-7 cell culture and TNF treatment

The human breast adenocarcinoma MCF-7 cell line was purchased (American Type Culture Collection, Manassas, VA, USA) and propagated in Dulbecco's modified Eagle’s medium (Thermo Fisher Scientific, Waltham, MA, USA), supplemented with 10 % fetal bovine serum (FBS) and antibiotics (100 units mL^-1 penicillin and 100 μg mL^-1 streptomycin, Nacalai Tesque, Kyoto, Japan). TNFα (Thermo Fisher Scientific) was dissolved in a 0.1 % BSA/PBS (bovine serum albumin/phosphate-buffered saline) solution at a concentration of 100 ng mL^-1 and added to the cells at a final concentration of 1 ng mL^-1. These final concentrations of TNF and FBS were identified based on multiple experiments to find the best conditions that showed stable nuclear NFκB translocation oscillatory dynamics at the cell population level.

4.1.2 siRNA transfection

Reverse transfection was performed using Hiperfect reagent (Qiagen, Hilden, Germany) according to the manufacturer's instructions. Trypsinized MCF-7 cells were resuspended in an antibiotic-free medium and then mixed with a suspension of Opti-MEM (Thermo Fisher Scientific) containing 50 nM siRNA and Hiperfect reagent in 60-mm dishes (for ATAC-seq), 6-well plates (for RNA-seq), or 96-well plates (for immunostaining). SMARTpool ON-TARGETplus siRNA targeting IκBα (L-004765-00, a mixture of four sequences: AGUCAGAGUUCACGGAGUU, GCUGAUGUCAACAGAGUUA, AGGACGAGCUGCCCUAUGA, GUGCUGAUGUCAAUGCUCA), and ON-TARGETplus Non-targeting siRNA (D-001810-02, UGGUUUACAUGUUGUGUGA) were purchased from Dharmacon (GE Healthcare, now Horizon Discovery, UK). siRNA transfections were carried out 3 days before TNF-α stimulation.

4.1.3 Immunostaining

The method of immunostaining and quantification of signal intensity at every single cell was slightly modified from the previously reported method[35]. The control and IκBα-knockdown MCF-7 cells were seeded at a density of 1 x 10^4 cells well^-1 in 96-well plates. Cells were exposed to 1 ng mL^-1 of TNFα for 0–3 h at 15 min intervals, fixed with 4 % paraformaldehyde (Electron Microscopy Science, Hatfield, PA, USA) in PBS for 15 min, permeabilized with 0.1 % Triton X-100 in PBS for 5 min, and washed with PBS. After incubating with blocking solution (10 % FBS in Blocking One, Nacalai

Tesque) for 1 h at room temperature, the cells were exposed to anti-RelA antibody (#8242, Cell Signaling Technology, Danvers, MA, USA) diluted 1:200 with by blocking solution at 4 °C. The next day, the cells were stained with Dylight550 anti-rabbit-IgG antibody (#84541, Thermo Fisher Scientific) diluted 1:500 with blocking solution for 1 h at room temperature, and thereafter stained with 0.2 mg mL^-1 DAPI in PBS for nuclei detection. Fluorescence images were obtained by using InCell Analyzer 2000 (GE Healthcare, now Cytiva, Marlborough, MA, USA). The Developer Toolbox software (Cytiva) was used to segment area of the cells from bright-field images, segment area of nuclei from DAPI images, and quantify signal intensities for each cell. For each image, the signal intensity was calculated by subtracting the background signal intensity from the signal intensity of the area of the cells, and images which showed negative values of signal intensity were excluded. This was performed to remove the background effects. The experimental conditions and imaging conditions were fixed throughout the whole process, and images which were detected to show abnormally high signal intensities were excluded when contamination was observed based on visual inspection. In addition, the sparsity of the signal intensity was corrected using the flat field correction, and the cellular RelA abundance from multiple images were confirmed to show a lognormal distribution by visual inspection. The nuclear-to-cell signal ratios were calculated based on the integrated signal density (i.e., mean signal intensity x area) for two biological replicates.

4.1.4 RNA extraction and mRNA sequencing

The control and IκBα-knockdown MCF-7 cells were exposed to 1 ng mL^-1 of

TNFα for 0–3 h at 15 min intervals. Duplicate samples were used for total RNA extraction with NucleoSpin RNA Plus (Takara Bio, Shiga, Japan) according to the manufacturer's instructions. The concentration and integrity of RNA were evaluated using the Bioanalyzer 2100 (Agilent Technologies, Santa Clara, CA, USA). Thereafter, library preparation was performed using 50 ng of mRNA with the Sureselect Strand RNA kit (Agilent Technologies) according to the manufacturer's protocol. A 36 bp single-read was performed using the HiSeq2500 System (Illumina, San Diego, CA, USA) with distinct samples from the immunostaining experiments.

4.1.5 Single-cell ATAC-sequencing

To investigate whether the expression of NF-κB target genes was affected by chromatin accessibility, single-cell ATAC-seq was performed using the control and IκBα-knockdown MCF-7 cells for three biological replicates (distinct samples from immunostaining experiments and bulk RNA-sequencing experiments were used). The cells were stimulated with 1 ng mL^-1 TNFα for 0 min, 30 min, 75 min, and 120 min, and then collected using TrypLE™ Select (Thermo Fisher Scientific). The cells were washed twice with ice-cold PBS. The cell aggregates were removed by the pluriStrainer 20 μm (pluriSelect Life Science, Leipzig, Germany) and resuspended in PBS (250 cells μL^-1). The preparation of single-cell ATAC-Seq libraries using the C1 system (Fluidigm, South San Francisco, CA, USA) and Nextera DNA Library Preparation Kit (Illumina) was performed with reference to the previously reported method in the paper[36] and the deposited protocol in the manufacture's platform (Fluidigm script Hub https://www.fluidigm.com/c1openapp/scripthub/script/2015-06/single-cell-chromatin-

accessib-1433443631246-1, Revision C), with some modifications: The cell suspension and suspension regents (Fluidigm) were mixed in a 7:3 ratio and loaded into a C1 Single-Cell Open App IFC 17-25 µm (Fluidigm). Thereafter, a phase-contrast microscope was used to check whether any single cell without cell debris was captured. The cells were lysed and exposed to ATAC reaction by Tn5 transposition mix [1.5 x TD buffer, 1.5 x Tn5 transposase (Nextera DNA Sample Prep Kit, Illumina), 1.5 x C1 Loading Regent with no salt (Fluidigm), 0.15 % NP-40] at 37 °C for 30 min. Tn5-DNA complexes were dissociated from chromatin via the addition of the EDTA buffer (50 mM EDTA, 8.5 mM Tris-HCl pH 8, 1 x C1 Loading Regent with no salt) for 30 min at 50 °C, and thereafter free EDTA was quenched by the $MgCl_2$ buffer (45 mM $MgCl_2$, 0.5 mM Tris-HCl pH 8, 1 x C1 Loading Regent with no salt). Then, polymerase chain reaction (PCR) was performed with ATAC Seq PCR Mix [1.4 µM non-indexed custom Nextera PCR primers 1 and 2 (Illumina), 1 x C1 Loading Reagent with low salt, and 1.1 x NEBnext High-Fidelity PCR Master Mix (New England Biolabs, Ipswich, MA, USA)] using the following conditions: 72 °C for 5 min; 98 °C for 30 s; and thermocycling at 98 °C for 10 s, 72 °C for 30 s, and 72 °C for 1 min. The amplified transposed DNA in every single cell was collected in approximately 3.5 µL each of C1 Harvest Reagent each (Fluidigm). The single-cell DNA library was collected from C1 Single-Cell Open App IFC (Fluidigm) and mixed with 10 µL of C1 DNA Dilution Reagent (Fluidigm). To dual-index the harvested libraries, 10 µL of harvested libraries were amplified for an additional 14 cycles in 50 µL of PCR reagent [1.25 µM custom Nextera dual-index PCR primers (Illumina) in 1x NEBnext High-Fidelity PCR Master Mix (New England Biolabs)] with the following PCR conditions: 72 °C for 5 min; 98 °C for 30 s; and thermocycling at 98 °C for 10 s, 72 °C for 30 s, and 72 °C for 1 min. The PCR products from 96 single cells were collected

in a single tube and purified using a single MinElute PCR purification Kit column (Qiagen). The purified library was then eluted with 20 μL of pure H_2O. To remove primer dimers, the pooled libraries were purified twice or thrice using the same volume of AMPure XP beads (Beckman Coulter, Brea, CA, USA). After quantifying the library using the Bioanalyzer 2100, multiplex sequencing (36 bp single-read) was performed using HiSeq2500 (Illumina).

4.2 Computational analysis of sequence data

4.2.1 Sequencing mapping of bulk RNA-seq data

Bulk RNA-seq datasets were aligned using HISAT2[37] version 2.0.5 to build version 'GRCh38/hg38' of the human genome after adapter trimming by TrimGalore[38] version 0.6.0. Alignments were performed using option '–p 12 –q' where –p 12 indicates that 12 threads were ran on parallel processors and synchronized when parsing reads and outputting alignments; –q indicates that the reads are in FASTQ file format. Mapped reads assigned to genomic features were counted using featureCounts[39] version 1.5.2. Assignments were performed using the option '-t exon –g gene_name' where –t exon indicates that featureCounts[39] specifies the feature type in 'exon'; and –g gene_name indicates that gene_name is the attribute type used to group features when GTF annotation is provided.

4.2.2 Quantification of expression level

The size factor and library size were calculated using the 'calcNormFactors' function in the R package 'edgeR'[40] from the read counts which were normalized to the read counts of each transcript to be at the length of 1000. Where X_t is the read counts per 1000 bps, R_t is the read counts that were mapped, L_t is the length of the transcript length, S_t is the library size, N_t is the normalization factor of RLE normalization, and TPM_t is the TPM.

$$X_t = \frac{R_t}{L_t} 10^3 \ldots (1)$$

$$\mathrm{TPM}_t = X_t \frac{1}{S_t N_t} 10^6 \ldots (2)$$

The expression level for each protein-coding gene was normalized using RLE normalization, where the raw read counts were normalized by the number of the total read counts to be 1,000,000 after the read counts were divided by the product of the library size and size factor. The mean value of the two replicates was used for further analysis.

4.2.3 Identification of DEGs

DEGs were identified using the 'DESeq' function in the R package 'DESeq2'[41] by performing a Wald significance test between the gene expression levels before and after TNF stimulation for each time point to calculate the adjusted p-values and fold change in expression for each gene in control and siIκBα. The expression levels of the

genes were normalized using the RLE normalization method. Genes with adjusted p-values < 0.05, log2 fold change ≥ 0 were classified as upregulated DEGs, and adjusted p-values < 0.05, and log2 fold change ≤ 0 as downregulated DEGs.

4.2.4 Clustering and subclustering of DEGs

The DEGs in the control and siIκBα were clustered into groups by their z-score normalized expression level using Fuzzy c-means clustering from the 'cmeans' function in the R package 'e1071'. Used parameters are: centers=5 for control and 3 for siIκBα (number of clusters), iter.max=2 (maximum number of iterations), method=cmeans (clustering method), m=1.3 (fuzzy partition matrix) and dist=euclidean (similarity measurement). Furthermore, for each TNF-induced cluster (ERGs, IRGs, and DRGs), the z-score normalized fold change was calculated for both conditions and identified the mean time point of the maximum expression level. The z-score normalized fold change was extracted at the corresponding time points until it reached the time point just before the mean time point of maximum expression level for each cluster. The extracted z-score normalized fold change in the control and siIκBα were combined for each gene. The genes were subclustered into two groups in each cluster based on these values using Fuzzy c-means clustering. Used parameters are: centers=2 (number of clusters), iter.max=2 (maximum number of iterations), method=cmeans (clustering method), m=1.3 (fuzzy partition matrix) and dist=euclidean (similarity measurement). Motif analysis was performed using 'findMotifsGenome' command in HOMER[42] version 4.10.4 for each cluster in control and siIκBα.

4.2.5 Sequencing mapping of single-cell ATAC-seq data

Single-cell ATAC-seq datasets containing two or more cells and samples that were contaminated were filtered out. A total of 989 cells remained in the control and 953 cells in the siIκBα, which were used for further analysis. In addition, a dataset was prepared in which all cells of the three replicates were aggregated into one dataset for each time point in each condition. The single-cell and aggregated datasets were aligned using Bowtie[43] version 2.3.4.1, to build version UCSC26/hg38 of the human genome. Alignments were performed using the option '-S -p 8 -m 1' where -S indicates that alignments will be printed in SAM format; -p 8 indicates that eight parallel search threads will be launched; and -m 1 indicates that all alignments for a particular read will be suppressed if more than one reportable alignment exists. Picard (http://broadinstitute.github.io/picard/) version 1.119 was used to remove duplicates that arose during sample preparation. Mitochondrial chromosomes were removed from the mapped data using samtools[44] version 1.9. The 'bamCoverage' function in deepTools[45] version 2.4.3 was used to quantify the reads mapped to the genome using the option '--binSize 1 -e 200 -ignoreForNormalization chrX -p max' where --binSize 1 indicates that each genomic region mapped by the reads are normalized to a bin of 1; -e 200 indicates that the reads will be extended to a fragment size of 200; -ignoreForNormalization chrX indicates that chromosome X will be excluded for computing the normalization; and -p max indicates that eight processors are used for the calculation.

4.2.6 Peak region identification

Peak calling was performed with MACS2 (https://pypi.org/project/MACS2/) version 2.1.2.1 using the option '-f BAM -g hs -q 0.05 --mfold 6 50' where -f BAM indicates the format of the input file; -g hs indicates the mappable human genome size; -q 0.05 indicates the cutoff to call significant regions is 0.05; and --mfold 6 50 indicates the lower and upper threshold of the height of the ATAC-seq peaks.

4.2.7 Quantification of chromatin accessibility

The signal of peak regions was calculated using 'multiBigwigSummary' function in deepTools[45], using the option '--BED' where a BED file with promoter regions defined as $\pm$ 500 bps TSS of protein coding genes from version GRCh38/hg38 of the human genome was provided. To normalize each signal at each time point, reads per million (RPM) were calculated, where the raw signal was normalized by the number of the total signal to be 1,000,000 after the read counts were divided by the product of the library size and size factor. The size factor and library size to normalize the ATAC-seq signal for each protein-coding gene were calculated using the TMM normalization method from the 'calcNormFactors' function in the R package 'edgeR'[40].

4.2.8 Identification and clustering of TNF-induced peak regions

Using the identified peak regions, significantly induced peak regions were detected for each time point after stimulation using the 'getDifferentialPeaks' command in HOMER[42] and these regions were merged. Regions that were not induced after TMM normalization were filtered out. The remaining regions were clustered based on their time-course chromatin accessibility. The chromatin accessibility at each time point was classified into a group in which its z-score normalized chromatin accessibility was smaller than 0 (z-score $<$ 0) and a group whose z-score normalized chromatin accessibility was more than 0 (z-score $\geq$ 0). For each cluster, motif analysis was performed using the 'findMotifsGenome' command in HOMER[42] and identified clusters which showed enrichment of κB sites. From this result, only the regions that included

κB sites in each cluster were extracted. The aggregated single-cell chromatin accessibility at those regions in each condition was calculated and a paired t-test from 't.test' function in the R package 'stats' was performed to determine whether they show statistical significance. In addition, the single-cell chromatin accessibility at those regions in each condition was calculated and a 10-fold cross validation using a Bayesian generalized linear model from the 'train' function in the R package 'caret' was performed to calculate the accuracy of the classification between the single cells of control and siIκBα in those regions.

4.3 Mathematical modeling

4.3.1 The input nuclear NFκB abundance

Basal nuclear NFκB activity from the two independent immunostaining results was subtracted from all time points in control and siIκBα. For replicate 1, the fold change of nuclear NFκB activity in control and siIκBα was calculated. Then, the fold change in the control and siIκBα together was converted using the 'rescale' function in the R package 'scales' to span a range of 2–100 to avoid assay specific reductions of the dynamic range. The fold change in nuclear NFκB activity of replicate 2 from the immunostaining result in the control was converted to span a range of 2–100 to avoid assay-specific reductions in the dynamic range. Then, the immunostaining result in the siIκBα of replicate 2 was converted using the same scale used for the control. Scaling methods were different between the two replicates because the time course nuclear NFκB activity of replicate 2 in both conditions was consistently lower than the activity of

replicate 1 in both conditions. Thus, to standardize the maximum activity of replicates 1 and 2, and because the maximum activity at the first peak in the control is also the maximum activity of both conditions in replicate 1 but not in replicate 2, showing the maximum activity of both conditions at late time points in siIκBα, activity of replicate 2 in control was scaled individually to avoid the scaled maximum activity (which is 100 in replicate 1) to appear at late time points in siIκBα but to appear at the first peak in control, similar to the scaled maximum activity of replicate 1. Each of the scaled nuclear NFκB activities was interpolated to every second using the 'pchipfun' function in the R package 'pracma'. These interpolated data for each replicate were used as the input of all ODE models, which were numerically solved using the 'ode' function in the R package 'deSolve'.

4.3.2 The simple model

A simple model was used to reproduce a transcription regulating mechanism that considers only the nuclear NFκB activity and its target gene (Figure 6).

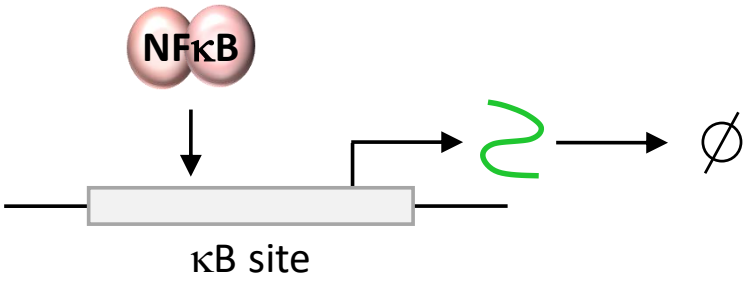

Figure 6. A simple mathematical model
Schematic diagram of the simple mathematical model.

Where, k_{syn} is the synthesis rate constant for the target gene, k_{deg} is the mRNA degradation rate constant for the target gene, K_D is the NFκB-regulation strength constant for the target gene, h is the Hill function exponent for the target gene, and τ is the time between nuclear NFκB and mature poly A^+ mRNA production.

$$\frac{d[\text{mRNA}(t)]}{dt} = k_{syn}\left(\frac{(K_D\,[\text{NFkB}(t-\tau)])^h}{(K_D\,[\text{NFkB}(t-\tau)])^h + 1}\right) - k_{deg}[\text{mRNA}(t)] \ldots (3)$$

The free parameters k_{deg}, K_D, and τ were optimized with bound constraints (2e-5 $< k_{deg} <$ 2e-3 s^{-1}, $0.001 < K_D < 1000\ s^{-1}$, and $0 < \tau < 7200$ sec). For simplicity, h was fixed at 1 and k_{syn} was fixed at 1 s^{-1}.

4.3.3 The IFFL model

The IFFL model[46] was used to enable a transcription-regulating mechanism that is fold change detectable (Figure 7). This model considered the competitor that binds to the target gene promoter to interfere with the transcriptional regulation by NFκB.

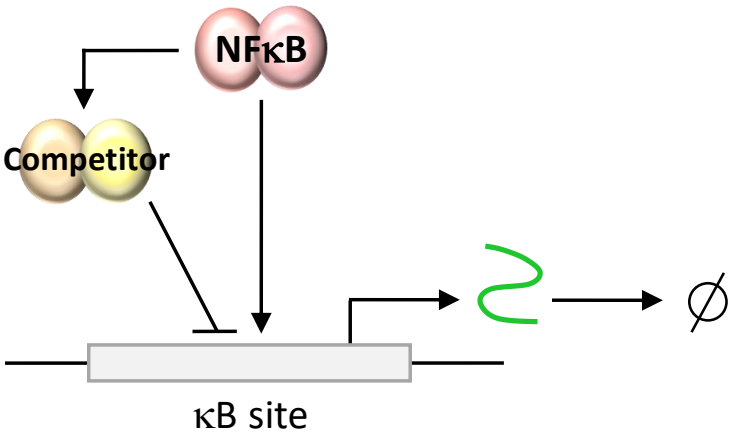

Figure 7. An IFFL (incoherent feedforward loop) model
Schematic diagram of the IFFL model.

Where, k_{degTF} is the mRNA degradation rate constant for the competitor transcription factor gene, K_{DTF} is the NFκB-regulation strength constant for the competitor transcription factor gene, K_{D1} is the NFκB-regulation strength constant for the target gene, K_{D2} is the competitor transcription factor-regulation strength constant for the target gene, h_{TF} is the Hill function exponent for the competitor transcription factor gene, and τ_{TF} is the time between nuclear TF and mature poly A^+ mRNA production.

$$\frac{d[\mathrm{TF}(t)]}{dt} = \left(\frac{(K_{DTF}[\mathrm{NFkB}(t-\tau)])^{h_{TF}}}{(K_{DTF}[\mathrm{NFkB}(t-\tau)])^{h_{TF}}+1}\right) - k_{degTF}[\mathrm{TF}(t)] \ldots (4)$$

$$\frac{d[\mathrm{mRNA}(t)]}{dt} = k_{syn}\left(\frac{(K_{D1}[\mathrm{NFkB}(t-\tau)])^{h}}{(K_{D1}[\mathrm{NFkB}(t-\tau)])^{h}+(K_{D2}[\mathrm{TF}(t-\tau_{TF})])^{h}+1}\right) - k_{deg}[\mathrm{mRNA}(t)] \ldots (5)$$

The free parameters k_{deg}, K_{D1}, K_{D2}, and τ were optimized with bound constraints (2e-5 $< k_{deg} <$ 2e-3 s^{-1}, $0.001 < K_{D1}, K_{D2} < 1000$ s^{-1}, and $0 < \tau <$ 7200 sec). For simplicity, h was fixed at 2, h_{TF} was fixed at 1, k_{degTF} was fixed at 8.022537e-6 s^{-1}, K_{DTF} was fixed at 100 s^{-1}, τ_{TF} was fixed at 7200[47,48] sec and k_{syn} was fixed at 1 s^{-1}.

4.3.4 The 3-state cycle model

The 3-state cycle model was constructed to recapitulate the promoter state transition from the active state (state A) to the closed state (state C), which induces transcriptional repression of the target gene (Figure 8).

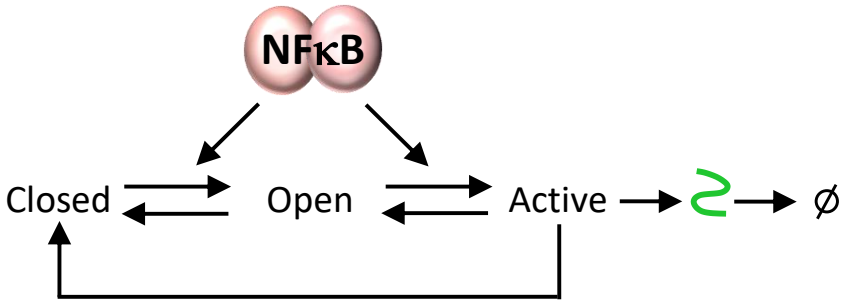

Figure 8. A 3-state transcription control cycle model
Schematic diagram of the 3-state cycle model.

Where K_{D3} is the cooperativity of the active chromatin state at the promoter region of the target gene, and k_1, k_2, k_{-1}, k_{-2}, and k_{-3} are the reaction rate constants.

$$\frac{dC}{dt} = -k_1\left(\frac{K_{D1}[\mathrm{NFkB}(t)]}{K_{D1}[\mathrm{NFkB}(t)]+1}\right)\cdot C + k_{-1}\cdot O + k_{-3}\left(\frac{K_{D3}\cdot A}{K_{D3}\cdot A+1}\right) \ldots (6)$$

$$\frac{dO}{dt} = k_1\left(\frac{K_{D1}[\mathrm{NFkB}(t)]}{K_{D1}[\mathrm{NFkB}(t)]+1}\right)\cdot C - k_2\left(\frac{K_{D2}[\mathrm{NFkB}(t)]}{K_{D2}[\mathrm{NFkB}(t)]+1}\right)\cdot O - k_{-1}\cdot O + k_{-2} \cdot A \ldots (7)$$

$$\frac{dA}{dt} = k_2\left(\frac{K_{D2}[\mathrm{NFkB}(t)]}{K_{D2}[\mathrm{NFkB}(t)]+1}\right)\cdot O - k_{-2}\cdot A - k_{-3}\left(\frac{K_{D3}\cdot A}{K_{D3}\cdot A+1}\right) \ldots (8)$$

$$1 = C + O + A \ldots (9)$$

$$\frac{d[\mathrm{mRNA}(t)]}{dt} = k_{syn}\cdot A(t-\tau) - k_{deg}[\mathrm{mRNA}(t)] \ldots (10)$$

The free parameters k_1, k_2, k_{deg}, K_{D1}, K_{D2}, and τ were optimized with bound constraints (2e-5 $< k_{deg} <$ 2e-3 s^{-1}, 6e-5 $< k_1 <$ 6e-3 s^{-1}, 0.007 $< k_2 <$ 69.315 s^{-1}, 1e-4 $< k_1, k_2 <$ 1 s^{-1}, 0.001 $< K_{D1}, K_{D2} <$ 1000 s^{-1}, and 0 $< \tau <$ 7200 sec). For simplicity, k_{-1} was fixed at $0.01 \times k_1$ s^{-1}, k_{-2} was fixed at $0.01 \times k_2$ s^{-1}, k_{-3} was fixed at 1 s^{-1}, K_{D3} was fixed at 0.5 s^{-1}, and k_{syn} was fixed at 1 s^{-1}.

4.3.5 The model v4

Model v4 is a combination of the 3-state cycle and the IFFL models (Figure 9).

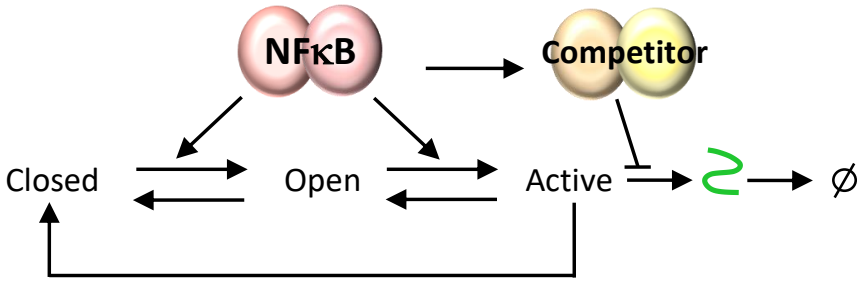

Figure 9. The model v4

Schematic diagram of the model v4

$$\frac{dC}{dt} = -k_1\left(\frac{K_{D1}[\text{NFkB}(t-\tau)]}{K_{D1}[\text{NFkB}(t-\tau)]+1}\right)\cdot C + k_{-1}\cdot O + k_{-3}\left(\frac{K_{D3}\cdot A}{K_{D3}\cdot A+1}\right) \ldots (11)$$

$$\frac{dO}{dt} = k_1\left(\frac{K_{D1}[\text{NFkB}(t-\tau)]}{K_{D1}[\text{NFkB}(t-\tau)]+1}\right)\cdot C - k_2\left(\frac{K_{D2}[\text{NFkB}(t-\tau)]}{K_{D2}[\text{NFkB}(t-\tau)]+1}\right)\cdot O - k_{-1}\cdot O + k_{-2}\cdot A \ldots (12)$$

$$\frac{dA}{dt} = k_2\left(\frac{K_{D2}[\text{NFkB}(t-\tau)]}{K_{D2}[\text{NFkB}(t-\tau)]+1}\right)\cdot O - k_{-2}\cdot A - k_{-3}\left(\frac{K_{D3}\cdot A}{K_{D3}\cdot A+1}\right) \ldots (13)$$

$$\frac{d[\text{TF}(t)]}{dt} = \left(\frac{(K_{DTF}[\text{NFkB}(t)])^{h_{TF}}}{(K_{DTF}[\text{NFkB}(t)])^{h_{TF}}+1}\right) - k_{degTF}[\text{TF}(t)] \ldots (14)$$

$$1 = C + O + A \ldots (15)$$

$$\frac{d[\text{mRNA}(t)]}{dt} = k_{syn}\left(\frac{\left(A(t-\tau)\right)^h}{\left(A(t-\tau)\right)^h + (K_{DTF2}[\text{TF}(t-\tau_{TF})])^h + 1}\right) - k_{deg}[\text{mRNA}(t)] \ldots (16)$$

K_{DTF2} is the competitor TF regulation strength constant for the target gene.

The free parameters k_{deg}, k_1, k_2, K_{D1}, K_{D2}, K_{DTF2}, and τ were optimized with bound constraints (2e-5 $< k_{deg} <$ 2e-3 s^{-1}, 6e-5 $< k_1 <$ 6e-3 s^{-1}, 0.007 $< k_2 <$ 69.315 s^{-1}, 0.001 $< K_{D1}, K_{D2}, K_{DTF2} <$ 1000 s^{-1}, and 0 $< \tau <$ 7200 sec). For

simplicity, h was fixed at 2, h_{TF} was fixed at 1, k_{degTF} was fixed at 8.022537e-6 s^{-1}, K_{DTF} was fixed at 100 s^{-1}, τ_{TF} was fixed at 7200 sec, k_{-1} was fixed at $0.01 \times k_1$ s^{-1}, k_{-2} was fixed at $0.01 \times k_2$ s^{-1}, k_{-3} was fixed at 1 s^{-1}, K_{D3} was fixed at 0.5 s^{-1}, and k_{syn} was fixed at 1 s^{-1}.

4.3.6 Model maturation

Parameters for each model were optimized using the subplex algorithm from the 'sbplx' function in the R package 'nloptr' to minimize the normalized RMSD (which was calculated using the 'rmsd' function in the R package 'bio3d'[49]) between max-normalized measured data and max-normalized simulated results which span from 0 to 1 and the difference between the simulated expression at the start of steady state (-60 min) and the end of steady state (0 min). RMSD is calculated by the following formula, where x_i is the expected value, y_i are the observed values, and n is the total number of values. Max-normalized expression of measured data was calculated after subtracting the basal expression from the expression for all time points in each condition.

$$\text{RMSD} = \sqrt{\frac{1}{n}\sum_{i=1}^{n}\|x_i - y_i\|^2} \quad \ldots (17)$$

4.3.7 Parameter optimization process and identification of concordant parameter sets

To identify the best-fit parameter, a 2-step parameter optimization process was applied. First, using the scaled input nuclear NFκB activity, expression was simulated and the time-course fold change in expression in the control and siIκBα were calculated. The time-course fold change in expression from the entire dataset was also calculated, and these were max-normalized to span a range of 0 to1 for both simulation and data. Next, the nRMSD was minimized between the max-normalized fold change between the simulation and data in the control for 100 initial parameter sets. Within these optimized parameter sets, parameter sets with nRMSD $<$ 0.5 were selected, some of which were set to 0.6 or 0.7, and identified the minimum and maximum values for each parameter. Using these two values as the lower and upper bound constraints, 100 initial parameter sets were further produced and were optimized by minimizing the nRMSD of the max-normalized fold change between the simulation and data in siIκBα.

After performing this optimization process for two biological replicates, the score for each optimized parameter set for each biological replicate was calculated. The concordant optimized parameter sets between replicates 1 and 2 were identified to ensure the robustness of each parameter value. First, all possible pairs of optimized parameter sets from replicates 1 and 2 (100 optimized parameter sets in replicate 1 $\times$ 100 optimized parameter sets in replicate 2 $=$ 10,000 pairs) were generated. For the score of parameters k_{deg} and K_D, the larger parameter value in either replicate 1 or replicate 2 was divided by the smaller parameter value in either replicate 1 or 2. For the score of τ, the absolute value of the difference between τ in replicate 1 and τ in replicate 2 was calculated. The nRMSD score was the sum of the nRMSD in replicate 1

and nRMSD in replicate 2 for the ERGs, IRGs and DRGs from simple model and IFFL model. The method to identify the concordant parameter sets for the ERGs in subcluster 2 is different for the 3-state cycle model and model v4, where only the score for k_1, k_2, k_{deg}, τ, and nRMSD were calculated. The method to identify concordant parameter sets for IRGs and DRGs from 3-state cycle model and model v4 are the same as simple model and IFFL model. The total score of these scores was identified for each optimized parameter pair, and the parameter pair with the smallest total score for each gene was identified.

4.3.8 Chromatin remodeling at promoter regions of post-induction repressed ERGs

There were 11 post-induction repressed genes that were best demonstrated by the 3-state cycle model or model v4. These genes all belonged to the ERGs in subcluster 2, and all the other genes that were best demonstrated by any of the four models were 89 in total. The peak regions at each time point in control and siIκBα that were included in the promoter regions ($\pm$ 500 bps TSS) of these 100 genes were identified. For these peak regions, motif analysis was performed using the 'findMotifsGenome' command in HOMER[42] to identify peak regions which showed enrichment of κB sites. From this result, only the peak regions that included κB sites were further extracted. When κB site enriched regions were identified for multiple time points, regions were merged using the 'mergePeaks' command in HOMER[42] using the default setting.

The signal of these peak regions was calculated using 'multiBigwigSummary' function in deepTools[45], using the option '--BED' where a BED file with promoter regions

defined as ± 500 bps TSS of protein coding genes from version GRCh38/hg38 of the human genome was provided. To normalize each signal at each time point, reads per million (RPM) were calculated, where the raw signal was normalized by the number of the total signal to be 1,000,000 after the read counts were divided by the product of the library size and size factor. The size factor and library size to normalize the ATAC-seq signal for each protein-coding gene were calculated using the TMM normalization method from the 'calcNormFactors' function in the R package 'edgeR'[40]. The κB site enriched regions that showed a start of decrease in chromatin accessibility at least at 30 minutes or 75 minutes in both Ctrl and siIκBα were selected and z-score normalized for each condition for heatmaps. The heatmaps of the time course fold change in expression of the 11 post-induction repressed ERGs in Ctrl and siIκBα were max-normalized from 0 to 1 for each condition using the gene expression data.

4.4 Analysis of sequence data from COVID-19 patients

4.4.1 Pre-processing of single-cell ATAC-seq data

To investigate chromatin accessibility at gene regions of inflammatory cytokine genes in *CCL3* highly accessible CD14+ monocytes, a published single-cell ATAC-seq data[50] was analyzed. The data was collected from 3,231 PBMCs from 6 healthy controls (1,114 cells), 5 moderate COVID-19 patients in convalescent stages (1,490 cells) and 3 severe COVID-19 patients in convalescent stages (627 cells). Dimensionality reduction and batch effect correction were performed for this data using iterative latent semantic indexing (LSI) in the 'addIterativeLSI' function and Harmony algorithm in the

'addHarmony' function in the R package 'ArchR'[51]. Since not only the local chromatin accessibility at promoters of the gene but also the chromatin accessibility at the gene body best predicts gene expression[51], the normalized chromatin accessibility was calculated by depth normalizing across all genes after multiplying the read counts by their corresponding distance and gene size weights in the 'ArchRProject' function in the R package 'ArchR'[51]. When chromatin accessibility of a particular gene showed FDR $\leq$ 0.05 and $\log_2$FC $\geq$ 1.25 between a cluster of cells which showed high chromatin accessibility of this gene and clusters of cells that did not, this gene was defined as a marker gene[50]. Then, the weights of the cells were imputed to reduce sparsity using Markov affinity-based graph imputation of cells[52] (MAGIC) in the 'addImputeWeights' function in the R package 'ArchR'[51]. Canonical marker genes of monocytes (*CD14*, *CD16*(*FCGR3A*) and *CEBPB*)[50] were identified and overlaid on UMAP embedding in the 'addUMAP' function in the R package 'ArchR'[51]. In addition, *CCL3* was also a marker gene, and was overlaid on UMAP embedding to identify CD14+ monocytes that showed high chromatin accessibility of *CCL3*. To identify the cluster which showed a significantly high chromatin accessibility of *CD14* and *CCL3*, clustering was performed using the smart local moving (SLM) algorithm[53]. A total of 400 cells in cluster 1 were extracted and annotated as *CCL3* highly accessible CD14+ monocytes, and used for downstream analysis.

4.4.2 Identification of significantly accessible regions

Using the data of *CCL3* highly accessible CD14+ monocytes, 136 cytokine genes were identified based on previous literature[50] and their chromatin accessibility at gene

regions were compared between healthy controls, moderate and severe COVID-19 patients in convalescent stages. Statistical significance ($p < 0.05$) in single-cell chromatin accessibility at gene regions was observed for 28 cytokine genes between severe COVID-19 patients in convalescent stages and healthy controls when a one-tailed Wilcoxon rank sum test[34] was performed. Among these 28 cytokine genes, 14 were NFκB target genes, while others were not.

4.4.3 Motif analysis at peak regions in promoters

These groups of NFκB target genes and genes that were not NFκB target genes were used for motif analysis at peak regions in promoters of these genes to investigate whether NFκB binding motifs were significantly accessible in promoters of NFκB target genes, but not in promoters of genes that are not NFκB target genes. The peak regions were identified using MACS2 (https://pypi.org/project/MACS2/) version 2.2.7.1 in the 'addReproduciblePeakSet' function in the R package 'ArchR'[51]. Peak regions included in promoters (-5kb TSS) were identified for both NFκB target genes and genes that are not NFκB target genes. Using these peak regions in promoters, motif analysis was performed using the 'findMotifsGenome' command in HOMER[42] for the 2 groups of genes. In addition, to confirm that κB sites were only enriched in promoters of NFκB target genes, motif analysis was performed for peak regions in promoters of NFκB target genes using the peak regions in promoters of genes that are not NFκB target genes as the background using the 'findMotifsGenome' command in HOMER[42].

4.4.4 Relating expression levels and chromatin accessibility

To investigate whether 28 cytokine genes which showed a significantly high chromatin accessibility at gene regions in severe patients compared to healthy controls also show an associated increase in expression levels in severe patients, a published single-cell RNA-seq data[34] was analyzed. The data was collected from 35,680 *CCL3* highly expressed CD14+ monocytes in PBMCs from 25 healthy controls (2,473 cells), 71 moderate COVID-19 patients in convalescent stages (10,081 cells) and 80 severe COVID-19 patients in convalescent stages (23,126 cells). Using the normalized expression levels of genes from this processed single-cell expression data[34], the expression levels were compared between healthy controls, moderate and severe COVID-19 patients in convalescent stages. Statistical significance ($p < 0.05$) in expression level was observed for 5 genes that are not NFκB target genes and 7 NFκB target genes among the 28 cytokine genes between severe COVID-19 patients in convalescent stages and healthy controls when a one-tailed Wilcoxon rank sum test[34] was performed. To validate whether the chromatin accessibility at gene regions and expression levels of these 12 cytokine genes show correlation, Pearson correlation coefficient was identified between the mean expression levels and mean chromatin accessibility at gene regions of all genes in all groups (healthy controls, moderate and severe COVID-19 patients in convalescent stages).

5 Results

5.1 NFκB target gene activation in the presence or absence of IκBα

To observe the difference in NFκB dynamics in the presence or absence of IκBα in MCF-7 cells, imaging experiments using fixed immunofluorescence to measure the time course of nuclear NFκB activity after stimulation with TNF were conducted. When IκBα was present, NFκB transiently translocated into the nucleus at earlier time points, followed by a dampened peak at later time points, whereas when the IκBα gene was knocked down using siRNA, nuclear translocation of NFκB was prolonged (Figure 10a). Furthermore, the basal level of nuclear NFκB abundance was 13 % higher when IκBα was knocked down (Figure 10b), and this difference in the basal level produced a significantly higher fold change in expression in the presence of IκBα (Figure 10c).

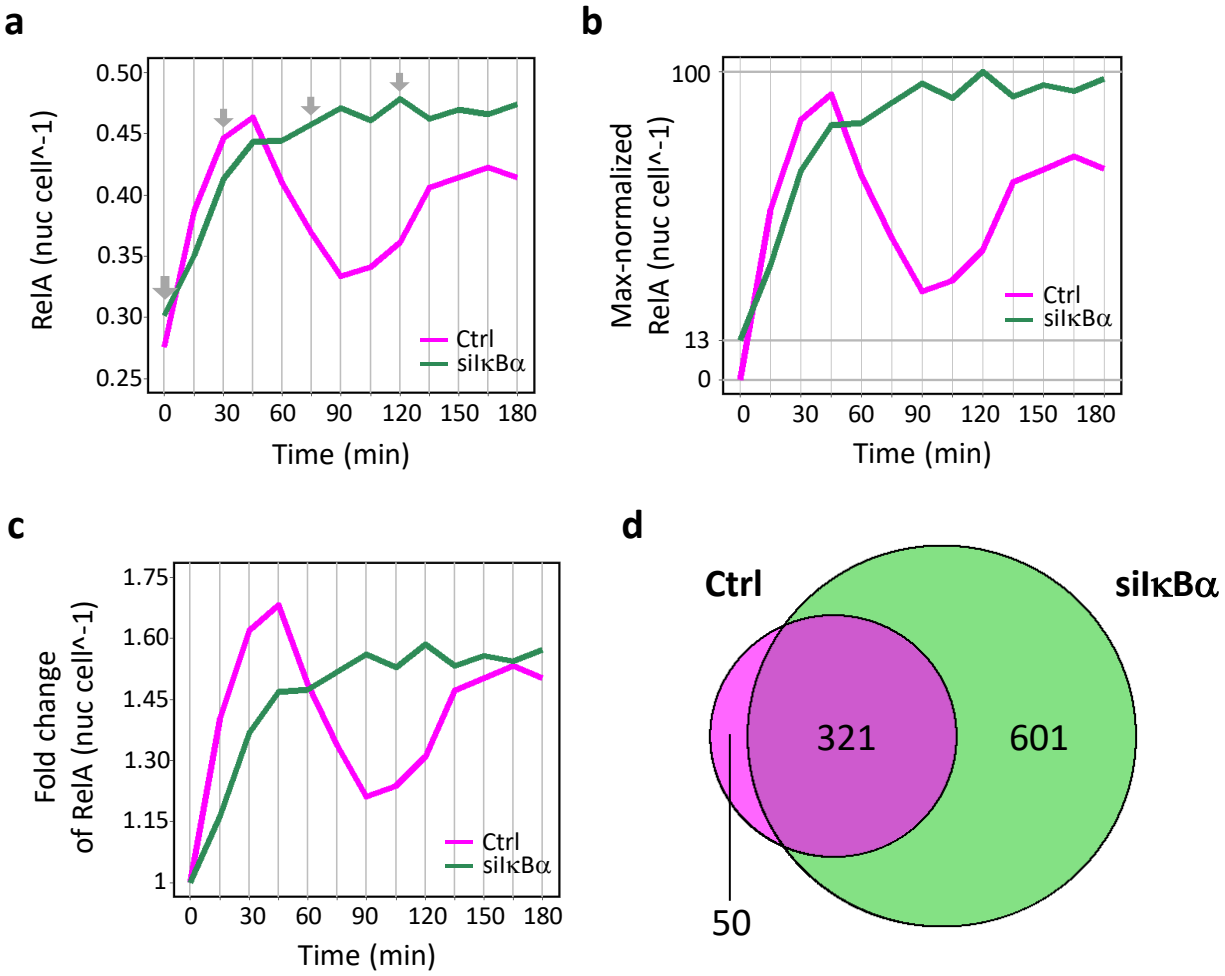

Figure 10. Dynamics of nuclear NFκB abundance and differentially expressed genes (DEGs)

Time course nuclear NFκB abundance (a) and time course NFκB abundance of two biological replicates which were max-normalized together from 0 to 100 (b), and fold change (c) from fixed-cell immunofluorescence of MCF-7 cells treated with 1 ng mL^-1 TNF in Ctrl (Control) and siIκBα (IκBα knockdown). Line graphs represent the means of two biological replicates. Number of cells used to calculate the mean for each time point ranged from 1336 to 2374 cells. Grey lines indicate the time points where RNA-seq data was measured, and arrows indicate the time points where single-cell ATAC-seq data was measured. Statistical significance was observed for interpolated (same method used in mathematical modeling) time course nuclear NFκB abundance (p-value: 1.039e-4) and fold change (p-value < 2.2e-16) between Ctrl and siIκBα from before stimulation and 75 minutes (the first peak time point of early response genes) after stimulation by one-tailed Wilcoxon rank sum test. (d) Venn diagram of the TNF-induced DEGs in Ctrl and siIκBα.

To investigate how IκBα-regulated NFκB localization affects the expression of its target genes, bulk RNA-sequencing at early time points (0-180 min) after stimulation with TNF in the presence (control) or absence of IκBα (siIκBα) were performed. RNA levels were measured every 15 minutes after stimulation to produce detailed expression patterns and identified 371 and 922 differentially expressed genes (DEGs) in control and siIκBα cells, respectively. Then, the DEGs in two conditions were compared and 321 overlapping DEGs in both conditions (Figure 10d) were identified. To observe the expression dynamics of DEGs in control cells, fuzzy c-means clustering was performed and 371 DEGs in control cells were classified into five gene clusters: early response genes (ERGs), intermediate response genes (IRGs), delayed response genes (DRGs), downregulated, and others (Figure 11a). To investigate genes that were differentially expressed in siIκBα but not in control, 601 DEGs that were unique to siIκBα were selected (Figure 10d) and clustered into three groups: upregulated, downregulated, and others (Figure 11b).

As the fold change in the expression level of a target gene is proportional to the fold change in the activity of the transcription factor when they participate in an incoherent feedforward loop[46,54], the fold change in expression between control and siIκBα for genes in each TNF-induced cluster were statistically compared. For the ERGs, IRGs, and DRGs, the fold change in gene expression at some time points were significantly higher in control cells (Figure 11a). In contrast, the mean fold change in the expression of upregulated genes that were unique to siIκBα cells was consistently lower in control cells after stimulation (Figure 11b). Furthermore, whether this gene cluster includes genes that are regulated by NFκB was investigated by performing motif analysis. This was performed at the promoter regions ($\pm$500 bps Transcription Start Site (TSS)) of

195 protein-coding genes among 214 upregulated genes, but none of the NFκB subunit binding motifs were significantly enriched (Figure 11c). Results indicated that most TNF-induced DEGs that were upregulated only in siIκBα were unlikely to be controlled by NFκB.

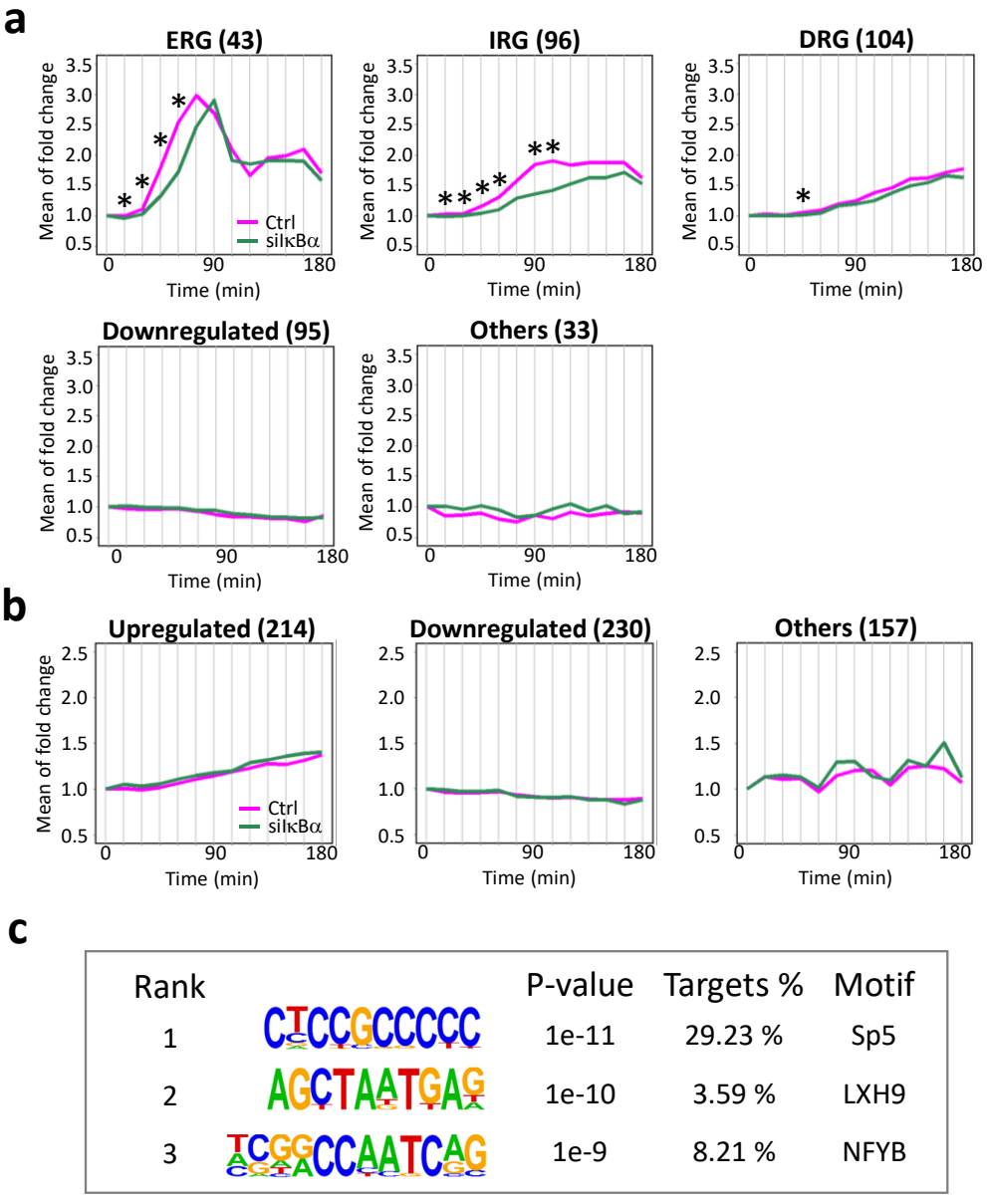

Figure 11. Mean fold change in expression of clusters of differentially expressed genes (DEGs)

(a) Mean of fold change in expression of five TNF-induced clusters (ERG, IRG, DRG, Downregulated and Others) of DEGs in Ctrl. For these 5 clusters, statistical tests were performed for fold change in expression between Ctrl and siIκBα (*: p-value < 0.01 by one-tailed Wilcoxon rank sum test). (b) 601 DEGs that were unique to siIκBα were classified into upregulated, downregulated and others clusters. Line graphs show the mean of time course fold change in expression. (c) Motif analysis results at the promoter regions of the upregulated DEGs that were unique to siIκBα condition.

To analyze the ERGs, IRGs, and DRGs in more detail, each of the clusters was further classified into two subclusters (Figure 12a). For each gene cluster, genes in subcluster 1 showed a similar fold change in expression between control and siIκBα, and genes in subcluster 2 showed a statistically higher fold change in expression in the control than in siIκBα. Motif analysis was performed at the promoter regions of each subcluster from the ERGs, IRGs, and DRGs, and found that a subcluster 2 from all three showed a significantly enriched NFκB binding motif, while only subcluster 1 from the ERGs showed a significant enrichment (Figure 12b). These data show that NFκB is involved in the induction of many TNF-responsive genes, and indicate that IκBα functions not only as a negative feedback regulator[4,55] of NFκB, but also as an enabler of NFκB-regulated stimulus-responsive gene expression.

a

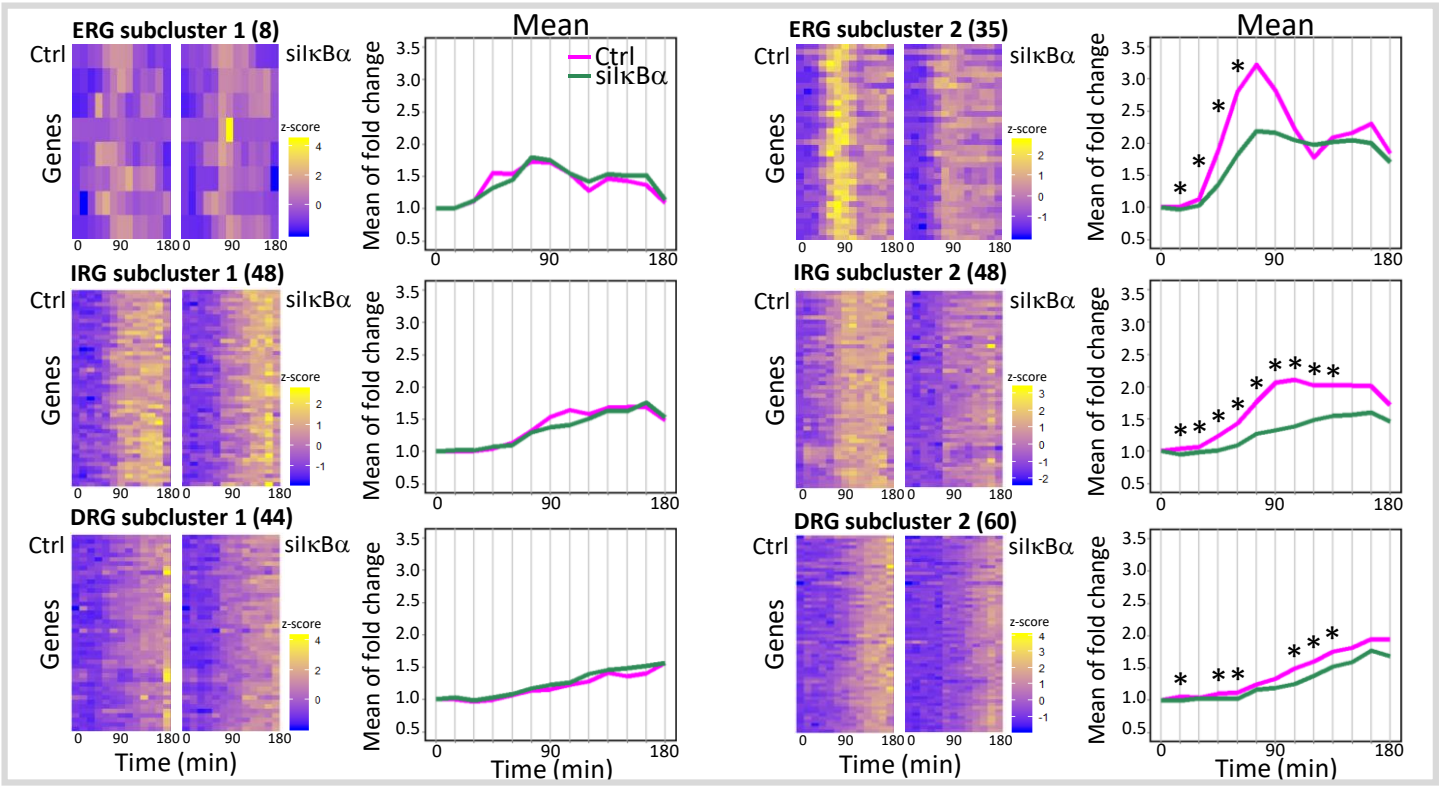

b

		P-value	Targets %	Motif
ERG subcluster 1		1e-6	20.00 %	NFκB-p65
ERG subcluster 2		1e-8	14.29 %	NFκB-p65-Rel

		P-value	Targets %	Motif
IRG subcluster 2		1e-9	27.08 %	NFκB-p65-Rel
DRG subcluster 2		1e-9	16.67 %	NFκB-p65-Rel

Figure 12. Subclusters of upregulated differentially expressed genes (DEGs) in Ctrl (Control)

(a) Two subclusters for each TNF-induced cluster (ERG, IRG, and DRG) in Ctrl (outlier *PCSK5* gene excluded). For these 6 subclusters, statistical tests were performed for fold change in expression between Ctrl and siIκBα (*: p-value < 0.01 by one-tailed Wilcoxon rank sum test). (b) κB motifs that were enriched at promoter regions (± 500 bps TSS) of ERG subclusters 1 and 2, IRG subcluster 2, and DRG subcluster 2.

5.2 NFκB control of chromatin accessibility in the presence or absence of IκBα

To examine how NFκB binding sites (κB sites) are affected by NFκB activation in the presence or absence of IκBα in individual cells, a single-cell assay for transposase-accessible chromatin using sequencing (ATAC-seq) was performed for early time points (0, 30, 75, and 120 minutes) after stimulation with TNF for control and siIκBα in MCF-7 cells. These time points were selected based on those that showed the maximum and minimum early time course (0–180 minutes) nuclear NFκB abundance (Figure 10a). After sample curation, the remaining 989 and 953 single-cell samples in control and siIκBα, respectively, were aligned to the genome and their chromatin accessibility was quantified. Furthermore, the chromatin accessibility of the aggregated samples for each condition was quantified and the peak regions for each time point were identified.

Using these peak regions in the aggregated data, peak regions of the ATAC-seq signal that were significantly induced at each time point after TNF stimulation were identified. Within these 3,643 regions in total, regions that did not show higher chromatin accessibility after TNF stimulation than before were filtered out when TMM normalization was applied to normalize the chromatin accessibility. As a result, 833, 704, and 1,889 regions were induced at 30, 75, and 120 minutes, respectively, in control cells (Figure 13a). Then, all 3,182 regions were clustered based on their time-course chromatin accessibility. These regions were clustered into 13 groups based on their time-course patterns (Figure 13b).

Next, motif analysis at these TNF-induced ATAC peak regions in control cells was performed to capture the trend of the time-course chromatin accessibility pattern of TNF-induced κB sites and to identify transcription regulators other than NFκB. There

were five clusters that showed significant enrichment of κB sites (Figure 13c), including binding sites for the interferon regulating IRF4[56] and inflammatory cytokine regulating AP-1 subunit[57] (Figure 13d). Furthermore, only the regions that were significantly enriched with κB sites from each of these clusters (Figure 13c) were extracted. The patterns of these extracted regions in each cluster reflected the nuclear NFκB abundance in control, showing a high chromatin accessibility at 30 and 120 minutes, which corresponds to the first and second peaks, respectively, of nuclear NFκB activity (Figure 13e).

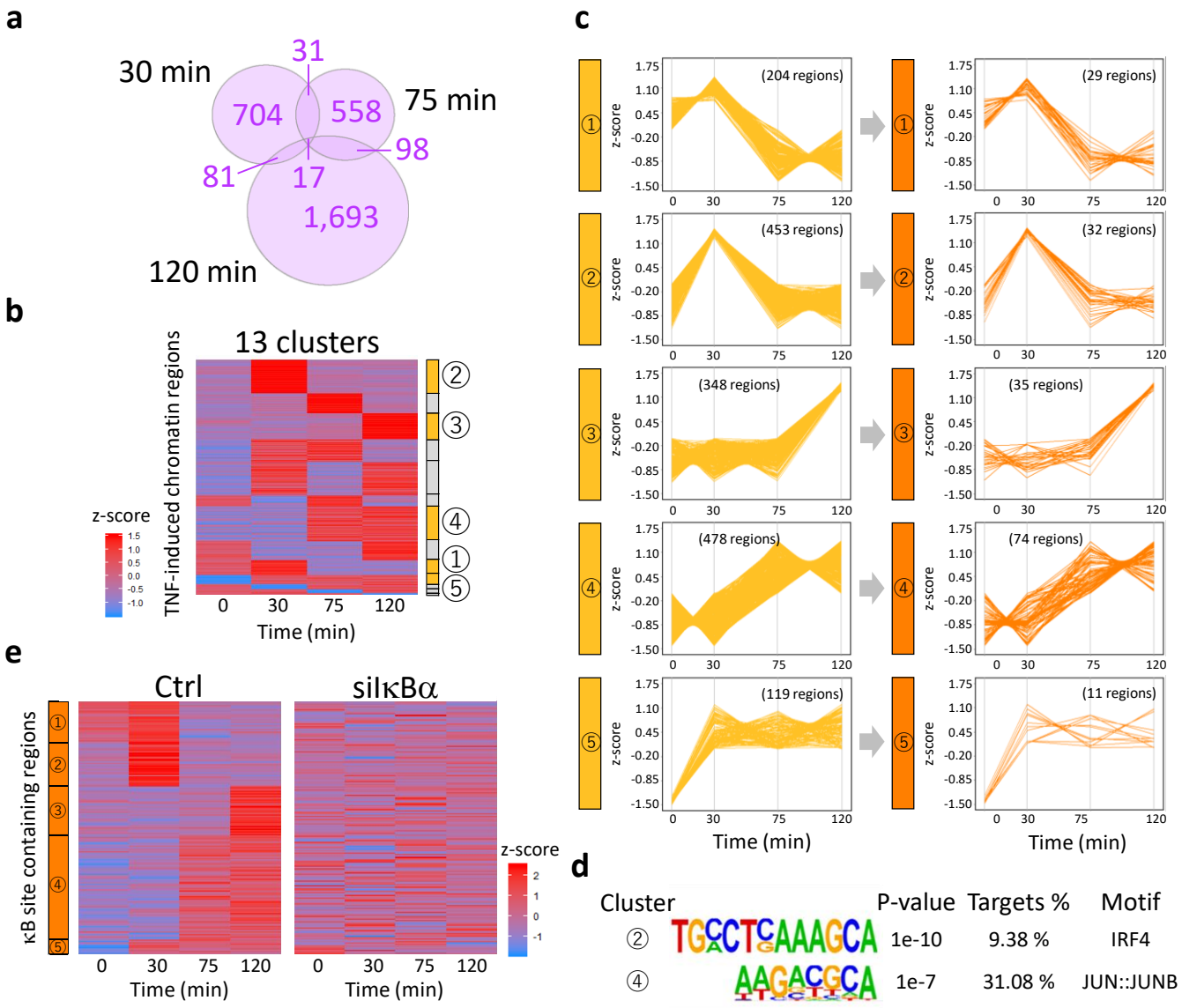

Figure 13. TNF (Tumor Necrosis Factor)-induced chromatin regions and dynamics of chromatin accessibility in κB sites

(a) Venn diagram of the number of TNF-induced chromatin regions at each time point in Ctrl (Control). (b) Regions in (a) clustered into 13 time course clusters. Chromatin accessibility was normalized to z-score, where red shows high chromatin accessibility and blue shows low chromatin accessibility in the heatmap. (c) Clusters enriched with κB sites and extracted κB site detected regions. Time course chromatin accessibility was z-score normalized for each κB site enriched region. Numbers in braces show the number of regions before and after κB site enriched regions were extracted for each cluster. (d) Motif analysis results showed that AP-1 and IRF4 binding sites were also enriched at κB site enriched clusters in Ctrl. (e) Time course chromatin accessibility in Ctrl and siIκBα (IκBα knockdown) at κB site detected regions in (c). Chromatin accessibility was normalized to z-score, where red shows high chromatin accessibility and blue shows low chromatin accessibility in the heatmap.

Similarly, 3,571 out of 4,079 TNF-induced regions that were upregulated in siIκBα were identified. These regions were clustered into 13 groups (Figure 14a), and motif analysis was performed to capture the trend of time-course chromatin accessibility. Five clusters were obtained which showed significant enrichment of κB sites, including IRF4 and AP-1 binding sites (Figure 14a). Then, only the regions that were significantly enriched with κB sites from each of these clusters (Figure 14b) were extracted. The time course patterns of these extracted regions in each cluster reflected the nuclear NFκB abundance in siIκBα, showing high and prolonged chromatin accessibility at late time points (Figure 14c).

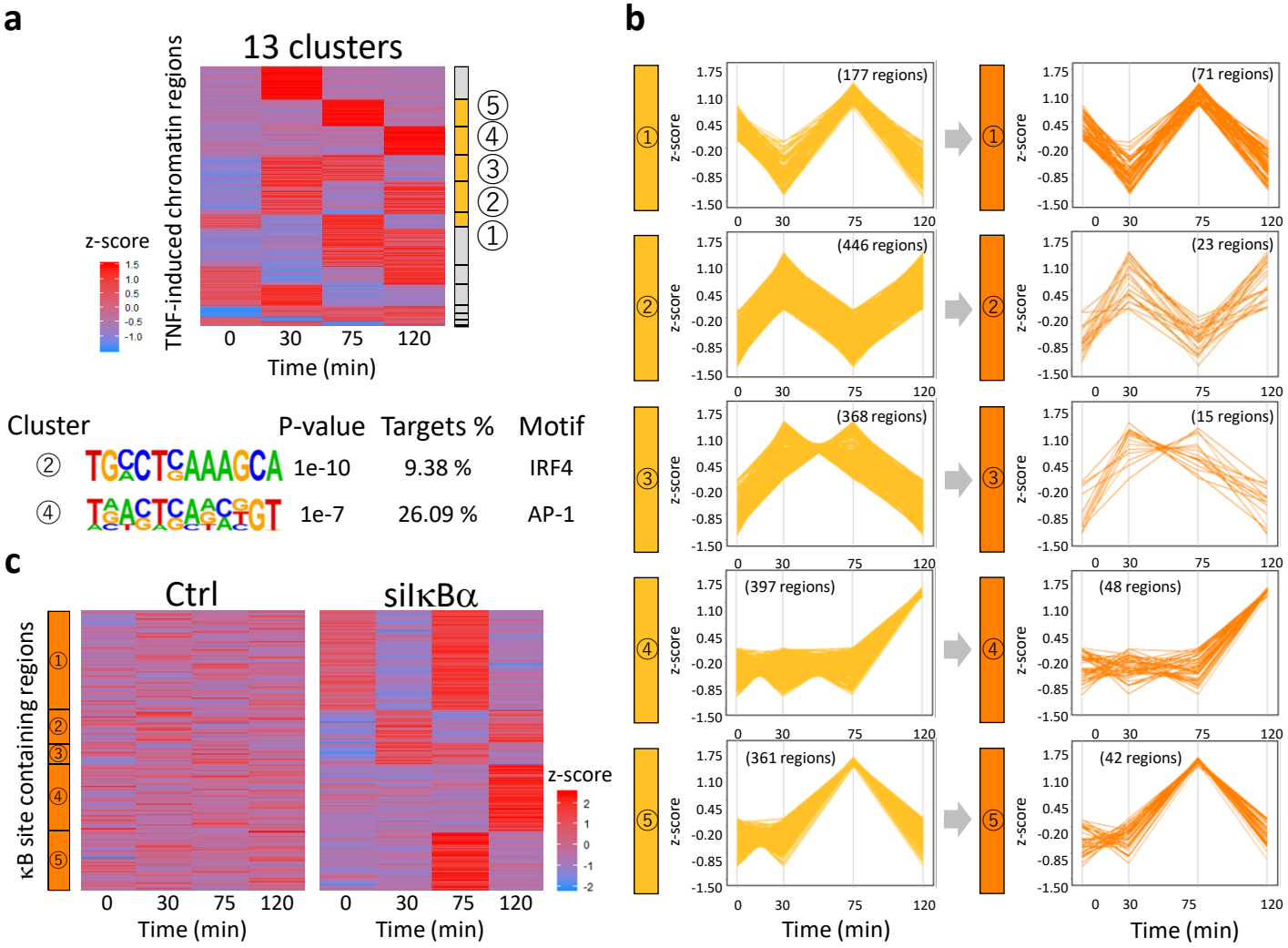

Figure 14. Dynamics of chromatin accessibility in κB sites after TNF (Tumor Necrosis Factor)-induction in siIκBα

(a) TNF-induced regions in siIκBα classified into 13 time course clusters and identified 5 clusters which were enriched with κB sites. Chromatin accessibility was normalized to z-score, where red shows high chromatin accessibility and blue shows low chromatin accessibility in the heatmap. In addition to the enrichment of κB sites, these clusters also showed enrichment of AP-1 and IRF4 binding sites. (b) Clusters enriched with κB sites and extracted κB site detected regions in siIκBα. Time course chromatin accessibility was z-score normalized for each κB site enriched region. (c) Time course chromatin accessibility in Ctrl (Control) and siIκBα at κB site detected regions in siIκBα, and comparison of time course chromatin accessibility between two conditions at κB site-enriched regions in siIκBα. Chromatin accessibility was normalized to z-score, where red shows high chromatin accessibility and blue shows low chromatin accessibility in the heatmap.

To confirm the statistical difference between chromatin accessibility at the TNF-induced clusters in the presence and absence of IκBα, the aggregated time course chromatin accessibility for each cluster in control and siIκBα cells were calculated and a one-tailed Wilcoxon rank sum test was performed between the two conditions for each cluster at each time point (Figure 13e, 15a, 14c and 15b). Furthermore, to investigate whether individual control and siIκBα cells can be distinguished by chromatin accessibility at these TNF-induced regions between the presence and absence of IκBα or not, a 10-fold cross validation using Bayesian generalized linear model was performed.

As a result, substantial statistical significance (p-value $<$ 0.0001) from aggregated cells and classification accuracy of more than 60 % from single-cells were observed at 30 minutes and 120 minutes of TNF-induced regions in the presence of IκBα, which corresponded to the peak of nuclear NFκB abundance in control (Figure 13e and 15a, cluster 2 at 30 minutes and cluster 3 at 120 minutes). However, TNF-induced regions in the absence of IκBα showed these statistical significance and classification accuracy at only late time points (Figure 14c and 15b, cluster 1 and 5 at 75 minutes and cluster 4 at 120 minutes). These results suggest that IκBα is responsible for the rapid NFκB activation dynamics that allows NFκB to mediate early chromatin activation.

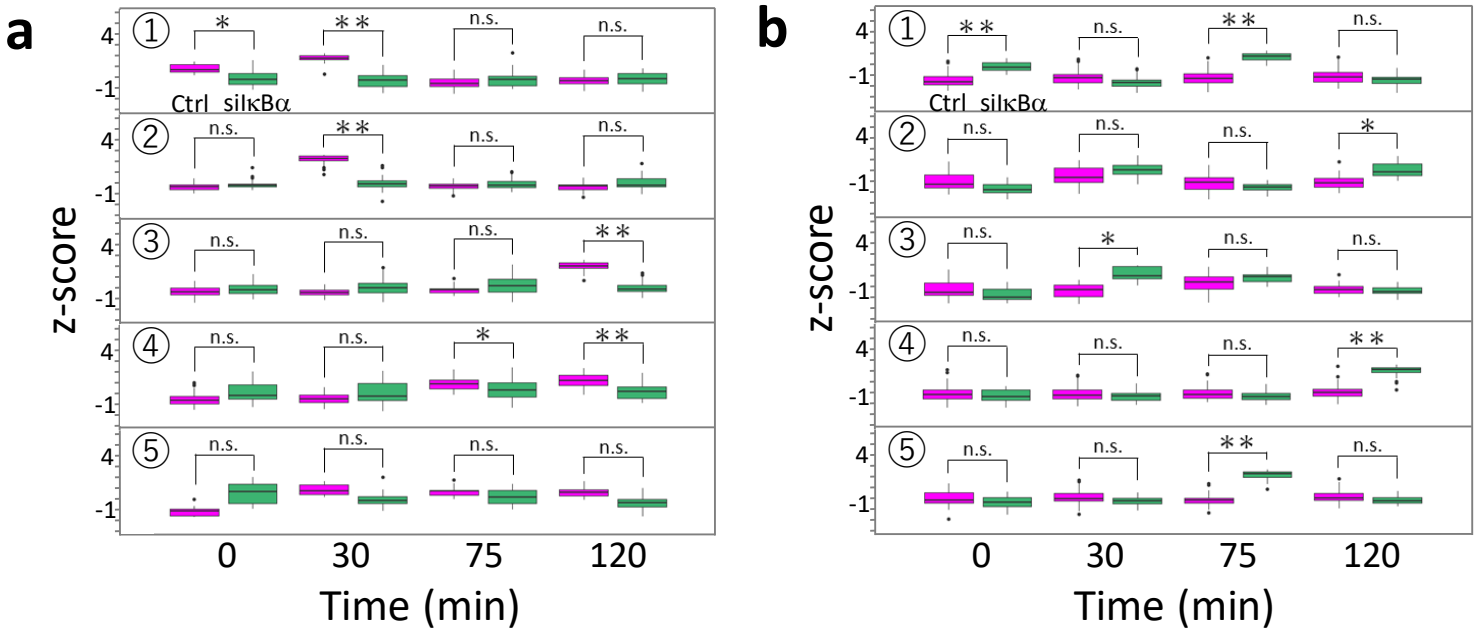

Figure 15. Statistical significance of aggregated chromatin accessibility between Ctrl (Control) and siIκBα

Comparison of time course chromatin accessibility between 2 conditions at κB site-enriched regions in Figure 6e are shown in (a), and κB site-enriched regions in Figure 7c are shown in (b). Statistical tests were performed for chromatin accessibility between Ctrl and siIκBα at these regions in Ctrl and siIκBα (*: p-value < 0.01, **: p-value < 0.0001 and n.s.: p-value $\geq$ 0.01 by one-tailed Wilcoxon rank sum test). The center line indicates the median, the upper and lower hinges indicate the first and third quartiles, the upper whisker extends from the hinge to the largest value no further than 1.5 $\times$ IQR (interquartile range) from the hinge, the lower whisker extends from the hinge to the smallest value at most 1.5 $\times$ IQR of the hinge, and the points indicate the outliers.

5.3 A simple mathematical model accounts for many DRGs in subcluster 2

The expression pattern of ERGs, IRGs, and DRGs in subcluster 2 in control cells followed a similar pattern with the time course nuclear NFκB dynamics. However, whereas nuclear NFκB activity time course showed a prolonged pattern in siIκBα, many ERGs showed post-induction repression. This implies that there is a post-induction repression mechanism of transcriptional control that is independent of IκBα.

To unravel this mechanism, a simple mathematical model (Figure 6) was applied to the data on the nuclear NFκB activity and its target genes to identify the regulatory mechanisms (detailed description in Methods). To recapitulate the time-course fold change in expression observed in the RNA-seq data, the fold change of input nuclear NFκB activity was calculated and scaled to avoid assay-specific reductions in the dynamic range for two biological replicates of NFκB translocation data (Figure 16).

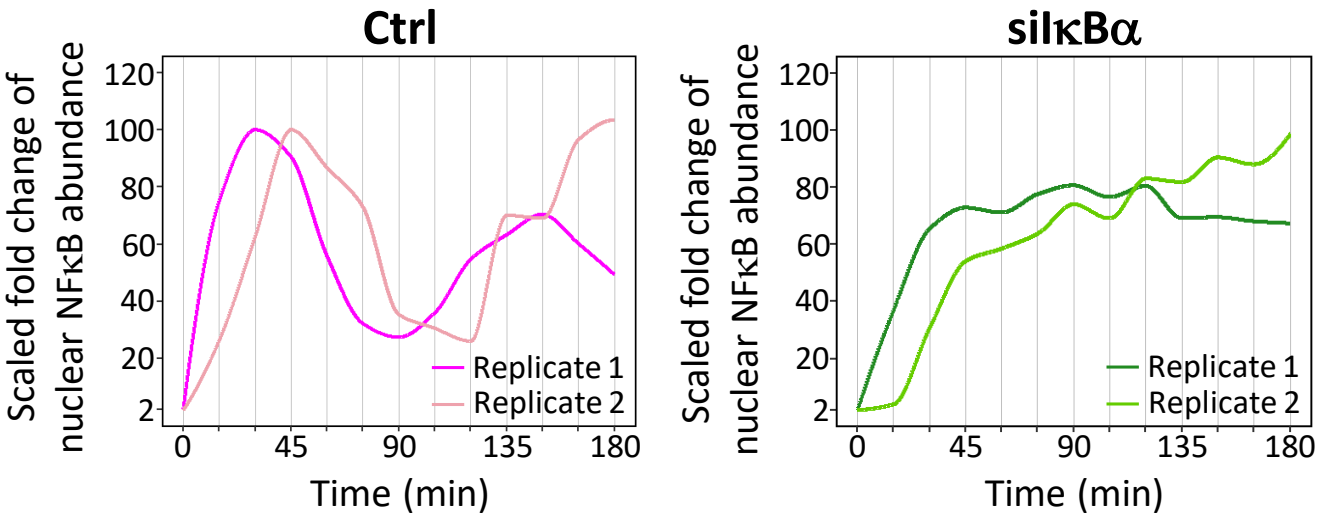

Figure 16. Scaled fold change of nuclear NFκB abundance in Ctrl (Control) and siIκBα
For replicate 1, fold change for all time points in each condition were calculated. Fractional nuclear RelA abundance (nuc cell^-1) in Ctrl and siIκBα were normalized together to span a range of 2 – 100 (50-fold) to avoid assay specific reductions of the dynamic range. For replicate 2, after calculating the fold change for all time points in each condition, fractional nuclear RelA abundance (nuc cell^-1) in Ctrl was normalized to span a range of 2 – 100 to standardize the maximum activity with the scaled Ctrl data in replicate 1. Then, the measured data in siIκBα was normalized using the same scale used in Ctrl. Parameters were optimized from the concordant parameter set using the simple model of replicate 1 and replicate 2 for each gene are plotted in dots. They showed positive correlation between the 2 replicates.

The parameters of the model for each biological replicate were optimized, and parameter sets that were the most concordant among the 10,000 pairs of two biological replicates according to the Pearson correlation coefficients were identified (Figure 17) to justify each parameter value.

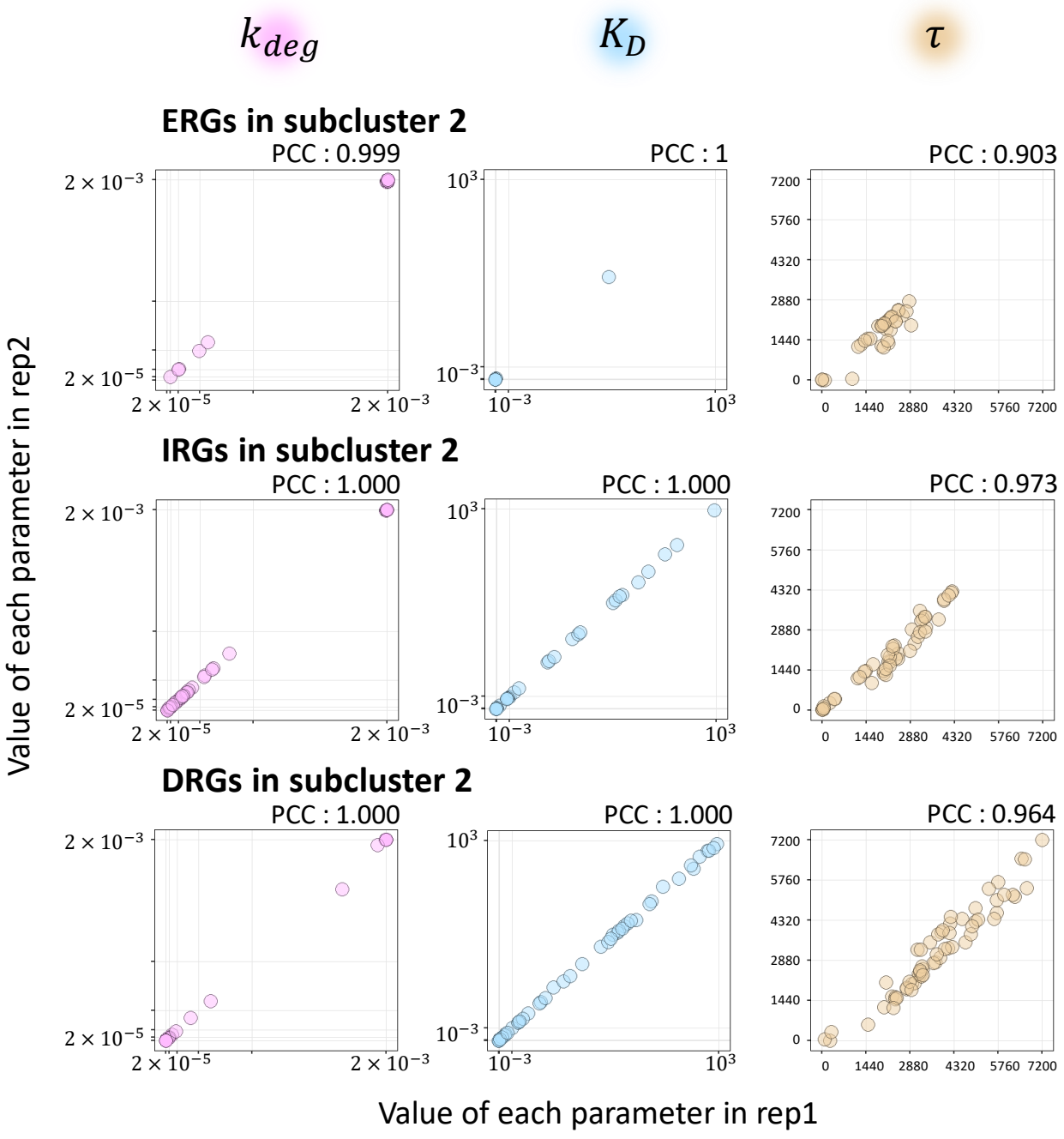

Figure 17. PCC (Pearson Correlation Coefficient) of the values of each optimized parameter using the simple model

Parameters were optimized from the concordant parameter set using the simple model of replicate 1 and replicate 2 for each gene are plotted in dots. They showed positive correlation between the 2 replicates.

Then, the fold change in expression using these concordant parameter sets were simulated and whether the model was acceptable for each gene was examined. To examine this, a definition referring to the results of the RNA-seq data analysis (Figure 12a) was established. First, to be a good fit, the nRMSD (normalized Root Mean Square Deviation) values in replicates 1 and 2 of the control set should be smaller than 0.5, and the nRMSD values in replicates 1 and 2 of the siIκBα should be smaller than 0.39. In addition, since all ERGs, IRGs, and DRGs in subcluster 2 showed a larger value in the control than in siIκBα for at least either their max-fold induction (MFI) or the area under the curve (AUC), a definition that at least either the simulated MFI or AUC should also show the same relationship (control > siIκBα) to be a good fit (Figure 18a) was established.

In subcluster 2, there were 5 out of 34 ERGs, 19 out of 48 IRGs, and 50 out of 60 DRGs that showed a good fit (Figure 18b). Many DRGs showed a good fit with this model, and the fold change in expression was similar between control and siIκBα, showing a monotonically increasing expression pattern. Representative good-fit DRGs included *LTB*, which encodes a membrane protein that promotes inflammation through the activation of the NFκB signaling pathway[58], and *RELB*, which encodes a protein that is a subunit of NFκB complex that is involved in immune tolerance to inflammation[59]. However, this model failed to recapitulate the patterns of many ERGs and IRGs in subcluster 2, especially ERGs in subcluster 2 that showed post-induction repression. Thus, this result implies additional gene regulatory mechanisms.

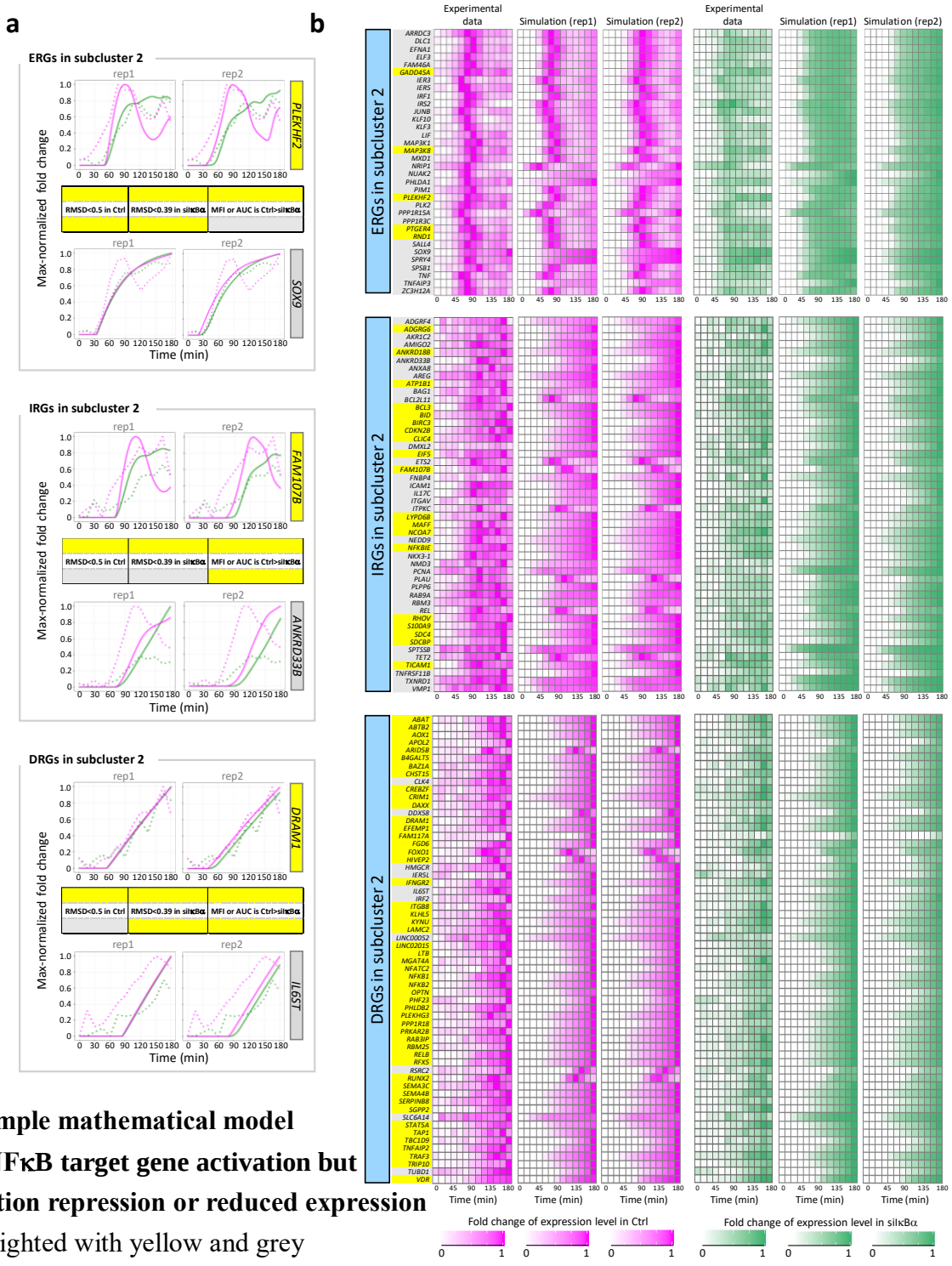

Figure 18. A simple mathematical model recapitulates NFκB target gene activation but not post-induction repression or reduced expression

(a) Genes highlighted with yellow and grey indicate whether the model is acceptable or not. Line graphs of representative genes from ERGs in subcluster 2, IRGs in subcluster 2 and DRGs in subcluster 2 showing good and bad fits between the simulation results and the experimental data. Yellow color bars show that simulation were acceptable for both replicates, and grey color bars show that simulation was not acceptable for at least either one of the replicates based on the definition.

(b) Heatmaps of the time course gene expression from experimental results and data-fit from the simple model.

5.4 The incoherent feedforward loop model accounts for reduced expression in siIκBα

Previous studies have revealed that transcription networks contain recurring regulation patterns, such as feedforward loops (FFLs)[60]. It is known to appear in hundreds of gene systems in multiple organisms, and among the multiple FFL types, two of them are known to occur much more frequently than others[61–63]. The first type is called the coherent type-1 FFL (C1-FFL) and the second type is called the incoherent type-1 FFL (I1-FFL). In the C1-FFL, when signal appears, X becomes active and rapidly binds its downstream promoter of Y and Z for activation, and Y also binds to Z for activation (Figure 19a)[60]. As a result, Z production continues as long as the signal is not removed and Y concentration crosses the activation threshold. On the other hand, in the I1-FFL, when signal appears, X activates Z, but also represses Z by activating repressor Y. As a result, when a signal causes X to activate, Z is rapidly produced (Figure 19b)[60]. However, after some time, Y levels accumulate to reach the repression threshold for the Z promoter. As a result, Z production decreases and its concentration drops, resulting in pulse-like dynamics. A previous study revealed that the transcriptional regulation by NFκB in HeLa cells was robustly explained by this I1-FFL[46].

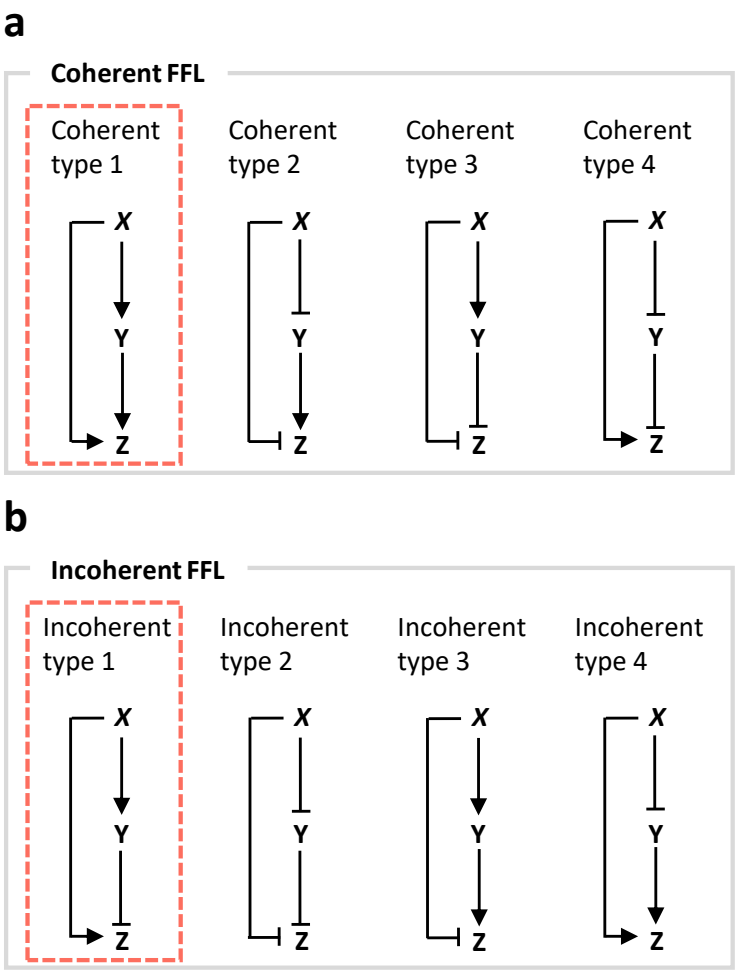

Figure 19. Feedforward loops (FFLs)

Eight types of feedforward loops (FFLs)[60]. Coherent type-1 FFL (C1-FFL) and incoherent type-1 FFL (I1-FFL) are frequently observed in multiple organisms.

Hence, since the simple model was insufficient to describe the post-induction repression mechanism, this previously introduced IFFL model describing NFκB transcriptional regulation[46] (I1-FFL) was applied (Figure 7). The IFFL model detects the fold change in the nuclear NFκB abundance, and reflects this change on gene expression. This model demonstrates a NFκB-regulated competitor transcription factor that competitively binds to the NFκB target gene promoter region. From among the ERGs, IRGs, and DRGs, TNF-induced DEGs, which are also NFκB target genes were searched, for possible NFκB competitors[46]. The *NFKB1* gene was identified, which is processed into p50 as the only competitor. The processing time of p50 was defined from information gathered from previous studies and fixed the time between nuclear p50 translocation and mature poly A^+ mRNA production as 2 hours[47,48] (detailed description in Methods). After fixing the processing time, this model was applied to the ERGs, IRGs, and DRGs in subcluster 2 by using the same parameter optimization flow, identification process of concordant parameter sets (Figure 20), and the definition of a good fit as those used for the simple model analysis.

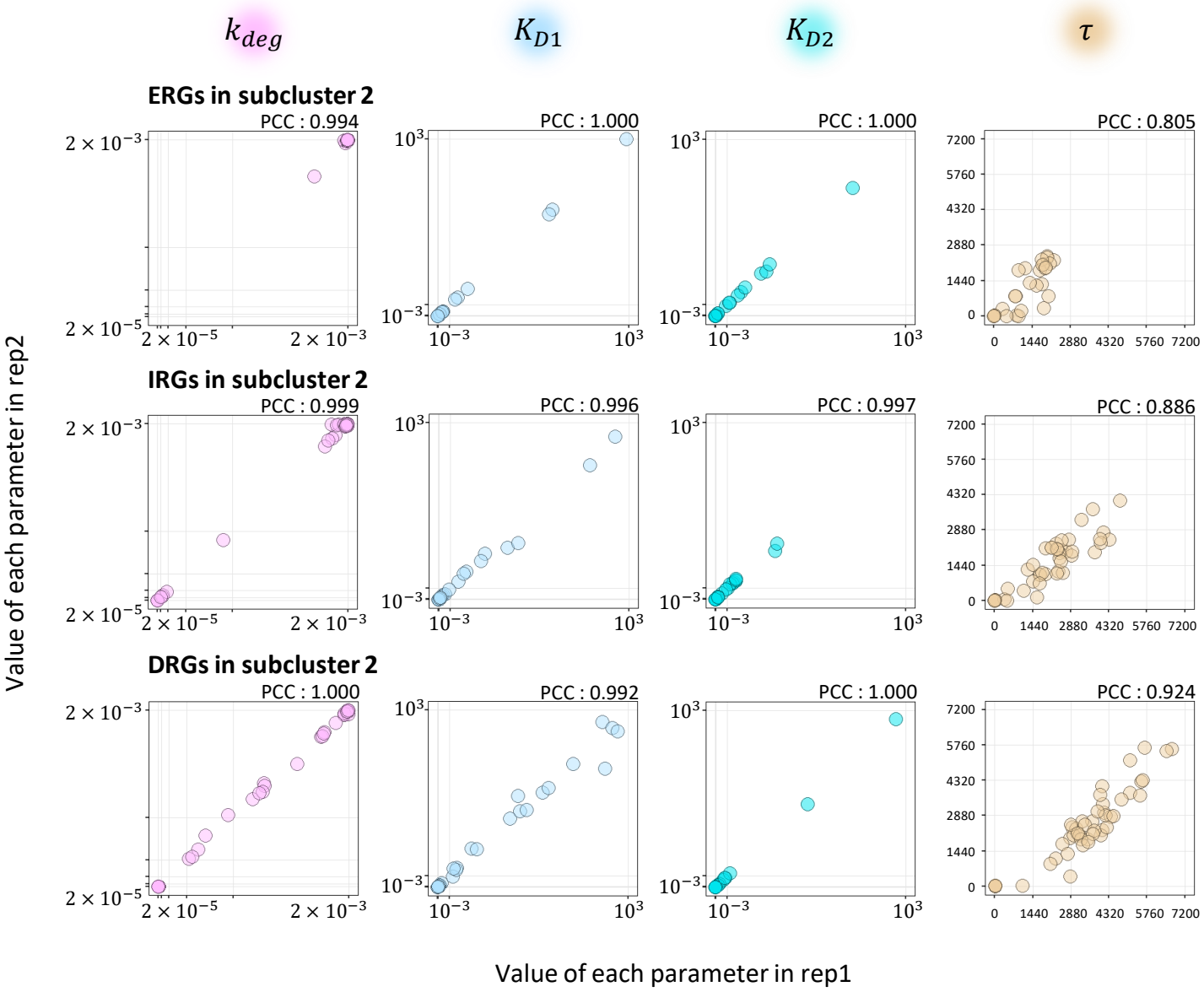

Figure 20. PCC (Pearson Correlation Coefficient) of the values of each optimized parameter using the IFFL (incoherent feedforward loop) model

Optimized parameters from the concordant parameter set using the IFFL model of replicate 1 and replicate 2 for each gene are plotted in dots. They showed positive correlation between the 2 replicates.

In subcluster 2, there were 5 out of 34 ERGs, 5 out of 48 IRGs, and 23 out of 60 DRGs that showed a good fit (Figure 21a and 21b). The good fit genes in each cluster showed a reduced fold change in expression in siIκBα, similar to the nuclear NFκB activity fold change in siIκBα, which showed a lower fold change level than in control (Figure 21a). The IFFL model detects the nuclear NFκB activity fold change, and thus the fold change in gene expression closely follows this reduction in siIκBα. However, the transcription regulatory mechanisms for most ERGs and IRGs in subcluster 2 were not described by this model.

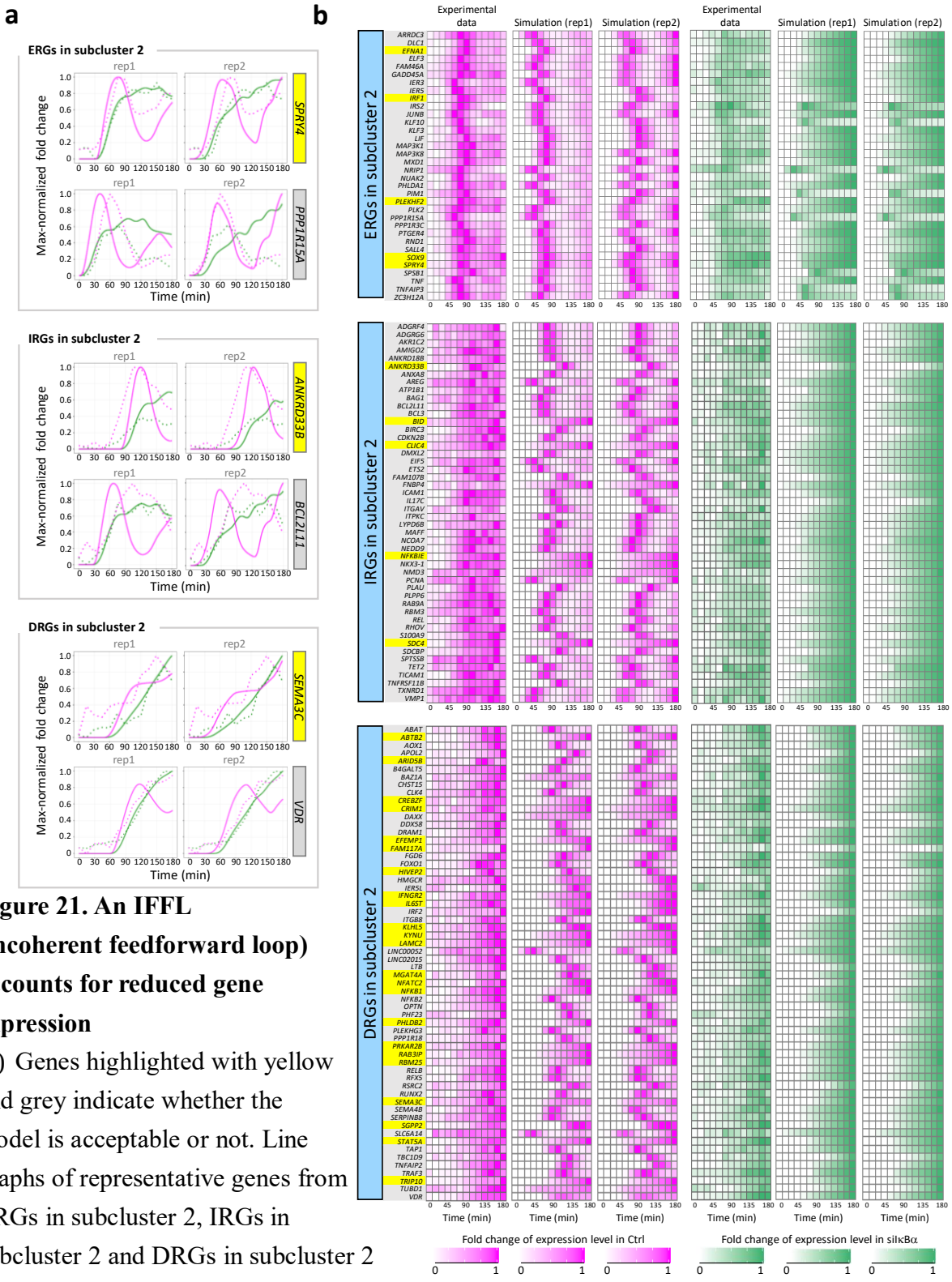

Figure 21. An IFFL (incoherent feedforward loop) accounts for reduced gene expression

(a) Genes highlighted with yellow and grey indicate whether the model is acceptable or not. Line graphs of representative genes from ERGs in subcluster 2, IRGs in subcluster 2 and DRGs in subcluster 2 showing good and bad fits between the simulation results and the experimental data.

(b) Heatmaps of the time course gene expression from experimental results and data-fit from the IFFL model.

5.4.1 A 3-state cycle model accounts for post-induction repression

The IFFL model was able to describe the reduced fold change in expression in siIκBα, but since many ERGs showed post-induction repression, a mechanism that physically inhibits the binding of NFκB after transcription inhibition was hypothesized. Therefore, a model that describes the transition of the promoter state was constructed (Figure 8). This model consists of nuclear NFκB, closed promoter state that is driven to an open promoter state, and the active promoter state that is driven by the open promoter state. The active promoter state is refractory and is driven to a closed promoter state (note that the rate constant of the regulation from the active state to the closed state may result from a combination of several transcriptional mechanisms, including the dissociation of NFκB). The active state also drives transcription, which includes the synthesis and degradation of mRNA. There are backward reactions between this closed chromatin state and open chromatin state, as well as between the open chromatin state and active chromatin state (detailed description in Methods). Post-induction repression may occur when the promoter state of a target gene changes from active to closed after nuclear NFκB translocation.

This model was applied to the ERGs, IRGs, and DRGs in subcluster 2 by using the same parameter optimization flow and the definition of a good fit as the simple model analysis. When fold change in expression was simulated with the concordant parameter set (Figure 22) for each gene in subcluster 2, there were 7 out of 34 ERGs, 24 out of 48 IRGs, and 55 out of 60 DRGs that showed a good fit (Figure 23a and 23b).

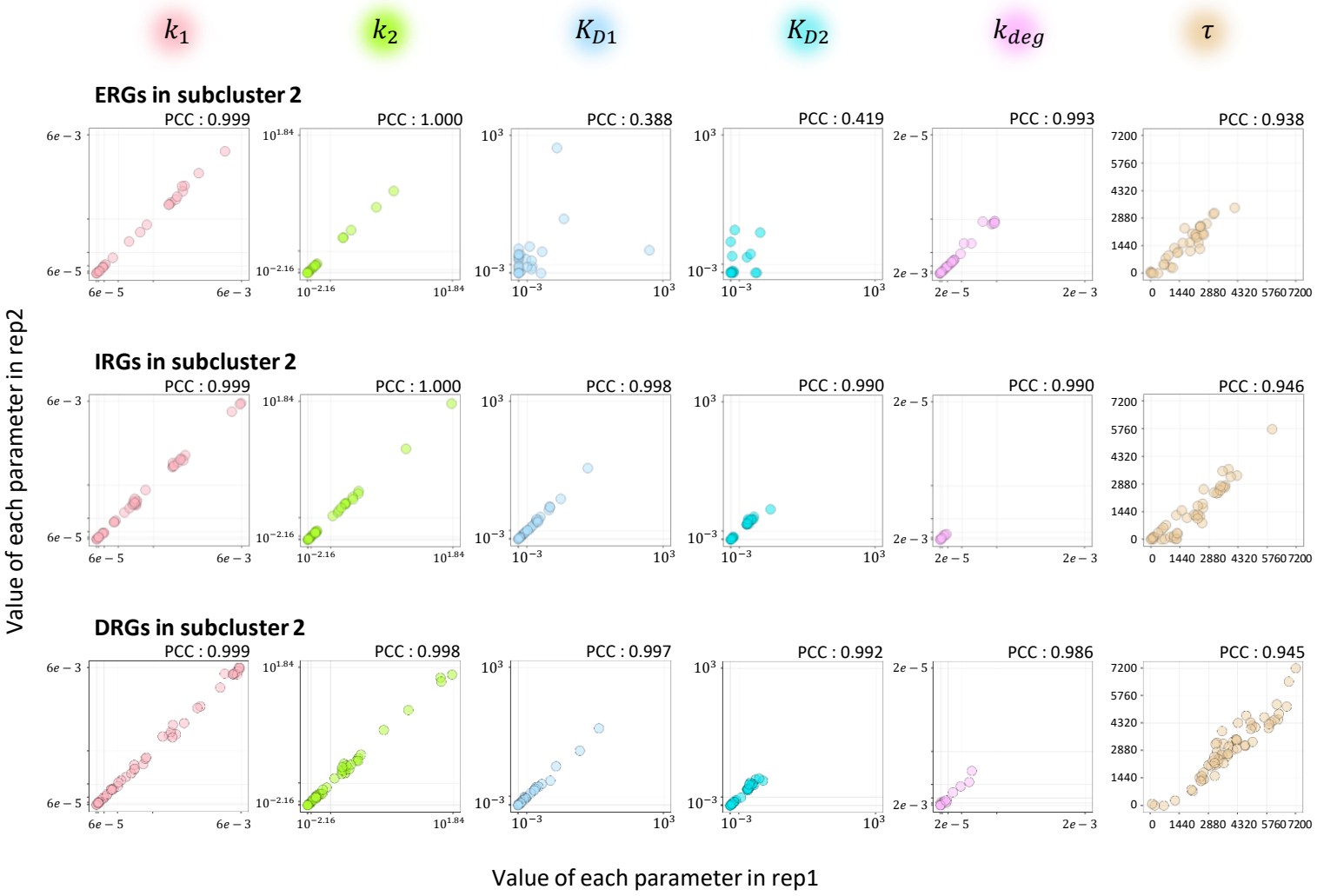

Figure 22. PCC (Pearson Correlation Coefficient) of the values of each optimized parameter using the 3-state cycle model

Optimized parameters from the concordant parameter set using the 3-state cycle model of replicate 1 and replicate 2 for each gene are plotted in dots. They showed positive correlation between the 2 replicates.

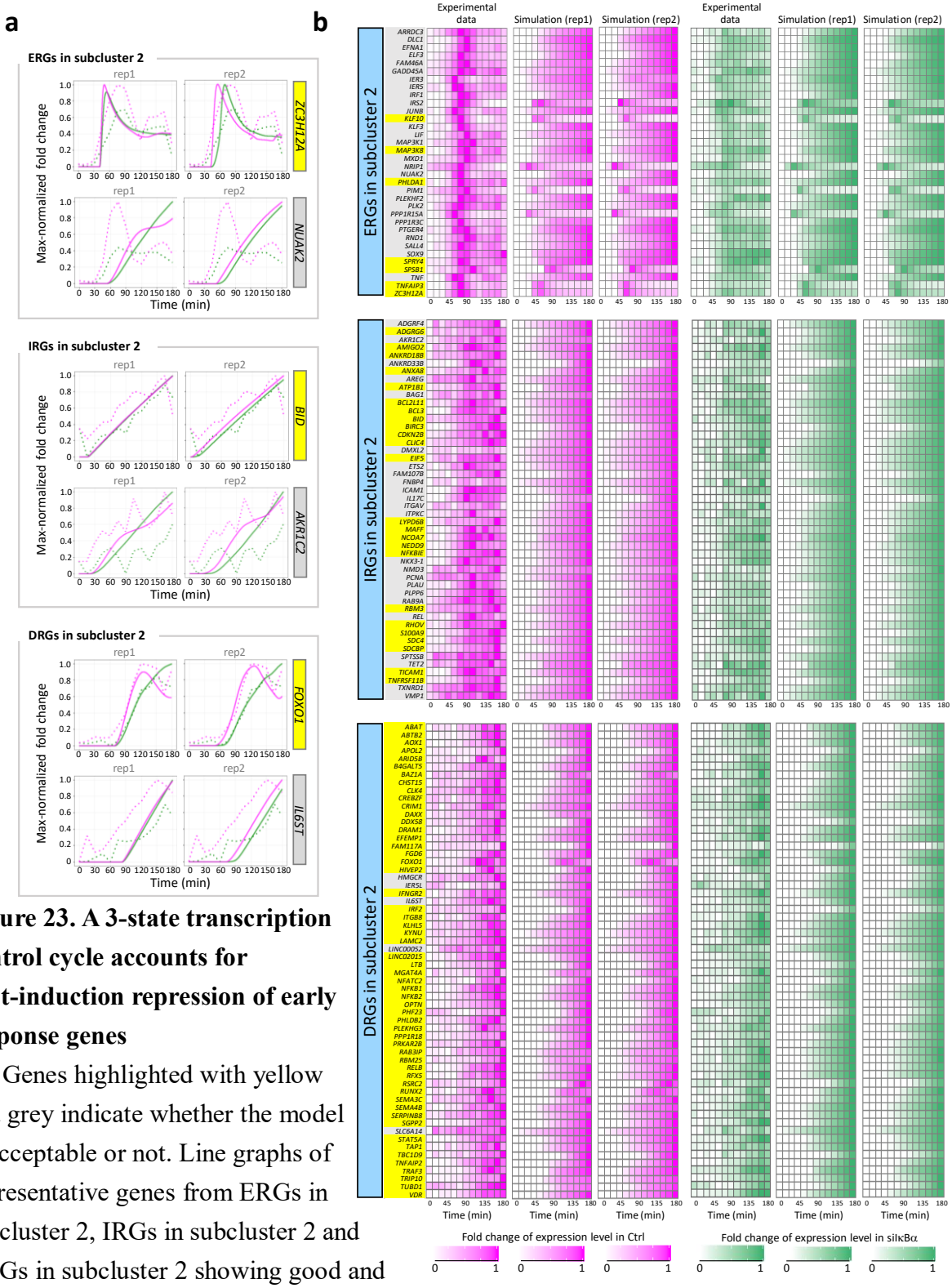

Figure 23. A 3-state transcription control cycle accounts for post-induction repression of early response genes

(a) Genes highlighted with yellow and grey indicate whether the model is acceptable or not. Line graphs of representative genes from ERGs in subcluster 2, IRGs in subcluster 2 and DRGs in subcluster 2 showing good and bad fits between the simulation results and the experimental data.

(b) Heatmaps of the time course gene expression from experimental results and data-fit from the 3-state transcription control cycle model.

A representative IRG, *BCL2L11*, which encodes a protein that functions as a tumor suppressor by inducing apoptosis[64], showed a good fit with this model. However, despite the presence of many ERGs in subcluster 2 that showed post-induction repression similar to the good fit genes in other clusters, there were only a few ERGs that showed a good fit with this model (Figure 23b). This was because many of the ERGs in subcluster 2 which showed post-induction repression also showed reduced expression in siIκBα.

5.5 A combined model v4 accounts for both post-induction repression and reduced expression

Finally, since many ERGs showed both post-induction repression and reduced expression in siIκBα, a model that combines the 3-state cycle model and the IFFL model was constructed by applying the previous three models (Figure 9). In this model, the NFκB competitor suppresses the NFκB target gene promoter in the active state, starting transcription of the target gene (detailed description in Methods). When the NFκB competitor suppression module was inserted in the closed state and open state, an error showed up and could not successfully simulate the time course fold change in expression. Hence, by adding the IFFL model to the 3-state cycle model in the active state, both post-induction repression and reduced expression were estimated to be observed at the same time.

This model was applied to the ERGs, IRGs, and DRGs in subcluster 2 by using the same parameter optimization flow and the definition of the good fit as the simple model analysis. When fold change in expression was simulated with the concordant

parameter set (Figure 24) for each gene in subcluster 2, there were 13 out of 34 ERGs, 12 out of 48 IRGs, and 38 out of 60 DRGs that showed a good fit (Figure 25a and 25b).

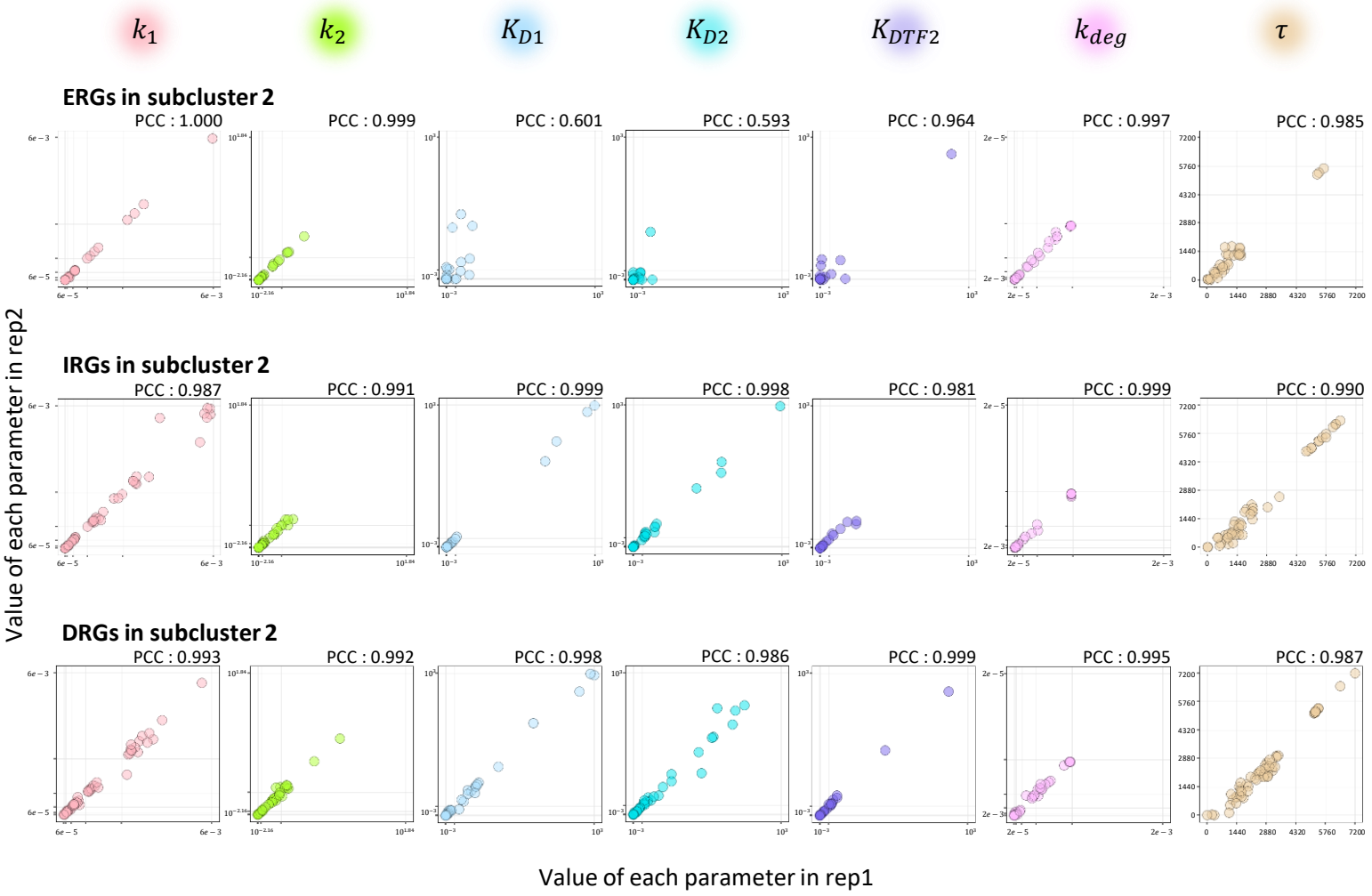

Figure 24. PCC (Pearson Correlation Coefficient) of the values of each optimized parameter using model v4
Optimized parameters from the concordant parameter set using model v4 of replicate 1 and replicate 2 for each gene are plotted in dots. They showed positive correlation between the 2 replicates.

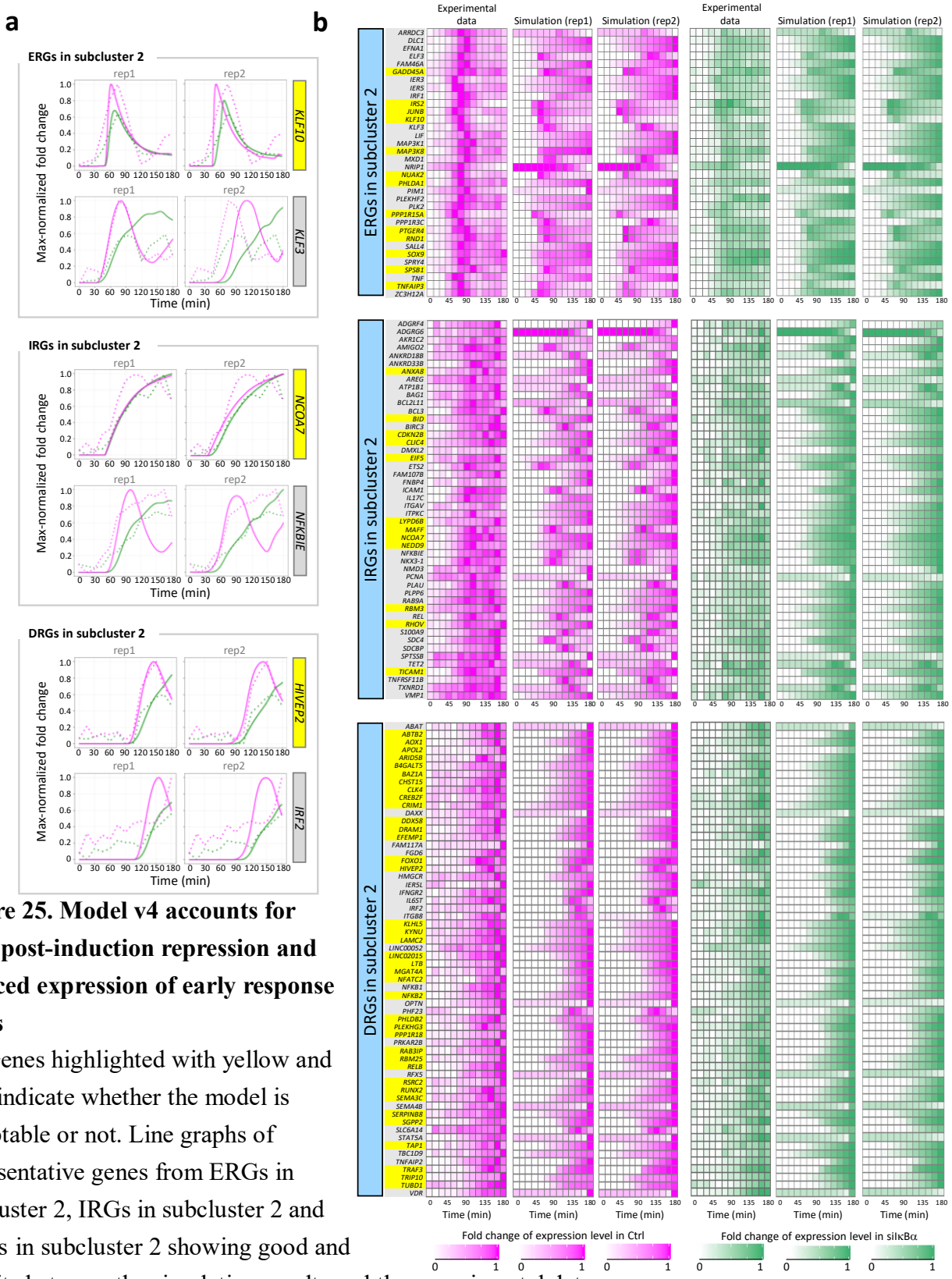

Figure 25. Model v4 accounts for both post-induction repression and reduced expression of early response genes

(a) Genes highlighted with yellow and grey indicate whether the model is acceptable or not. Line graphs of representative genes from ERGs in subcluster 2, IRGs in subcluster 2 and DRGs in subcluster 2 showing good and bad fits between the simulation results and the experimental data.

(b) Heatmaps of the time course gene expression from experimental results and data-fit from model v4.

This model was able to recapitulate many ERGs in subcluster 2, which showed both post-induction repression and reduced expression, indicating that the transition of promoter states and the suppression of transcription at the NFκB target gene promoter by the competitor protein are both required. In particular, inflammation and cancer-related early response genes (e.g., *A20* and *JUNB*) showed a transient fold change in expression. Overproduction of these genes results in inflammation, metastasis, invasion, and hormone-resistant phenotypes[57,65–67]. Among these genes, JUNB is a transcription factor that induces pro-inflammatory cytokines (e.g., TNF, IL-6, and IL-12)[57]. TNF and IL-6 possess both antitumor and protumor properties[68–71], whereas IL-12 promotes inflammation during the antitumor immune response[72,73]. The post-induction repression of these mechanisms might function as a brake for possible aberrant transcription induction of these cytokine-regulating transcription factors, which in turn safeguards against the overproduction of cytokines with protumor (e.g., TNF and IL-6) and excessive inflammation (e.g., IL-12) activities. While this repression acts as a brake for tumor progression and aberrant inflammation for some genes, it also acts as a suppressor of apoptosis, as observed for *KLF10*[74] (Figure 25a, 25b). Given that apoptosis suppresses tumor progression, these contradictory effects are controlled by a post-induction repression mechanism that safeguards gene expression from overproduction.

5.6 Identification of the best-fit model for each ERG, IRG, and DRG in subcluster 2

Four mathematical models were applied to each ERG, IRG, and DRG in subcluster 2 to identify the transcription mechanism of TNF-induced gene expression. At first, a simple model that considers only the relationship between the fold change in

nuclear NFκB activity and the transcription of its target gene was applied. This model recapitulated many DRGs in subcluster 2, which showed a similar level of fold change in expression between control and siIκBα, and a monotonically increasing expression pattern. However, most of the ERGs in subcluster 2 did not fit well with this model. Next, the IFFL model, which is a detectable fold-change model was applied. Since the fold change in nuclear NFκB is higher than that in siIκBα, reduced expression in siIκBα was recapitulated by this model. A few ERGs in subcluster 2 showed a good fit with this model, but many genes did not. To recapitulate post-induction repression, a 3-state cycle model was constructed and the good fit genes were identified. This model was able to recapitulate post-induction repression, but not reduced expression in siIκBα. Therefore, the model v4, which combines the 3-state cycle and IFFL models was constructed. This model was able to recapitulate both post-induction repression and reduced expression in siIκBα for many ERGs in subcluster 2.

Since there were genes which showed a good fit with multiple mathematical models, the best-fit model for each gene (Figure 26a) was identified. For each, the total nRMSD in replicate 1, nRMSD of siIκBα in replicate 1, nRMSD in replicate 2, and nRMSD of siIκBα in replicate 2 for each model, which showed a good fit was calculated. The total nRMSD was then compared between the good fit models, and the model with the smallest total nRMSD was identified. This model was defined as the "best-fit" model for each good fit gene. The best-fit model of many ERGs were found to be model v4 (Figure 26b and 26c), showing a transient expression pattern. Interestingly, among the ERGs recapitulated with model v4, there were well-known NFκB pathway regulators[66,67] (e.g., A20) and transcription factors (e.g., JUNB and KLF10), which are key inflammation and breast cancer regulators[57,65,74]. For the IRGs, *BCL2L11* encoded protein,

known as a tumor suppressor[64], was recapitulated by the 3-state cycle model, showing a monotonically increasing expression pattern. Among the DRGs, the *LTB* encoded membrane protein, known as tumor necrosis factor C, which promotes inflammation through the activation of the NFκB signaling pathway[58], and the *RELB*, known to be involved in immune tolerance to inflammation and to repress pro-inflammatory genes[59] were recapitulated by the simple model, showing a monotonically increasing expression pattern.

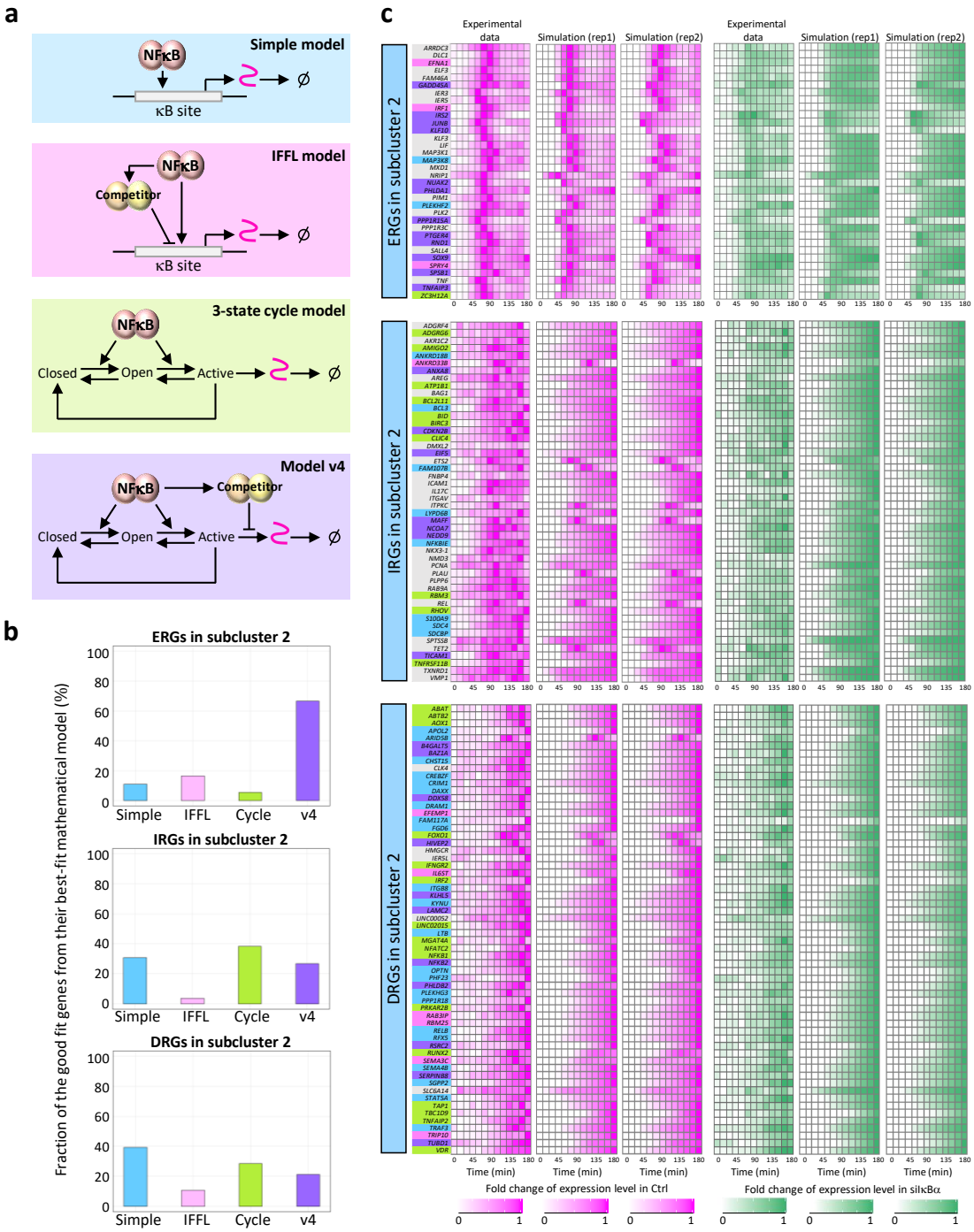

Figure 26. Model v4 recapitulated fold change in expression of many early response genes in subcluster 2

(a) Schematic of the 4 mathematical models. The color code corresponds with the background color of each model. (b) Fraction of the good fit genes from their best-fit mathematical model. (c) Heatmaps of the time course gene expression from experimental results and data-fit from the best-fit model. Each color bar indicates the best-fit model (blue: simple model, magenta: IFFL model, green: 3-state cycle model, and purple: model v4), which shows the smallest total nRMSD. Grey colored bars indicate genes which didn't a good fit with any of the 4 mathematical models, and so the result from the simple model are shown.

5.7 Chromatin remodeling at κB sites in promoter regions of post-induction repressed genes

To confirm that transcription of post-induction repressed ERGs in subcluster 2 that were best demonstrated by the 3-state cycle model or model v4 are regulated by chromatin remodeling, the time course chromatin accessibility at the κB sites in the promoter regions of these genes were investigated using aggregated single-cell ATAC-seq data. Firstly, κB site enriched ATAC-seq peak regions at each time point in Ctrl and siIκBα for each subcluster 2 were identified. All 3 subclusters showed more κB site enriched peak regions in siIκBα than in Ctrl (Figure 27).

Motif analysis results at ATAC-seq peaks in promoter regions in Ctrl (focused on κB motifs)

	ERGs in subcluster 2			IRGs in subcluster 2			DRGs in subcluster 2		
	P-value	Targets %	Motif	P-value	Targets %	Motif	P-value	Targets %	Motif
0 min									
30 min	1e-3	7.69 %	REL	1e-3	5.26 %	RELB			
75 min									
120 min	1e-4	38.10 %	RELB				1e-6	20.59 %	NFκB-p65-Rel

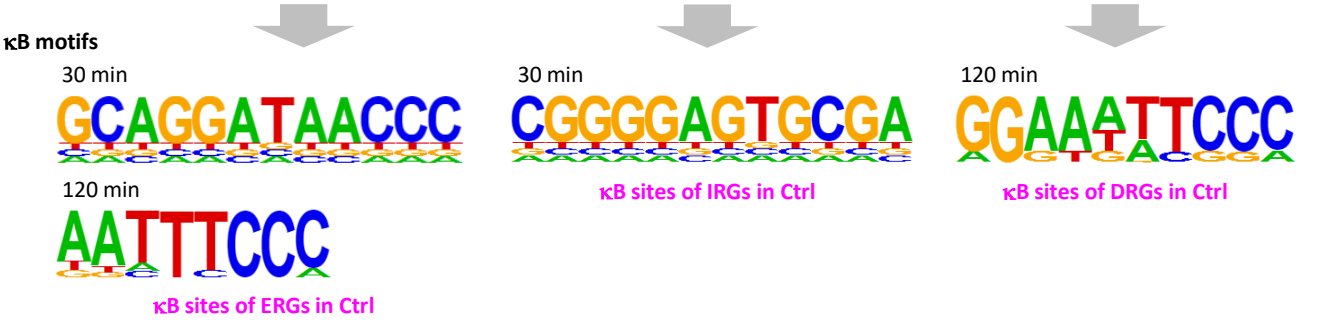

Motif analysis results at ATAC-seq peaks in promoter regions in siIκBα (focused on κB motifs)

	ERGs in subcluster 2			IRGs in subcluster 2			DRGs in subcluster 2		
	P-value	Targets %	Motif	P-value	Targets %	Motif	P-value	Targets %	Motif
0 min	1e-6	38.89 %	RELB	1e-4	13.64 %	RELB			
30 min	1e-8	35.71 %	RELB	1e-10	31.82 %	RELB			
75 min	1e-7	23.53 %	REL	1e-8	33.33 %	REL	1e-7	14.71 %	RELB
120 min	1e-7	19.23 %	NFκB-p50, p52				1e-5	41.67 %	REL

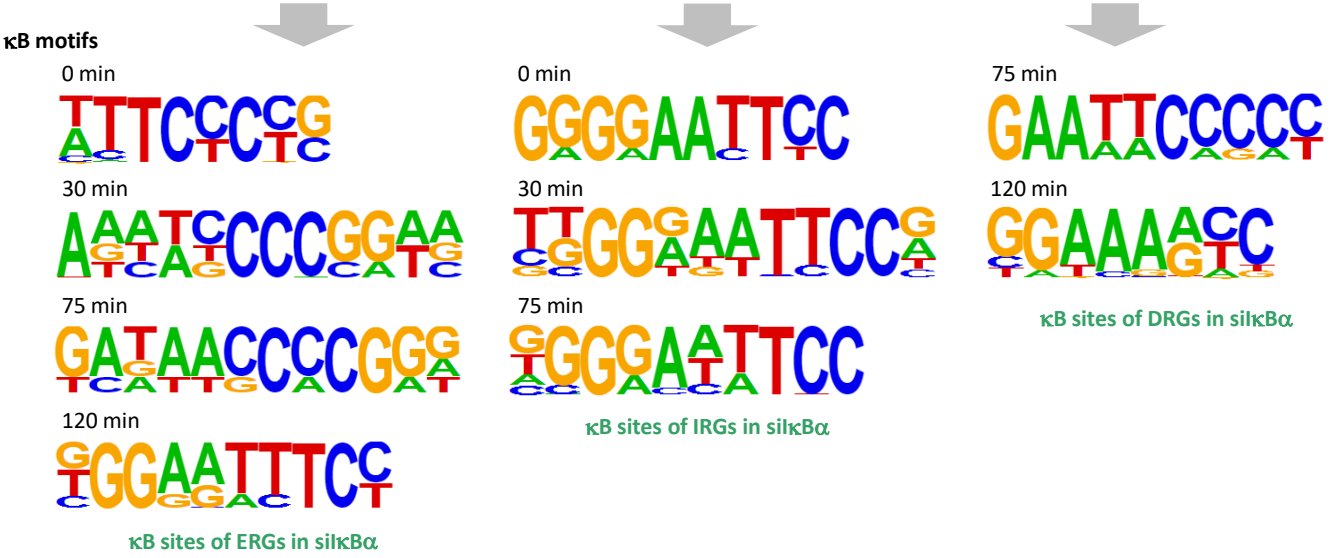

Figure 27. κB site enriched ATAC-seq peaks in promoter regions of ERGs, IRGs and DRGs in subcluster 2

κB site enriched aggregated single-cell ATAC-seq peak regions in promoter regions of ERGs, IRGs and DRGs in subcluster 2 were identified in Ctrl (Control) and siIκBα (IκBα knockdown). For κB site enriched peak regions at each time point, κB site detected regions were extracted and merged for multiple time points.

However, none of these κB-site-enriched peak regions were included in the κB-site-enriched peak regions identified in Figure 13b and 14a. This was because only the significantly induced peak regions after stimulation were extracted in Figure 13b and 14a, whereas most of the peak regions were not significantly induced but were induced to some extent during the time course. Thus, from these κB-site-enriched peak regions in promoter regions of genes in subcluster 2, only the κB-site-containing regions at each time point were further extracted, these regions were merged for multiple time points. The time course expression of genes in subcluster 2 showed their peak at 75 minutes for ERGs, 75 minutes and 120 minutes for IRGs and DRGs (Figure 28). Therefore, κB sites in promoter regions of these genes were expected to show a start of decrease in chromatin accessibility at least at 30 minutes or 75 minutes in both Ctrl and siIκBα.

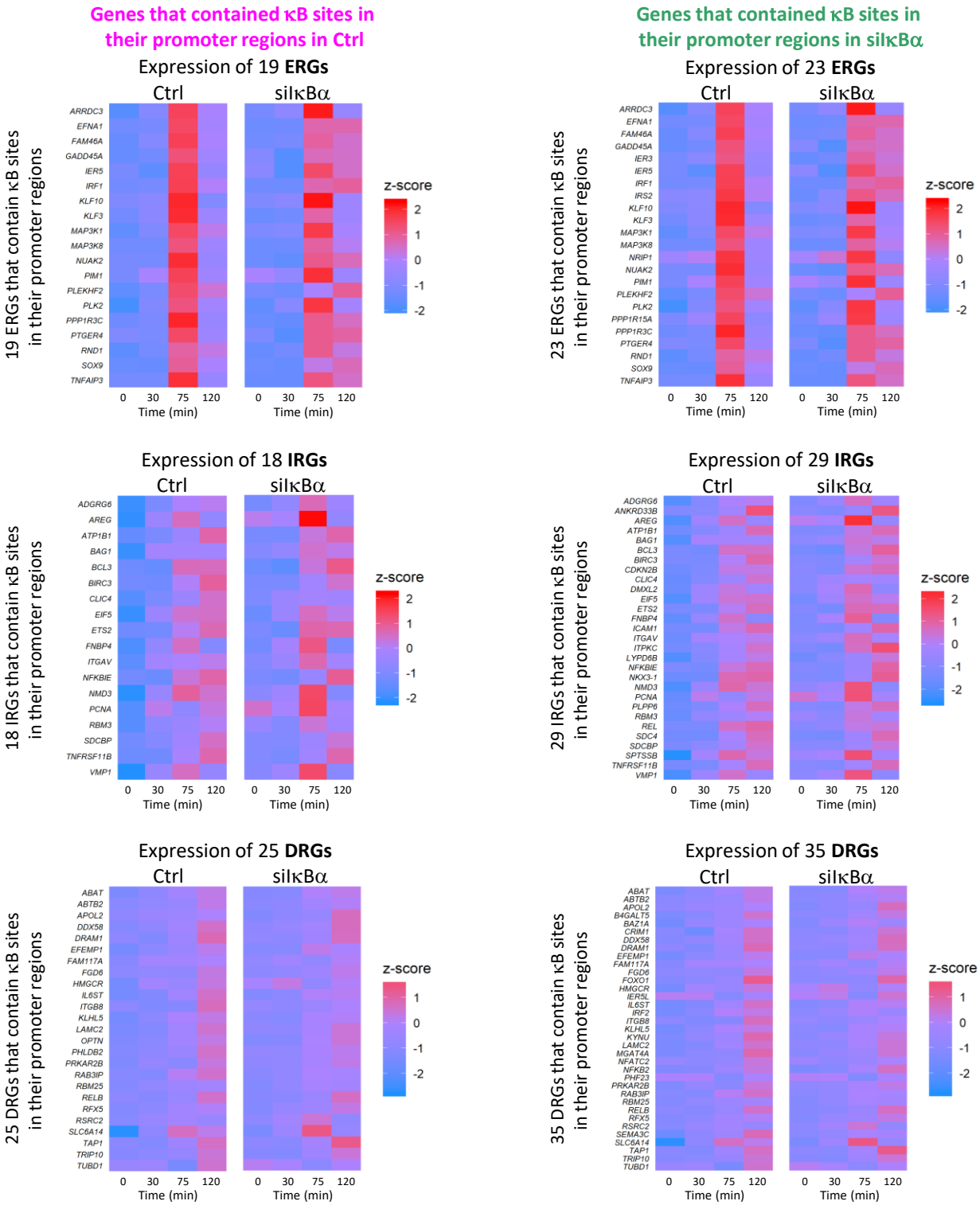

Figure 28. Expression of ERGs, IRGs and DRGs in subcluster 2 that contained κB sites in their promoter regions

Z-score normalized time course fold change in expression of ERGs, IRGs and DRGs in subcluster 2 which contained κB site detected aggregated single-cell ATAC-seq peak regions in promoter regions (± 500 bps TSS).

κB site detected regions that showed these patterns were identified, and more than 50 % of the post-induction repressed ERGs in subcluster 2 that were demonstrated by 3-state cycle model or model v4 (6 out of 11 genes) were found to show a decrease in chromatin accessibility before or at the same time (75 minutes) when post-induction repression was observed (Figure 29a and 29b). These included the *KLF10*, which is a key inflammation-related transcription factor that is an apoptosis-inducing tumor suppressor[74]. In contrast, less than 50 % of the ERGs, IRGs and DRGs in subcluster 2 demonstrated by any of the 4 models (41 out of 89 genes) that did not show post-induction repression showed these patterns (Figure 29b). These results suggest that many post-induction repressed ERGs in subcluster 2 showed chromatin remodeling at their promoter regions while many others did not, and these findings are consistent with the results obtained from mathematical modeling, showing that the transcriptional regulation of these post-induction repressed genes were best demonstrated by the GRMs which include chromatin remodeling modules.

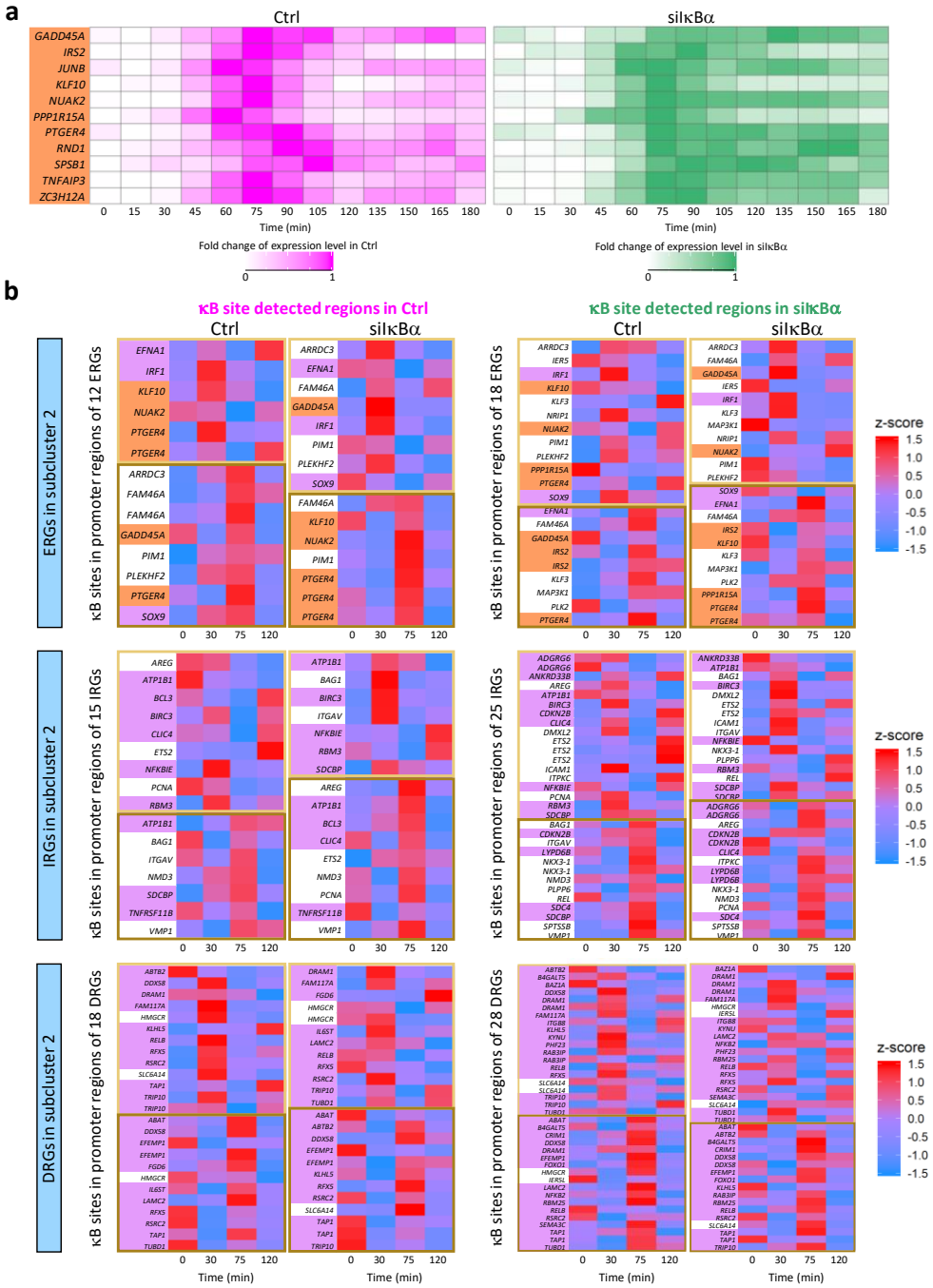

Figure 29. Chromatin remodeling observed for many post-induction repressed ERGs in subcluster 2

(a) Heatmaps of time course fold change in expression from data of all post-induction repressed genes that were demonstrated by the 3-state cycle model or model v4 (highlighted in orange). (b) Heatmaps of time course chromatin accessibility at κB sites in promoter regions of ERGs, IRGs and DRGs in subcluster 2 which showed the start of decrease in chromatin accessibility at least at 30 minutes or 75 minutes in both Ctrl and siIκBα. Genes highlighted with orange are post-induction repressed ERGs in subcluster 2 that were best demonstrated by 3-state cycle model or model v4. Genes highlighted with purple are genes that were demonstrated by any of the 4 models but did not show post-induction repression in data.

5.8 NFκB activation in COVID-19 patients at convalescent stages

5.8.1 NFκB binding sites of cytokine genes highly accessible in convalescent stages of severe patients

To investigate the chromatin landscapes at promoter regions of cytokine genes in *CCL3* highly expressed CD14+ monocytes, a previously published single-cell ATAC-seq data[50] from PBMCs collected from 6 healthy controls, 5 moderate COVID-19 patients in convalescent stages, and 3 severe COVID-19 patients in convalescent stages was analyzed. Firstly, to extract *CCL3* highly accessible CD14+ monocytes, dimensionality reduction and batch effect correction were performed. Then, cells which showed a high chromatin accessibility of *CD14*, *FCGR3A* and *CEBPB* which are canonical marker genes[50] of monocytes were overlaid on UMAP embedding. In addition, chromatin accessibility of *CCL3* were overlaid on UMAP embedding to identify cells with high chromatin accessibility of *CCL3*. Cells which showed high chromatin accessibility of *CCL3* also showed a high chromatin accessibility of *CD14* and *CEBPB* (Figure 30a). *CEBPB* is known to be highly expressed in CD14+ monocytes[75]. After performing clustering using the SLM algorithm, 7 clusters of cells were identified and cluster 1 was annotated as *CCL3* highly accessible CD14+ monocytes, which included 400 cells (Figure 30b).

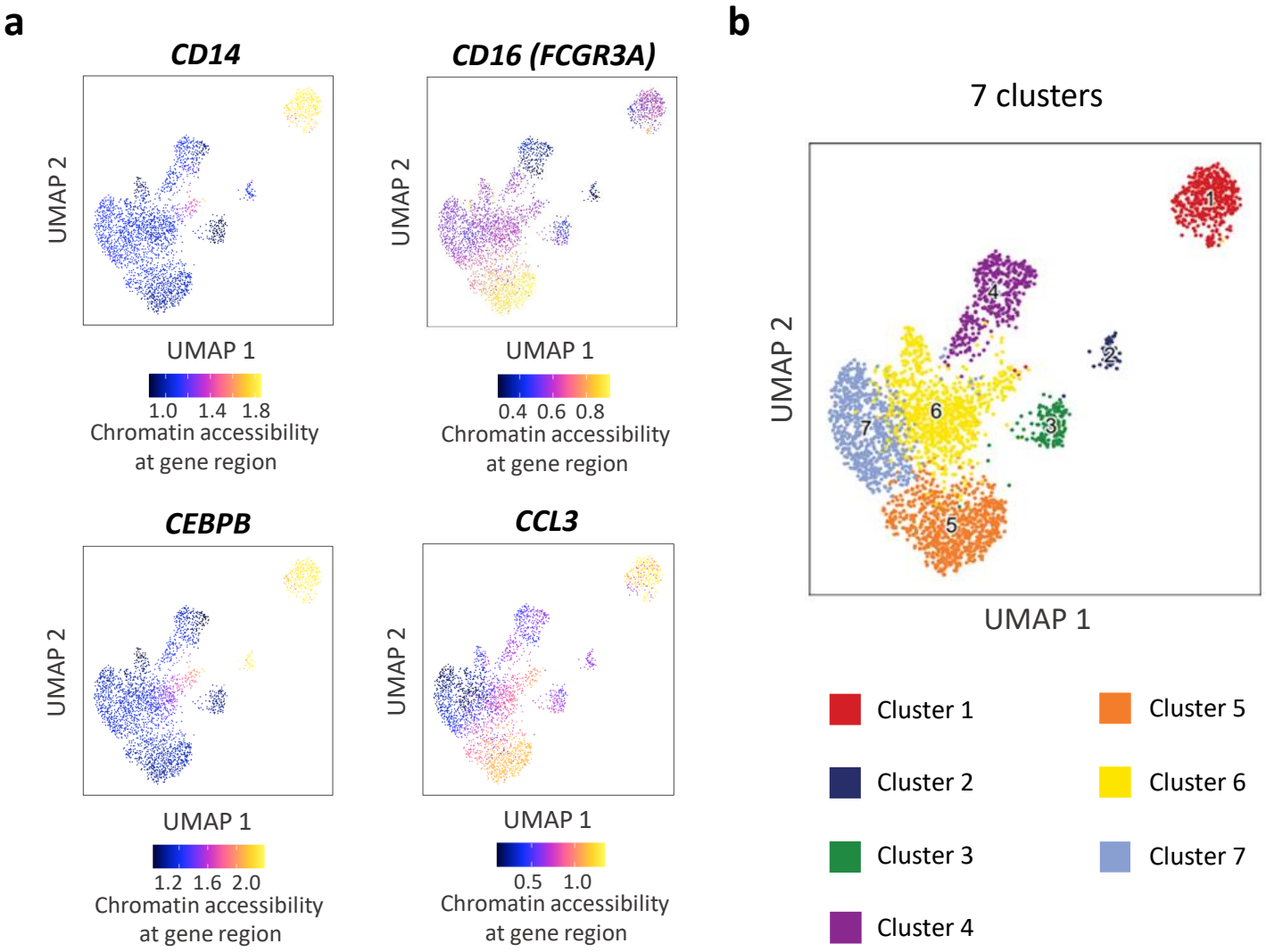

Figure 30. Identification of *CCL3* highly accessible CD14+ monocytes

(a) Chromatin accessibility at gene regions of canonical marker genes of monocytes overlaid on UMAP embedding.

(b) Clustering results of 400 cells of *CCL3* highly accessible CD14+ monocytes.

Using these cells for downstream analysis, the chromatin accessibility between healthy controls, moderate patients and severe patients in convalescent stages were statistically compared for 136 cytokine genes based on previous literature[34]. Among these genes, 28 showed a significant increase in chromatin accessibility between healthy controls and severe patients in convalescent stages. Furthermore, 14 of these genes were known NFκB target genes (Figure 31a). To investigate whether the significantly accessible chromatin regions in promoters (-5kb TSS) of 28 genes show enrichment of κB sites, motif analysis was performed at the peak regions in promoters of genes that are not NFκB target genes and NFκB target genes. As a result, while enriched motifs at peak regions in promoters of genes that are not NFκB target genes did not show enrichment of κB sites, enriched motifs at peak regions in promoters of NFκB target genes were enriched with κB sites (Figure 31b). To confirm whether peak regions of NFκB target genes show a significant enrichment of κB sites compared to peak regions of genes that were not NFκB target genes, motif analysis was performed for peak regions of NFκB target genes using the peak regions of genes that were not NFκB target genes as the background, and confirmed that the κB motif was highly enriched only in peak regions of NFκB target genes (Figure 31b).

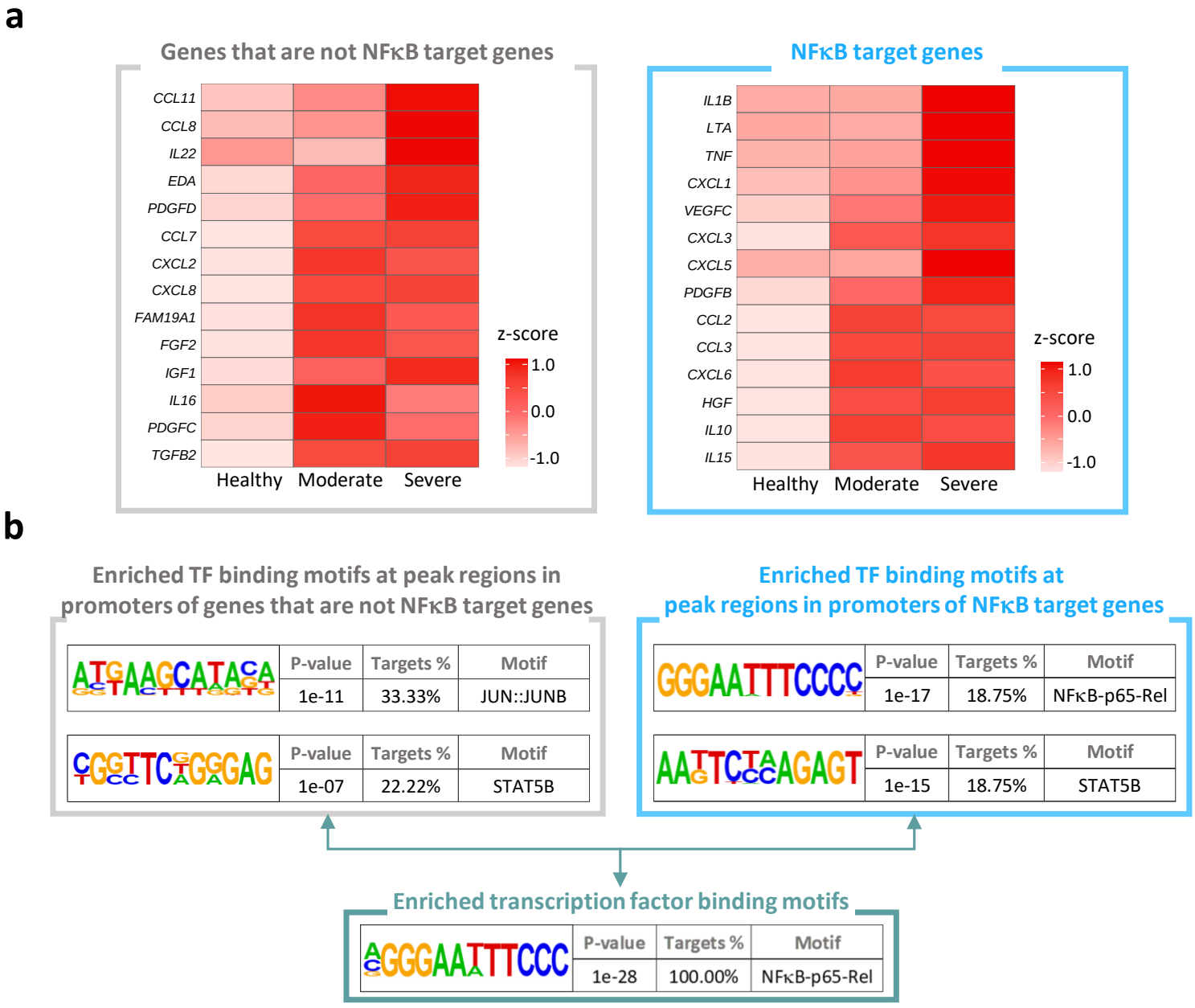

Figure 31. Significantly accessible chromatin regions of NFκB target cytokine genes

(a) Heatmaps of mean chromatin accessibility of single cells in each group (healthy control, moderate and severe in convalescent stages) which showed a significant increase in chromatin accessibility at gene regions of 28 cytokine genes (Wilcoxon rank sum test: $p < 0.05$). (b) Motif analysis results at peak regions in promoters of 28 cytokine genes. The results in light gray box and light blue box show representative transcription factor (TF) binding motifs. The result in the cadet blue square shows that NFκB binding motif was most enriched for peak regions in promoters of NFκB target genes using the peak regions in promoters of genes that were not NFκB target genes as the background.

5.8.2 Expression levels associated with chromatin accessibility of NFκB target cytokine genes

As the chromatin accessibility at gene regions of 28 cytokine genes showed a significant increase in convalescent stages of severe patients compared to healthy controls, whether expression levels of these 28 cytokine genes also show a significant increase in convalescent stages of severe patients was investigated using a previously published single-cell RNA-seq data[34] from *CCL3* highly expressed CD14+ monocytes in PBMCs collected from 25 healthy controls, 71 moderate COVID-19 patients in convalescent stages, and 80 severe COVID-19 patients in convalescent stages. Using this processed single-cell RNA-seq data, the expression levels of 28 cytokine genes were statistically compared between healthy controls, moderate and severe patients in convalescent stages. Among these genes, 5 genes that are not NFκB target genes and 7 NFκB target genes showed a significant increase in expression levels in convalescent stages of severe patients compared to healthy controls (Figure 32a). To validate whether the expression levels and chromatin accessibility of these genes show correlation, Pearson correlation coefficient was between the mean expression levels and mean chromatin accessibility of all genes in all groups (healthy controls, moderate and severe patients in convalescent stages). As a result, the correlation coefficient showed a strong positive correlation between expression levels and chromatin accessibility of these 12 cytokine genes (Figure 32b). This result indicates that more than 50% of the cytokine genes that showed an increase in both chromatin accessibility and expression levels in convalescent stages of severe patients were possibly regulated by NFκB.

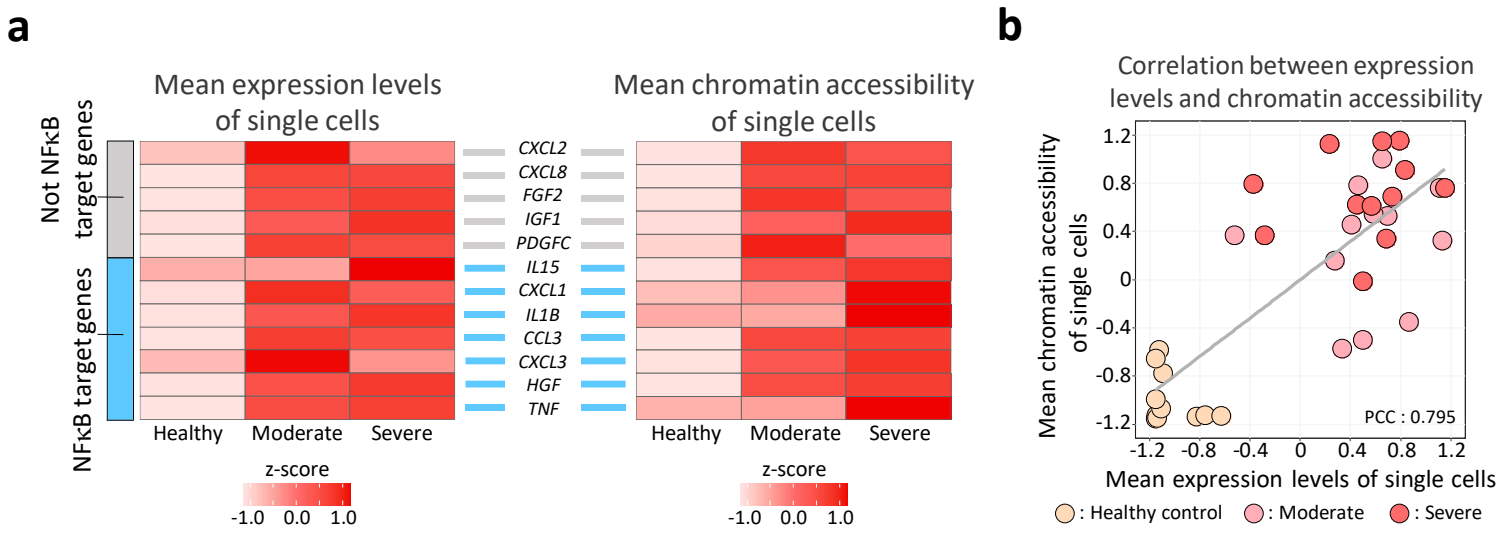

Figure 32. Correlation between expression levels and chromatin accessibility

(a) Heatmaps of mean expression levels and mean chromatin accessibility of single cells which showed a statistical significance (Wilcoxon rank sum test: $p < 0.05$) between healthy controls and severe patients in convalescent stages for single-cell expression levels and single-cell chromatin accessibility at gene regions of 5 genes that are not NFκB target genes and 7 NFκB target genes. (b) Correlation between the mean expression levels and mean chromatin accessibility at gene regions of single cells for 12 genes from (a) in all groups (healthy controls, moderate and severe patients in convalescent stages). Pearson correlation coefficient (PCC) shown at the corner of the graph.

6 Discussion

Previous studies have focused on IκBα's role as the negative feedback regulator of NFκB activity, which limits the duration when stimulated transiently[4,25]. Thus, in IκBα-deficient cells, transient stimulation results in prolonged NFκB activation[4,25], which in turn induces enhanced expression of some genes[4]. It was shown that prolonged NFκB activity allows genes regulated by a slow chromatin step or by slow mRNA decay to be activated more fully[23]. Persistent stimulation may result in NFκB oscillations mediated by the IκBα feedback loop; in their absence NFκB was shown in macrophages to generate hundreds of *de novo* enhancers by triggering nucleosome eviction[24], suggesting that IκBα's role is to preserve the enhancer landscape. However, the absence of IκBα also results in slowed and diminished activation of NFκB, as other IκB family members have slower IKK-responsive degradation kinetics[20]. Whether IκBα's role to provide rapid NFκB activation is important for gene activation has not been examined.

Physiologically, radiation is known to induce apoptosis[76] through the expression of TNF[77], which is also known to inhibit cell proliferation[78]. TNF activates the canonical NFκB signaling pathway, which induces IκBα degradation and releases NFκB to the nucleus for transcriptional regulation[1]. The expression of a gene that is involved in immune tolerance to inflammation[59] (e.g., *RELB*) and apoptosis-inducing tumor suppressor genes[64,74] (e.g., *BCL2L11* and *KLF10*) were confirmed. However, the expression of inflammation and cancer progressing genes[57,58,65–67] (e.g., *A20*, *JUNB* and *LTB*) were also observed when IκBα was present, indicating that IκBα enables the full induction of not only NFκB-regulated genes that promote apoptosis, but also NFκB-regulated genes that promote inflammation and cancer progression. Here, these findings

provided by studying gene expression in cells that contain IκBα and those that do not suggest that IκBα not only functions as a negative feedback regulator, but also as an enabler of some NFκB-regulated stimulus-responsive inflammatory gene expression and NFκB-regulated early chromatin activation. This indicates the complex involvement of IκBα in NFκB transcription regulation, activated by TNF.

Secondly, how the altered dynamics in IκBα deficient cells are interpreted by transcription regulatory mechanisms of TNF-induced NFκB target genes was explored. In particular, expression of some early response genes was repressed in the absence of IκBα after induction. Given that the time course of nuclear NFκB activity in the absence of IκBα was prolonged, these results indicated the existence of gene regulatory mechanisms. These mechanisms were investigated by fitting GRM models to the RNA-seq transcriptomic profiling data.

While the NFκB activation mechanism is common between cells, basal nuclear NFκB activity varies from cell to cell because of heterogeneity in protein expression[79,80] and kinase activity. A previous study revealed that fold-change of NFκB activity rather than absolute NFκB abundance in HeLa cells provided a more statistically robust explanation for the observed variability in expression between cells[46]. The fold-change detection mechanism provides an analog of Weber's law, which discriminates the signal relative to the background signal[81]. Mathematically, it can be seen through dimensional analysis. The dynamic equations for Y and Z can be rescaled so that stimulation X drops out, and only the fold-change in input level, $F(t)=X(t) / X_0$ drives the dynamics of Z (Figure 33)[54].

Dynamic equations for the IFFL

Both X and Y regulate the Z promoter, generally described by an input function:

$$G(X,Y) = \beta_0 \frac{X/K_1}{1 + X/K_1 + Y/K_2 + XY/K_3} \ldots (1)$$

When repression by Y is strong,

$$Y/K_2 >> (1 + X/K_1 + XY/K_3)$$

it can be written to a first approximation:

$$G(X,Y) = \frac{\beta_2 X}{Y} \ldots (2)$$

Where $\beta_2 = \beta_0 K_2/K_1$. The resulting dynamic equations for Y and Z are:

$$\frac{dY}{dt} = \beta_1 X - \alpha_1 Y \ldots (3)$$

$$\frac{dZ}{dt} = \frac{\beta_2 X}{Y} - \alpha_2 Z \ldots (4)$$

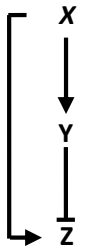

Dimensional analysis shows that IFFL provides fold-change detection

Define the following dimensionless variables,

$$y = \frac{Y}{\beta_1 X_0/\alpha_1} \qquad z = \frac{Z}{\beta_2 \alpha_1/\beta_1 \alpha_2} \ldots (5)$$

$$F = \frac{X}{X_0} \qquad \tau = \alpha_1 t \ldots (6)$$

and rescale equations 3-4,

$$\frac{dy}{d\tau} = F - y \ldots (7) \qquad r\frac{dz}{d\tau} = \frac{F}{y} - z \ldots (8)$$

This scaling shows that the dynamics of the IFFL depends on only one parameter,

$$r = \frac{1/\alpha_2}{1/\alpha_1} \qquad \frac{\text{half-life of Z}}{\text{half-life of Y}} \ldots (9)$$

Thus, dynamics of Z (eqn. 8) depends on fold-changes in X (F), and not on the absolute level of X: a feature called fold change detection.

Figure 33. Fold change detection in the IFFL (incoherent feedforward loop)
Mathematical description of the IFFL as a fold-change detector[54].

In signaling systems, it may be mediated by an IFFL, in which a transcription factor regulates its target gene and a repressor of the target gene. Since the fold change detection mechanism in the transcription of target genes is introduced by an incoherent feedforward loop of human cells[82–84] and is also found in the NFκB signaling pathway, the IFFL model was applied. Consequently, a combined model that inserts the IFFL model into the 3-state cycle model was found to recapitulate many early response genes, indicating that transcription is regulated by a post-induction repression mechanism that drives the promoter state from active to closed and a detectable fold change mechanism that renders these genes sensitive to the presence of IκBα. As a whole, the complexity of the transcription regulatory mechanism increased as the response time to TNF stimulation decreased, indicating that inflammation and cancer-related early response genes require a strict and precise transcriptional regulation to avoid overproduction (Figure 34).

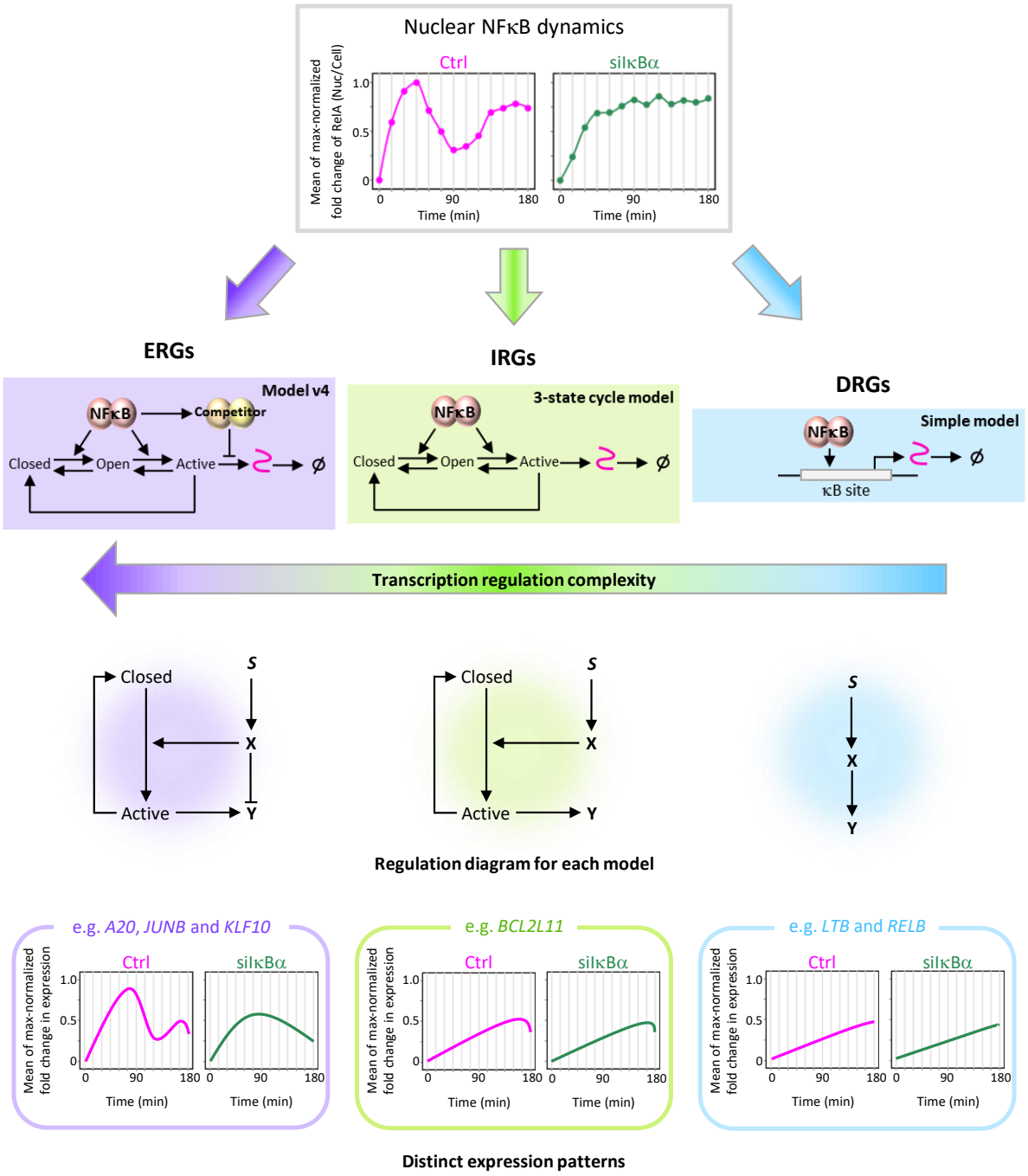

Figure 34. Distinct regulatory mechanisms of NFκB target genes depending on their response time
Diagram of the distinct transcription regulatory mechanisms that characterize each TNF-induced NFκB target gene cluster. Mean fold change in nuclear NFκB abundance of two biological replicates in Ctrl and siIκBα were interpolated to every second (same method used in mathematical modeling) and were max-normalized from 0 to 1 together, shown as line graphs in the top panel. The dots indicate the data from fixed-cell immunofluorescence experiments. The bottom panel shows the schematic curves of the expression patterns of ERGs, IRGs and DRGs in subcluster 2.

The post-induction repression can be explained by molecular mechanisms that involve chromatin remodeling complexes that have been revealed in previous studies[85,86]. For example, the nucleosome remodeling and deacetylation (NuRD) complex is recruited to its target sites by transcriptional repressors and/or methylated DNA, and nucleosome remodeling facilitates histone deacetylation by HDAC1/2 subunits of the NuRD complex[85]. This enzymatic reaction promotes the folding of chromatin into a repressed, higher-order structure, which in turn leads to the loss of RNA polymerase II and represses transcription of some genes[85]. At the same time, resetting the local nucleosome landscape and initializing the transcription start site of RNA polymerase II established a new transcriptional state, where some genes showed an overall increase in transcript levels[87]. In addition, NuRD complex is known to promote the activity of an another chromatin remodeling complex called the polycomb repressive complex 2 (PRC2)[88,89], which initially targets the genomic region for chromatin remodeling by methylating H3K27. H3K27me3 produced by PRC2 acts as a docking site for the PRC1 to induce chromatin compaction, which reduces not only the accessibility of transcription factors[86] but also the ATP-dependent chromatin-remodeling machineries, such as the SWI/SNF complex[90]. The SWI/SNF complex also catalyzes ATP-dependent chromatin remodeling by coupling ATP-hydrolysis with directional movement over DNA, which represses transcription of some genes[91]. Chromatin remodeling mechanisms including these mechanisms may cooperatively or independently induce the post-induction repression observed for many early response genes found in this study.

This study provides insights that may be used to reveal the transcription regulatory mechanisms in many biological systems, such as systems that require both post-induction repression and fold change detection. TNF-induced NFκB target genes

that were recapitulated by either of the four models are likely robust to noise, because the models applied here were all deterministic. In addition, genes that did not show a good fit when either of the four models were applied may be regulated by an additional combination of a transcription regulatory model, such as the existence of multiple repressors and activators[92–95]. Other factors may also affect the transcription of target genes. For example, the dose of the TNF stimulus changes the NFκB dynamics, which in turn alters the transcription pattern of the target gene[96], or the abundance of the different NFκB dimers affects the transcription state of the target gene[97]. Transcription regulation is affected by various factors and is controlled by a sensitive balance in each cell.

In summary, rapid IκBα-mediated NFκB activation was found to be required for full induction of some NFκB-regulated target genes and for NFκB-regulated early chromatin activation. Among the TNF-induced target genes which showed reduced fold change in expression in the absence of IκBα, gene regulatory mechanisms that render some genes sensitive to the presence of IκBα were characterized by fitting GRM models to data. This study repositions the function of IκBα not only as a negative feedback regulator but also as an enabler of NFκB-regulated stimulus-responsive inflammatory gene expression in the signaling pathway, and proposes gene regulatory mechanisms that safeguard inflammatory gene expression from overproduction.

These findings implicated that gene regulatory mechanisms of inflammatory NFκB target genes identified here are important for preventing overproduction of inflammatory NFκB target genes which may lead to harmful diseases in MCF-7 cells, but this may also apply for other cell types. In particular, patients suffering from post-acute COVID-19 syndrome are known to be affected by the residual effects of SARS-CoV-2

infection, and an overproduction of inflammatory cytokines during a robust innate immune response are considered as one of the causes of post-acute COVID-19 syndrome[26]. For example, in thromboembolism, cytokines appear to promote thrombus formation[98]. However, whether transcription regulatory regions of NFκB target cytokine genes are active with their expression overproduced in a subtype of cells which was considered to be the major source of cytokine storm from COVID-19 patients in convalescent stages remained to be elucidated. To reveal this, published datasets were used for investigation[34,50]. Significantly accessible peak regions included in promoters of NFκB target cytokine genes which showed a significantly high chromatin accessibility in convalescent stages of severe COVID-19 patients were enriched with κB sites, indicating the possibility of transcriptional regulation by NFκB in convalescent stages. Therefore, when combined with gene expression analysis, cytokine genes were identified which were significantly high for their chromatin accessibility and expression levels in convalescent stages of severe COVID-19 patients, and more than 50 % of these genes were NFκB target cytokine genes. These genes included *TNF* and *IL1B*, which encode well-known cytokines that promote inflammation through the NFκB signaling pathway, p38 MAPK signaling pathway and the JNK signaling pathway[23,99–101]. Fatigue and cognitive disturbances have been reported to be induced by TNF and IL-1β[102]. TNF is also considered to contribute to venous thromboembolism (VTE) pathogenesis[103], and IL-1β level have showed association with sleep disturbance[104]. It was found that these symptoms which are also known as the sequelae of post-acute COVID-19[26] may be induced by the overproduction of these NFκB regulated cytokine genes with highly accessible NFκB binding sites in their promoters in convalescent stages of COVID-19 patients. Thus, the precise transcriptional regulation of NFκB target inflammatory genes

was confirmed to be crucial to maintain health, and overproduction of these genes without precise regulation in this subtype of cells may lead to various diseases, including post-acute COVID-19 syndrome. These findings may contribute when therapeutically modulating aberrant expression of inflammatory cytokine genes from patients with post-acute COVID-19 syndrome.

7 References

1. Hoffmann, A. & Baltimore, D. Circuitry of nuclear factor κB signaling. *Immunol. Rev.* **210**, 171–186 (2006).
2. Lee, S. H. & Hannink, M. Characterization of the nuclear import and export functions of IκBε. *J. Biol. Chem.* **277**, 23358–23366 (2002).
3. Tam, W. F., Lee, L. H., Davis, L. & Sen, R. Cytoplasmic Sequestration of Rel Proteins by IκBα Requires CRM1-Dependent Nuclear Export. *Mol. Cell. Biol.* **20**, 2269–2284 (2000).
4. Hoffmann, A., Levchenko, A., Scott, M. L. & Baltimore, D. The IκB-NF-κB signaling module: Temporal control and selective gene activation. *Science (80-.).* **298**, 1241–1245 (2002).
5. Gilmore, T. D. Introduction to NF-κB: Players, pathways, perspectives. *Oncogene* **25**, 6680–6684 (2006).
6. Basak, S., Shih, V. F.-S. & Hoffmann, A. Generation and Activation of Multiple Dimeric Transcription Factors within the NF-κB Signaling System. *Mol. Cell. Biol.* **28**, 3139–3150 (2008).
7. Bours, V. *et al.* The oncoprotein Bcl-3 directly transactivates through κB motifs via association with DNA-binding p50B homodimers. *Cell* (1993) doi:10.1016/0092-8674(93)90401-B.
8. Claudio, E., Brown, K. & Siebenlist, U. NF-κB guides the survival and differentiation of developing lymphocytes. *Cell Death Differ.* **13**, 697–701 (2006).
9. Dejardin, E. *et al.* The Lymphotoxin-Receptor Induces Different Patterns of Gene

Expression via Two NF-B Pathways quire LTR signaling for their expression in development (Ngo et al The NF-B family of transcription factors regulates expression of genes crucial to innate and ad. *Immunity* **17**, 525–535 (2002).

10. Hoffmann, A., Natoli, G. & Ghosh, G. Transcriptional regulation via the NF-κB signaling module. *Oncogene* **25**, 6706–6716 (2006).
11. Oeckinghaus, A. & Ghosh, S. The NF-kappaB family of transcription factors and its regulation. *Cold Spring Harbor perspectives in biology* (2009) doi:10.1101/cshperspect.a000034.
12. Sarnico, I. *et al.* Activation of NF-κB p65/c-Rel dimer is associated with neuroprotection elicited by mGlu5 receptor agonists against MPP+ toxicity in SK-N-SH cells. *J. Neural Transm.* **115**, 669–676 (2008).
13. Weih, D. S., Yilmaz, Z. B. & Weih, F. Essential Role of RelB in Germinal Center and Marginal Zone Formation and Proper Expression of Homing Chemokines. *J. Immunol.* **167**, 1909–1919 (2001).
14. Yilmaz, Z. B., Weih, D. S., Sivakumar, V. & Weih, F. RelB is required for Peyer's patch development: Differential regulation of p52-RelB by lymphotoxin and TNF. *EMBO J.* **22**, 121–130 (2003).
15. Werner, S. L. *et al.* Encoding NF-κB temporal control in response to TNF: Distinct roles for the negative regulators IκBα and A20. *Genes Dev.* **22**, 2093–2101 (2008).
16. Basak, S., Behar, M. & Hoffmann, A. Lessons from mathematically modeling the NF-κB pathway. *Immunol. Rev.* (2012) doi:10.1111/j.1600-065X.2011.01092.x.
17. O'Dea, E. & Hoffmann, A. NF-κ B signaling. *Wiley Interdiscip. Rev. Syst. Biol. Med.* (2009) doi:10.1002/wsbm.30.

18. Beg, A. A., Finco, T. S., Nantermet, P. V & Baldwin, A. S. Tumor necrosis factor and interleukin-1 lead to phosphorylation and loss of I kappa B alpha: a mechanism for NF-kappa B activation. *Mol. Cell. Biol.* **13**, 3301–3310 (1993).

19. Henkel, T. *et al.* Rapid proteolysis of IκB-α is necessary for activation of transcription factor NF-κB. *Nature* (1993) doi:10.1038/365182a0.

20. Kearns, J. D., Basak, S., Werner, S. L., Huang, C. S. & Hoffmann, A. IκBε provides negative feedback to control NF-κB oscillations, signaling dynamics, and inflammatory gene expression. *J. Cell Biol.* **173**, 659–664 (2006).

21. Dembinski, H. E. *et al.* Functional importance of stripping in NFκB signaling revealed by a stripping-impaired IκBα mutant. *Proc. Natl. Acad. Sci. U. S. A.* **114**, 1916–1921 (2017).

22. Mitchell, S., Vargas, J. & Hoffmann, A. Signaling via the NFκB system. *Wiley Interdisciplinary Reviews: Systems Biology and Medicine* (2016) doi:10.1002/wsbm.1331.

23. Sen, S., Cheng, Z., Sheu, K. M., Chen, Y. H. & Hoffmann, A. Gene Regulatory Strategies that Decode the Duration of NFκB Dynamics Contribute to LPS-versus TNF-Specific Gene Expression. *Cell Syst.* (2020) doi:10.1016/j.cels.2019.12.004.

24. Cheng, Q. J. *et al.* NF-κB dynamics determine the stimulus specificity of epigenomic reprogramming in macrophages. *Science (80-.).* (2021) doi:10.1126/science.abc0269.

25. Adelaja, A. *et al.* Six distinct NFκB signaling codons convey discrete information to distinguish stimuli and enable appropriate macrophage responses. *Immunity* (2021) doi:10.1016/j.immuni.2021.04.011.

26. Nalbandian, A. *et al.* Post-acute COVID-19 syndrome. *Nat. Med.* **27**, 601–615 (2021).

27. Carfi, A.; Bernabei, R. and Landi, F. Persistent Symptoms in Patients After Acute COVID-19. *JAMA* **324**, 603–605 (2020).

28. Tenforde, M. W. *et al.* Symptom Duration and Risk Factors for Delayed Return to Usual Health Among[1] M. W. Tenforde et al., "Symptom Duration and Risk Factors for Delayed Return to Usual Health Among Outpatients with COVID-19 in a Multistate Health Care Systems Network — United. *MMWR. Morb. Mortal. Wkly. Rep.* **69**, 993–998 (2020).

29. Ramanathan, K. *et al.* 6-month consequences of COVID-19 in patients discharged from hospital: a cohort study. *Lancet* **397**, 19–21 (2020).

30. McElvaney, O. J. *et al.* Characterization of the inflammatory response to severe COVID-19 Illness. *Am. J. Respir. Crit. Care Med.* **202**, 812–821 (2020).

31. Sungnak, W. *et al.* SARS-CoV-2 entry factors are highly expressed in nasal epithelial cells together with innate immune genes. *Nat. Med.* **26**, 681–687 (2020).

32. Tang, N., Li, D., Wang, X. & Sun, Z. Abnormal coagulation parameters are associated with poor prognosis in patients with novel coronavirus pneumonia. *J. Thromb. Haemost.* **18**, 844–847 (2020).

33. Hirano, T. & Murakami, M. COVID-19: A New Virus, but a Familiar Receptor and Cytokine Release Syndrome. *Immunity* **52**, 731–733 (2020).

34. Ren, X. *et al.* COVID-19 immune features revealed by a large-scale single-cell transcriptome atlas. *Cell* **184**, 1895-1913.e19 (2021).

35. Magi, S. *et al.* Transcriptionally inducible pleckstrin homology-like domain,

family a, member 1, attenuates ERBB receptor activity by inhibiting receptor oligomerization. *J. Biol. Chem.* (2018) doi:10.1074/jbc.M117.778399.

36. Buenrostro, J. D. *et al.* Single-cell chromatin accessibility reveals principles of regulatory variation. *Nature* **523**, 486–490 (2015).

37. Kim, D., Langmead, B. & Salzberg, S. L. Hisat2. *Nat. Methods* (2015).

38. Krueger, F. Trim Galore!: A wrapper tool around Cutadapt and FastQC to consistently apply quality and adapter trimming to FastQ files. *Babraham Inst.* (2015).

39. Liao, Y., Smyth, G. K. & Shi, W. FeatureCounts: An efficient general purpose program for assigning sequence reads to genomic features. *Bioinformatics* (2014) doi:10.1093/bioinformatics/btt656.

40. Robinson, M., Mccarthy, D. & Smyth, G. K. edgeR. *Most* (2010).

41. Love, M. I., Huber, W. & Anders, S. Moderated estimation of fold change and dispersion for RNA-seq data with DESeq2. *Genome Biol.* (2014) doi:10.1186/s13059-014-0550-8.

42. Benner, C., Heinz, S. & Glass, C. K. HOMER - Software for motif discovery and next generation sequencing analysis. *Http://Homer.Ucsd.Edu/* (2017).

43. Langmead, B., Trapnell, C., Pop, M. & Salzberg, S. L. Ultrafast and memory-efficient alignment of short DNA sequences to the human genome. *Genome Biol.* (2009) doi:10.1186/gb-2009-10-3-r25.

44. Li, H. *et al.* The Sequence Alignment/Map format and SAMtools. *Bioinformatics* (2009) doi:10.1093/bioinformatics/btp352.

45. Ramírez, F., Dündar, F., Diehl, S., Grüning, B. A. & Manke, T. DeepTools: A flexible platform for exploring deep-sequencing data. *Nucleic Acids Res.* (2014)

doi:10.1093/nar/gku365.

46. Lee, R. E. C., Walker, S. R., Savery, K., Frank, D. A. & Gaudet, S. Fold change of nuclear NF-κB determines TNF-induced transcription in single cells. *Mol. Cell* **53**, 867–879 (2014).

47. Cartwright, T., Perkins, N. D. & L Wilson, C. NFKB1: a suppressor of inflammation, ageing and cancer. *The FEBS journal* (2016) doi:10.1111/febs.13627.

48. Moorthy, A. K. *et al.* The 20S proteasome processes NF-κB1 p105 into p50 in a translation-independent manner. *EMBO J.* (2006) doi:10.1038/sj.emboj.7601081.

49. Grant, B. J., Rodrigues, A. P. C., ElSawy, K. M., McCammon, J. A. & Caves, L. S. D. Bio3d: An R package for the comparative analysis of protein structures. *Bioinformatics* (2006) doi:10.1093/bioinformatics/btl461.

50. You, M. *et al.* Single-cell epigenomic landscape of peripheral immune cells reveals establishment of trained immunity in individuals convalescing from COVID-19. *Nat. Cell Biol.* **23**, 620–630 (2021).

51. Granja, J. M. *et al.* Author Correction: ArchR is a scalable software package for integrative single-cell chromatin accessibility analysis (Nature Genetics, (2021), 53, 3, (403-411), 10.1038/s41588-021-00790-6). *Nat. Genet.* **53**, 935 (2021).

52. van Dijk, D. *et al.* Recovering Gene Interactions from Single-Cell Data Using Data Diffusion. *Cell* **174**, 716-729.e27 (2018).

53. Waltman, L. & Van Eck, N. J. A smart local moving algorithm for large-scale modularity-based community detection. *Eur. Phys. J. B* **86**, (2013).

54. Goentoro, L., Shoval, O., Kirschner, M. W. & Alon, U. The Incoherent Feedforward Loop Can Provide Fold-Change Detection in Gene Regulation. *Mol.*

Cell (2009) doi:10.1016/j.molcel.2009.11.018.

55. Fagerlund, R. *et al.* Anatomy of a negative feedback loop: The case of IκB. *J. R. Soc. Interface* (2015) doi:10.1098/rsif.2015.0262.

56. Nam, S. & Lim, J. S. Essential role of interferon regulatory factor 4 (IRF4) in immune cell development. *Archives of Pharmacal Research* (2016) doi:10.1007/s12272-016-0854-1.

57. Gomard, T. *et al.* An NF-κB-dependent role for JunB in the induction of proinflammatory cytokines in LPS-activated bone marrow-derived dendritic cells. *PLoS One* (2010) doi:10.1371/journal.pone.0009585.

58. Bauer, J. *et al.* Lymphotoxin, NF-κB, and cancer: The dark side of cytokines. *Dig. Dis.* (2012) doi:10.1159/000341690.

59. Baud, V. & Collares, D. Post-Translational Modifications of RelB NF-κB Subunit and Associated Functions. *Cells* (2016) doi:10.3390/cells5020022.

60. Alon, U. Network motifs: Theory and experimental approaches. *Nat. Rev. Genet.* **8**, 450–461 (2007).

61. Ma, H. W. *et al.* An extended transcriptional regulatory network of Escherichia coli and analysis of its hierarchical structure and network motifs. *Nucleic Acids Res.* **32**, 6643–6649 (2004).

62. Mangan, S. & Alon, U. Structure and function of the feed-forward loop network motif. *Proc. Natl. Acad. Sci. U. S. A.* **100**, 11980–11985 (2003).

63. Mangan, S., Itzkovitz, S., Zaslaver, A. & Alon, U. The incoherent feed-forward loop accelerates the response-time of the gal system of Escherichia coli. *J. Mol. Biol.* **356**, 1073–1081 (2006).

64. Tan, T. T. *et al.* Key roles of BIM-driven apoptosis in epithelial tumors and

rational chemotherapy. *Cancer Cell* (2005) doi:10.1016/j.ccr.2005.02.008.

65. Sundqvist, A. *et al.* JUNB governs a feed-forward network of TGFβ signaling that aggravates breast cancer invasion. *Nucleic Acids Res.* (2018) doi:10.1093/nar/gkx1190.

66. Lee, J. H. *et al.* A20 promotes metastasis of aggressive basal-like breast cancers through multi-monoubiquitylation of Snail1. *Nat. Cell Biol.* (2017) doi:10.1038/ncb3609.

67. Yoon, C. I. *et al.* High A20 expression negatively impacts survival in patients with breast cancer. *PLoS One* (2019) doi:10.1371/journal.pone.0221721.

68. Balkwill, F. TNF-α in promotion and progression of cancer. *Cancer and Metastasis Reviews* (2006) doi:10.1007/s10555-006-9005-3.

69. Van Antwerp, D. J., Martin, S. J., Kafri, T., Green, D. R. & Verma, I. M. Suppression of TNF-α-induced apoptosis by NF-κB. *Science (80-.).* (1996) doi:10.1126/science.274.5288.787.

70. Knüpfer, H. & Preiß, R. Significance of interleukin-6 (IL-6) in breast cancer (review). *Breast Cancer Research and Treatment* (2007) doi:10.1007/s10549-006-9328-3.

71. van Horssen, R., ten Hagen, T. L. M. & Eggermont, A. M. M. TNF-α in Cancer Treatment: Molecular Insights, Antitumor Effects, and Clinical Utility. *Oncologist* (2006) doi:10.1634/theoncologist.11-4-397.

72. Säemann, M. D. *et al.* Anti-inflammatory effects of sodium butyrate on human monocytes: potent inhibition of IL-12 and up-regulation of IL-10 production. *FASEB J.* (2000) doi:10.1096/fj.00-0359fje.

73. Yoshimoto, T. *et al.* Regulation of antitumor immune responses by the IL-12

family cytokines, IL-12, IL-23, and IL-27. *Clinical and Developmental Immunology* (2010) doi:10.1155/2010/832454.

74. Song, K. D., Kim, D. J., Lee, J. E., Yun, C. H. & Lee, W. K. KLF10, transforming growth factor-β-inducible early gene 1, acts as a tumor suppressor. *Biochem. Biophys. Res. Commun.* (2012) doi:10.1016/j.bbrc.2012.02.032.

75. Hume, D. A., Irvine, K. M. & Pridans, C. The Mononuclear Phagocyte System: The Relationship between Monocytes and Macrophages. *Trends Immunol.* **40**, 98–112 (2019).

76. Dewey, W. C., Ling, C. C. & Meyn, R. E. Radiation-induced apoptosis: Relevance to radiotherapy. *Int. J. Radiat. Oncol. Biol. Phys.* (1995) doi:10.1016/0360-3016(95)00214-8.

77. Rübe, C. E. *et al.* Modulation of radiation-induced tumour necrosis factor α (TNF-α) expression in the lung tissue by pentoxifylline. *Radiother. Oncol.* (2002) doi:10.1016/S0167-8140(02)00077-4.

78. Burow, M. E. *et al.* Differences in susceptibility to tumor necrosis factor α-induced apoptosis among MCF-7 breast cancer cell variants. *Cancer Res.* (1998).

79. Bar-Even, A. *et al.* Noise in protein expression scales with natural protein abundance. *Nat. Genet.* **38**, 636–643 (2006).

80. Cheong, R., Rhee, A., Wang, C. J., Nemenman, I. & Levchenko, A. Information transduction capacity of noisy biochemical signaling networks. *Science (80-.).* **334**, 354–358 (2011).

81. Ross, H.E., and Murray, D.J. E.H. Weber on the Tactile Senses (East Sussex, UK: Erlbaum Taylor & Francis) doi: https://doi.org/10.4324/9781315782089 (1996).

82. Boyer, L. A. *et al.* Core transcriptional regulatory circuitry in human embryonic stem cells. *Cell* **122**, 947–956 (2005).

83. Krejčí, A., Bernard, F., Housden, B., Collins, S. & Bray, S. J. Erratum: Direct response to notch activation: Signaling crosstalk and incoherent logic (Science Signaling (2009) 2 (er3)). *Sci. Signal.* **2**, 1–15 (2009).

84. Swiers, G., Patient, R. & Loose, M. Genetic regulatory networks programming hematopoietic stem cells and erythroid lineage specification. *Dev. Biol.* **294**, 525–540 (2006).

85. Tyler, J. K. & Kadonaga, J. T. The "Dark Side" of Chromatin Remodeling. *Cell* (1999) doi:10.1016/s0092-8674(00)81530-5.

86. Di Croce, L. & Helin, K. Transcriptional regulation by Polycomb group proteins. *Nature Structural and Molecular Biology* (2013) doi:10.1038/nsmb.2669.

87. Bornelöv, S. *et al.* The Nucleosome Remodeling and Deacetylation Complex Modulates Chromatin Structure at Sites of Active Transcription to Fine-Tune Gene Expression. *Mol. Cell* (2018) doi:10.1016/j.molcel.2018.06.003.

88. Morey, L. *et al.* MBD3, a Component of the NuRD Complex, Facilitates Chromatin Alteration and Deposition of Epigenetic Marks. *Mol. Cell. Biol.* (2008) doi:10.1128/mcb.00467-08.

89. Reynolds, N. *et al.* NuRD-mediated deacetylation of H3K27 facilitates recruitment of Polycomb Repressive Complex 2 to direct gene repression. *EMBO J.* (2012) doi:10.1038/emboj.2011.431.

90. Bantignies, F. & Cavalli, G. Polycomb group proteins: Repression in 3D. *Trends in Genetics* (2011) doi:10.1016/j.tig.2011.06.008.

91. Ribeiro-Silva, C., Vermeulen, W. & Lans, H. SWI/SNF: Complex complexes in genome stability and cancer. *DNA Repair* (2019) doi:10.1016/j.dnarep.2019.03.007.

92. Galardi, S., Mercatelli, N., Farace, M. G. & Ciafrè, S. A. NF-κkB and c-Jun induce the expression of the oncogenic miR-221 and miR-222 in prostate carcinoma and glioblastoma cells. *Nucleic Acids Res.* (2011) doi:10.1093/nar/gkr006.

93. Messner, B., Stütz, A. M., Albrecht, B., Peiritsch, S. & Woisetschläger, M. Cooperation of binding sites for STAT6 and NF kappa B/rel in the IL-4-induced up-regulation of the human IgE germline promoter. *J. Immunol.* (1997).

94. Planeta, C. S., Lepsch, L. B., Alves, R. & Scavone, C. Influence of the dopaminergic system, CREB, and transcription factor-κB on cocaine neurotoxicity. *Brazilian Journal of Medical and Biological Research* (2013) doi:10.1590/1414-431X20133379.

95. Toledano, M. B. & Leonard, W. J. Modulation of transcription factor NF-κB binding activity by oxidation-reduction in vitro. *Proc. Natl. Acad. Sci. U. S. A.* (1991) doi:10.1073/pnas.88.10.4328.

96. DeFelice, M. M. *et al.* NF-B signaling dynamics is controlled by a dose-sensing autoregulatory loop. *Sci. Signal.* (2019) doi:10.1126/scisignal.aau3568.

97. Lewin, S. R., Lambert, P., Deacon, N. J., Mills, J. & Crowe, S. M. Constitutive expression of p50 homodimer in freshly isolated human monocytes decreases with in vitro and in vivo differentiation: a possible mechanism influencing human immunodeficiency virus replication in monocytes and mature macrophages. *J. Virol.* (1997) doi:10.1128/jvi.71.3.2114-2119.1997.

98. Najem, M. Y., Couturaud, F. & Lemarié, C. A. Cytokine and chemokine regulation of venous thromboembolism. *J. Thromb. Haemost.* **18**, 1009–1019 (2020).

99. Beyaert, R. *et al.* The p38/RK mitogen-activated protein kinase pathway regulates interleukin-6 synthesis in response to tumour necrosis factor. *EMBO J.* **15**, 1914–1923 (1996).

100. Tomida, T., Takekawa, M. & Saito, H. Oscillation of p38 activity controls efficient pro-inflammatory gene expression. *Nat. Commun.* **6**, 4–6 (2015).

101. Wagner, E. F. & Nebreda, Á. R. Signal integration by JNK and p38 MAPK pathways in cancer development. *Nat. Rev. Cancer* **9**, 537–549 (2009).

102. Vaziri-harami, R. & Delkash, P. Can L -carnitine reduce post-COVID-19 fatigue ? *Ann. Med. Surg.* **73**, (2022).

103. Roselli, M. *et al.* TNF-α gene promoter polymorphisms and risk of venous thromboembolism in gastrointestinal cancer patients undergoing chemotherapy. *Ann. Oncol.* **24**, 2571–2575 (2013).

104. Breitbart, W. *et al.* Depression , cytokines , and pancreatic cancer. *Psychooncology.* **345**, 339–345 (2014).

8 Acknowledgements

This is a thesis to the Graduate School of Science, Osaka University for the doctoral degree. This study was done under the directions of Professor Mariko Okada at the Laboratory for Cell Systems, Institute for Protein Research, Osaka University.

I thank Dr. Alexander Hoffmann, Dr. Yutaka Suzuki, The University of Tokyo, and Dr. Takeya Kasukawa, RIKEN Institute for a help of next-generation sequence analysis and informatics analysis, respectively. I also thank Dr. Shigeyuki Magi for acquisition of the sequence data and data on the NF-κB dynamics used in this study. And lastly, I deeply appreciate the members in the Laboratory for Cell Systems for fruitful discussion and supporting this study.

9 Publication List

Ando, M., Magi, S., Seki, M., Suzuki, Y., Kasukawa, T., Lefaudeux, D., Hoffmann, A. and Okada, M. IκBα is required for full transcriptional induction of some NFκB-regulated genes in response to TNF in MCF-7 cells. *npj Syst Biol Appl* 7, 42 (2021). https://doi.org/10.1038/s41540-021-00204-7

Yoshida, K., Maekawa, T., Ly, N. H., Fujita, S., Muratani, M., Ando, M., Katou, Y., Araki, H., Miura, F., Shirahige, K., Okada, M., Ito, T., Chatton, B. and Ishii, S. ATF7-dependent epigenetic changes are required for the intergenerational effect of a paternal low-protein diet. *Molecular Cell* 78, 445-458 (2020). https://doi.org/10.1016/j.molcel.2020.02.028

Oral Presentation

Minami Ando, Kazunari Iwamoto, Shigeyuki Magi, Mariko Okada

Elucidating the transcriptional mechanisms of NF-κB target gene expression based on various sequence data

16th IPR Retreat Program, Osaka, Japan, 12-13 December, 2017.

Minami Ando, Kazunari Iwamoto, Shigeyuki Magi, Mariko Okada

Elucidating the transcriptional mechanisms of NF-κB target gene expression based on

various sequence data

Behavior and Logic of Cellular Systems X, Saitama, Japan, 12-13 April, 2018.

Minami Ando, Shigeyuki Magi, Kazunari Iwamoto, Mariko Okada

Elucidating the transcriptional mechanisms of NF-κB target gene expression based on various sequence data

The 56th Biophysical Society 2018, Okayama, Japan, 15-17 September, 2018.

Minami Ando, Shigeyuki Magi, Kazunari Iwamoto, Mariko Okada

Biological significance of the oscillatory dynamics of NF-κB for target gene expression

2018 International Symposium of Innovative Research and Graduate Education in Biomedical Sciences, Hsinchu, Taiwan, 25-29 September, 2018. (Best Presentation Award)

Minami Ando, Shigeyuki Magi, Kazunari Iwamoto, Mariko Okada

Biological significance of the oscillatory dynamics of NF-κB for target gene expression

The 91st Annual Meeting of the Japanese Biochemical Society, Kyoto, Japan, 24-26 September, 2018

Minami Ando, Shigeyuki Magi, Kazunari Iwamoto, Mariko Okada

Biological significance of the oscillatory dynamics of NF-κB for target gene expression

Japan-Korea Bilateral Symposium on Multi-Scale Structural Life Science and the Advanced Technologies, Osaka, Japan, 15 March, 2019.

Poster presentation

Minami Ando, Shigeyuki Magi, Kazunari Iwamoto, Mariko Okada

Biological significance of the oscillatory dynamics of NF-κB for target gene expression

17th IPR Retreat Program, Osaka, Japan, 20-21 December, 2018.

Minami Ando, Shigeyuki Magi, Kazunari Iwamoto, Mariko Okada

Biological significance of the oscillatory dynamics of NF-κB for target gene expression

3rd Symposium on Complex Biodynamics & Networks, Biopolis, Singapore, 10-12 December, 2018.

Minami Ando, Shigeyuki Magi, Mariko Okada

Significance of NF-κB dynamics on target gene expression in MCF-7 cells

QCBio 5th Annual Retreat, Los Angeles, CA, U.S.A, 25 September, 2019.

Minami Ando, Shigeyuki Magi, Mariko Okada

Significance of NF-κB dynamics on target gene expression in MCF-7 cells

2nd Annual Symposium on Multiscale Cell Fate, Irvine, CA, U.S.A, 28-29 October, 2019.